Title

Recognition of Tetraloop Hairpin RNA by the Double-Stranded RNA-Binding Domain of S. cerevisiae RNase III

Permalink

https://escholarship.org/uc/item/1dd7d1j7

Author

Hartman, Elon Avi

Publication Date

2012

Peer reviewed|Thesis/dissertation

UNIVERSITY OF CALIFORNIA

Los Angeles

Recognition of Tetraloop Hairpin RNA by the

Double-Stranded RNA–Binding Domain of *S. cerevisiae* RNase III

A dissertation submitted in partial satisfaction

of the requirements for the degree

Doctor of Philosophy in Molecular Biology

by

Elon Avi Hartman

2012

Abstract of the Dissertation

Recognition of Tetraloop Hairpin RNA by the

Double-Stranded RNA–Binding Domain of *S. cerevisiae* RNase III

by

Elon Avi Hartman

Doctor of Philosophy in Molecular Biology

University of California, Los Angeles, 2012

Professor Juli Feigon, Chair

The *S. cerevisiae* RNase III enzyme Rnt1p preferentially binds to dsRNA hairpin substrates with a conserved (A/u)GNN tetraloop fold, via shape-specific interactions by its dsRBD helix α1 to the tetraloop minor groove. The solution structure of Rnt1p dsRBD bound to an AAGU-capped hairpin reveals that the tetraloop undergoes a structural rearrangement upon binding to Rnt1p dsRBD to adopt a backbone conformation that is essentially the same as the AGAA tetraloop, and indicates that a conserved recognition mode is used for all Rnt1p substrates. Comparison of free and RNA-bound Rnt1p dsRBD reveals that tetraloop-specific binding requires a conformational change in helix α1. To investigate whether conformational flexibility in the dsRBD regulates the binding specificity, I determined the backbone dynamics of the Rnt1p dsRBD in the free and AGAA hairpin-bound states using NMR spin relaxation experiments. The intrinsic μs-ms timescale dynamics of the dsRBD suggests that helix α1 undergoes conformational sampling in the free state, with large dynamics at some residues in the α1-β1 loop (α1-β1 hinge). These results, in combination with an RDC-refined solution structure of the free dsRBD, revealed that the Rnt1p dsRBD has an extended hydrophobic core comprising helix α1, the α1-β1 loop, and helix α3. Analysis of the backbone dynamics and structures of the free and bound dsRBD reveals that

slow-timescale dynamics in the $\alpha 1$-$\beta 1$ hinge are associated with concerted structural changes in the extended hydrophobic core that govern binding of helix $\alpha 1$ to AGAA tetraloops. The dynamic behavior of the dsRBD bound to a longer AGAA hairpin reveals that dynamics within the hydrophobic core differentiate between specific and nonspecific sites. Mutations of residues in the $\alpha 1$-$\beta 1$ hinge result in changes to the dsRBD stability and RNA-binding affinity, and cause defects in snoRNA processing *in vivo*. These results reveal that dynamics in the extended hydrophobic core are important for binding site selection by the Rnt1p dsRBD.

The dissertation of Elon Avi Hartman is approved.

Arnold J. Berk

Douglas L. Black

Guillaume Chanfreau

Feng Guo

Juli Feigon, Committee Chair

University of California, Los Angeles

2012

TABLE OF CONTENTS

List of Figures

Chapter 3 Intrinsic dynamics of an extended hydrophobic core in the *S. cerevisiae* RNase III dsRBD contributes to recognition of specific RNA binding sites

ACKNOWLEDGEMENTS

<center>## Vita</center>

2004	B.S. Biology (Cell and Molecular)
	California State University, Northridge
2006, 2010	Teaching Assistant
	University of California, Los Angeles
2006-2012	Graduate Student Researcher
	University of California, Los Angeles

<center>## Publications</center>

Wang, Z., Hartman, E., Roy, K., Chanfeau, G., and Feigon, J. (2011). Structure of a yeast RNase III dsRBD complex with a noncanonical RNA substrate provides new insights into binding specificity of dsRBDs. *Structure.* **19**: 999-1010.

Hartman, E., Wang, Z., Zhang, Q., Roy, K., Chanfreau, G., and Feigon, J. (2012). Intrinsic dynamics of an extended hydrophobic core in the *S. cerevisiae* RNase III dsRBD contributes to recognition of specific RNA binding sites. *J. Mol. Biol.* In press. doi:10.1016/j.jmb.2012.11.025

CHAPTER 1

Introduction

S. cerevisiae RNase III (Rnt1p)   The RNase III family of enzymes processes a variety of double-stranded RNA (dsRNA) substrates, including precursors to cellular non-coding RNAs, as well as miRNA and siRNA.[1-3] RNase III enzymes cleave dsRNA targets using a conserved catalytic mechanism, leaving a two-nucleotide 3′ overhang on processed RNAs, a distinctive feature of RNase III cleavage. RNase III family members typically have one or two double-stranded RNA-binding domains (dsRBDs) and one or two endonuclease domains (endoNDs), which cleave dsRNA substrates as an inter- or intramolecular dimer.[4,5] RNase III enzymes are divided into four classes, according to domain structure: bacterial RNase III (class 1), yeast RNase III (Rnt1p, class 2), Drosha (class 3), and Dicer (class 4). Rnt1p includes three domains: an N-terminal domain that likely aids dimerization, a endoND, and a dsRBD (Fig. 1.1). Like bacterial RNase III enzymes, Rnt1p binds to and cleaves RNA as an intermolecular dimer.
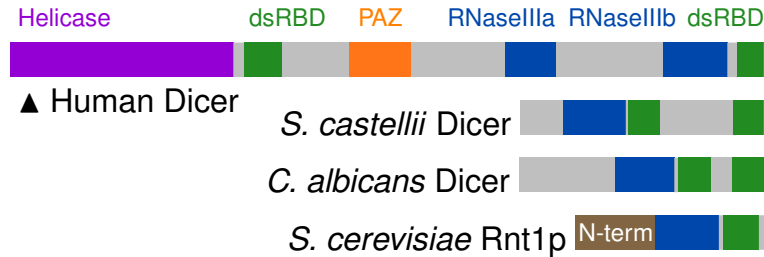
Fig. 1.1. Domain structure of RNase III enzymes.

Rnt1p, the primary RNase III enzyme in *S. cerevisiae*, processes pre-rRNA, pre-snoRNA, and pre-snRNA targets, cleaving the RNA stem of specific tetraloop-hairpin substrates 14-16 bp away from the tetraloop.[8] Box C/D snoRNAs in *S. cerevisiae* undergo 5′ end processing via cleavage at a specific site by Rnt1p, followed by further processing by the exonucleases Xrn1p or Ratp1. Rnt1p cleavage sites are defined by the presence of stem loops in target RNA (Fig. 1.2).

Although *S. cerevisiae* lacks an miRNA processing pathway, closely related budding yeast species, including *S. castellii* and *K. polysporus*, have a functional

RNAi pathway that employs a noncanonical yeast Dicer with a domain structure similar to Rnt1p, and RNAi has been reconstituted in *S. cerevisiae* using only a yeast Dicer and Argonaut.[6] Moreover, Dcr1 from *Candida albicans* is able to carry out the roles of both Dicer and Rnt1p, suggesting that the two dsRBDs for *C. albicans* Dcr1 function in multiple RNA-processing pathways.[7]
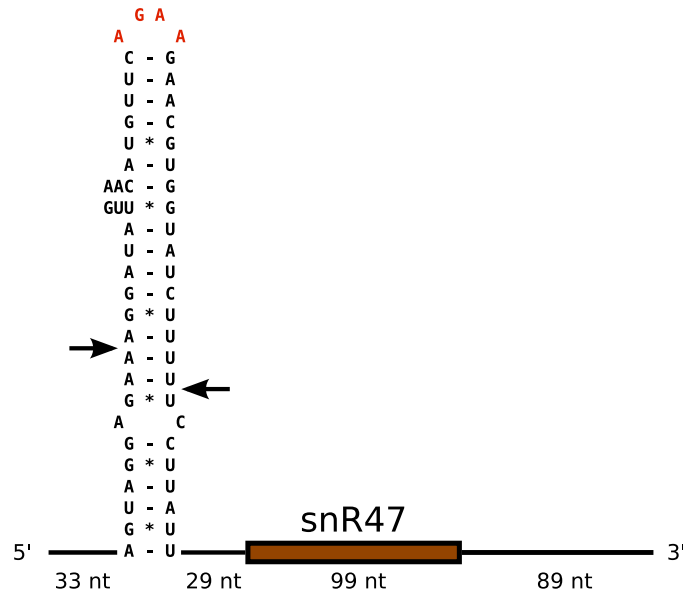
Fig. 1.2. The *S. cerevisiae* snR47 pre-snoRNA. The specific binding site for Rnt1p, an AGAA tetraloop hairpin, is highlighted in red. The Rnt1p cleavage site is indicated by arrows.

Rnt1p also offers an unusual example of RNA recognition in that it specifically binds to RNA substrates capped by an NGNN tetraloop through structure-specific recognition of the tetraloop.[9] Tetraloop recognition is mediated by the Rnt1p double-stranded RNA binding domain (dsRBD), which specifically recognizes the conserved shape of the tetraloop on target substrates, with no base-specific contacts. Like canonical dsRBDs, the Rnt1p dsRBD interacts with successive minor, major, and minor grooves but adopts a conformation in the bound state that differs from the conformation of the free Rnt1p dsRBD and other dsRBDs, both free and in complex with RNA. The Rnt1p dsRBD extends the canonical $\alpha\beta\beta\beta\alpha$ secondary structure motif with a third C-terminal helix that has been proposed to

contribute to recognition of Rnt1p substrates via steric effects on the orientation of helix $\alpha 1$.[9,10] Binding of the dsRBD to the tetraloop is required for substrate cleavage at the correct site, 14-16 bp from the tetraloop, although Rnt1p can nonspecifically cleave dsRNA under certain conditions.
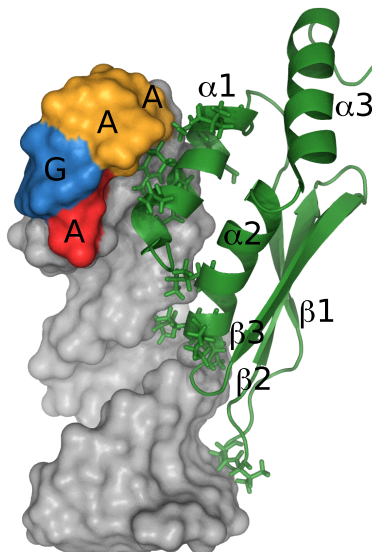
Fig. 1.3. Structure of the Rnt1p dsRBD bound to an AGAA tetraloop hairpin.

Although, Rnt1p usually binds to a conserved class of RNA tetraloops characterized by the consensus sequence NGNN, the *S. cerevisiea* snoRNA snR48 was found to serve as a specific Rnt1p substrate, despite having a non-canonical AAGU tetraloop in place of the canonical AGAA tetraloop.[11] This discovery prompted us to investigate whether the Rnt1p dsRBD binds to AAGU-tetraloop substrates differently than to NGNN-tetraloop substrates. The results of these studies are presented in Chapter 2.

The structure of the dsRBD in complex with a specific tetraloop-hairpin substrate revealed that the dsRBD interacts with target RNAs in successive tetraloop minor, major, and minor grooves, with no base-specific contacts to the RNA (Fig. 1.3).[9] However, the structural details of interaction between the Rnt1p dsRBD and a model specific RNA substrate do not fully explain the unique preference of

the Rnt1p dsRBD for NGNN-tetraloop substrates. In particular, dsRNA recognition by the Rnt1p dsRBD is likely to be dynamic, with interconversion between specific and nonspecific binding modes. Furthermore, previous studies of the interaction of RNA- and DNA-binding domains with specific and nonspecific substrates indicate that these proteins dynamically interact with their targets using a number of distinct modes, including sliding and hopping along the DNA or RNA stem, and intermolecular transfer between substrates. Discerning the molecular requirements for RNA recognition by the Rnt1p dsRBD, including both structure and dynamics, has broad applications in understanding protein-RNA binding and clarifies the function of RNase III enzymes, an important class of enzymes with relevance to RNA processing and gene regulation. Here, I examine how intrinsic dynamics of the dsRBD facilitates a conformational search for the specific binding mode, and allows Rnt1p to functionally distinguish between specific and nonspecific sites on RNA despite small differences in binding affinity. The results of these studies are presented in Chapter 3.

Double-stranded RNA–binding domains dsRBDs typically interact with a variety of dsRNA substrates via interactions by helix $\alpha 1$, the $\beta 1$-$\beta 2$ loop, and helix $\alpha 2$ with the RNA minor, major, and minor grooves, respectively. Although dsRBDs usually bind to dsRNA nonspecifically, as in the crystal structure of the Xlrbpa dsRBD in complex with A-form dsRNA,[12] a number of dsRBDs have been found to have additional modes of substrate specificity, including structure- and sequence-specific interactions. For example, the human ADAR dsRBD in complex with RNA and the prokaryotic *Aquifex aeolicus* RNase III dsRBD can sequence specifically recognize dsRNA substrates though hydrophobic contacts between dsRBD side chains and nucleotide bases.[13] Here, I have investigated the structural and dynamic basis for substrate recognition by the Rn1p dsRBD.

Methods for studying dynamics of proteins To analyze the dynamics of the free dsRBD and dsRBD/RNA complexes, I used ^{15}N NMR spin relaxation experiments in combination with model-free analysis to obtain quantitative information of the fast- and slow-timescale dynamics for the dsRBD backbone. Model-free analysis requires an initial estimate of the rotational correlation time and the diffusion tensor, obtained using the program HYDRONMR, which predicts the hydrodynamic properties of the protein and provides estimates for the rotational correlation time and diffusion tensor. HYDRONMR estimates for the diffusion tensor are optimized using the program ModelFree[14] prior to model selection. Relaxation parameters are interpreted using the Lipari-Szabo model-free formalism to obtain values for motional parameters describing the dynamic behavior of backbone amide bond vectors.[15,16] ModelFree optimizes the values for the correlation time and fits relaxation data for each residue to one of five increasingly complex models, where model 1 includes the parameter S_s^2; model 2, S_s^2 and τ_e; model 3, S_s^2 and R_{ex}; model 4, S_s^2, τ_e, and R_{ex}; and model 5, S_s^2, S_f^2, and τ_e. Following model selection for all residues, global and internal parameters are optimized with a grid-search algorithm using an axially symmetric diffusion tensor.

Summary of the thesis Chapter 2, "Structure of a yeast RNase III dsRBD complex with a noncanonical RNA substrate provides insights into binding specificity of dsRBDs," describes the structure of the dsRBD/AAGA complex. The structure of the dsRBD/AAGU complex, determined by NMR, revealed that the dsRBD uses the same binding mode for both canonical and non-canonical substrates. Intriguingly, and unlike NGNN-tetraloop substrates, the AAGU tetraloop undergoes a structural rearrangement upon binding of the dsRBD to achieve a fold nearly identical to the AAGU tetraloop. Cleavage and binding efficiency for the AAGU-tetraloop substrate, measured by assays of single-turnover cleavage kinetics and by NMR titration experiments, respectively, supported the finding that

6

the AAGU tetraloop is recognized in the same manner as the AGAA tetraloop. This work was a joint project with Dr. Zhonghua Wang, a postdoctoral fellow in the laboratory, and we are co-first authors on the publication. My contributions to this work include the Rnt1p cleavage assays, initial NMR titration experiments, data analysis, figure preparation, and manuscript writing. This work was also done in collaboration with the laboratory of Professor Guillaume Chanfreau and his graduate student Kevin Roy, who did the *in vivo* experiments and analyzed the data.

Chapter 3, "Intrinsic dynamics of an extended hydrophobic core in the *S. cerevisiae* RNase III dsRBD contributes to recognition of specific RNA binding sites," presents results for the dynamics of the free dsRBD and the dsRBD/AGAA complex. The Rnt1p dsRBD recognizes the AGAA tetraloop hairpin structure specifically and undergoes conformational changes to bind to the specific binding site. To investigate whether conformational flexibility in the dsRBD regulates the binding specificity, we determined the backbone dynamics of the Rnt1p dsRBD in the free and AGAA hairpin-bound states using NMR spin relaxation experiments. The slow-timescale dynamics of the free dsRBD revealed the presence of a dynamic hinge in the $\alpha 1$-$\beta 1$ loop ($\alpha 1$-$\beta 1$ hinge) that allows helix $\alpha 1$ to sample multiple orientations in the free state. Comparison of a newly determined, RDC-refined structure of the free dsRBD with the bound dsRBD revealed that the dsRBD has an extended hydrophobic core comprising helix $\alpha 1$, the $\alpha 1$-$\beta 1$ loop, and helix $\alpha 3$ that undergoes conformational changes between free and bound states. For this project, I made the RNA and protein samples, acquired and analyzed all of the relaxation data, and wrote the manuscript. Dr. Qi Zhang, a postdoctoral fellow in the laboratory, taught me how to collect and analyze the relaxation data and assisted with experimental design and data collection. Dr. Zhonghua Wang solved the structure of the free protein. Collaborators Professor Guilluame Chanfreau and Kevin Roy contributed the *in vivo* experiments.

1.1 References

1. Ketting, R. F., Fischer, S. E., Bernstein, E., Sijen, T., Hannon, G. J. and Plasterk, R. H. (2001). Dicer functions in RNA interference and in synthesis of small RNA involved in developmental timing in *C. elegans*. *Genes. Dev.* **15**, 2654-9.

2. Knight, S. W. and Bass, B. L. (2001). A role for the RNase III enzyme DCR-1 in RNA interference and germ line development in *Caenorhabditis elegans*. *Science*. **293**, 2269-71.

3. He, L. and Hannon, G. J. (2004). MicroRNAs: small RNAs with a big role in gene regulation. *Nat. Rev. Genet.* **5**, 522-31.

4. Ji, X. (2006). Structural basis for non-catalytic and catalytic activities of ribonuclease III. *Acta. Crystallogr. D. Biol. Crystallogr.* **62**, 933-40.

5. MacRae, I. J. and Doudna, J. A. (2007). Ribonuclease revisited: structural insights into ribonuclease III family enzymes. *Curr. Opin. Struct. Biol.* **17**, 138-45.

6. Weinberg, D. E., Nakanishi, K., Patel, D. J. and Bartel, D. P. (2011). The inside-out mechanism of Dicers from budding yeasts. *Cell*. **146**, 262-76.

7. Bernstein, D. A., Vyas, V. K., Weinberg, D. E., Drinnenberg, I. A., Bartel, D. P. and Fink, G. R. (2012). *Candida albicans* Dicer (CaDcr1) is required for efficient ribosomal and spliceosomal RNA maturation. *Proc. Natl. Acad. Sci. U.S.A.* **109**, 523-8.

8. Chanfreau, G., Buckle, M. and Jacquier, A. (2000). Recognition of a conserved class of RNA tetraloops by *Saccharomyces cerevisiae* RNase III. *Proc. Natl. Acad. Sci. U.S.A.* **97**, 3142-7.

9. Wu, H., Henras, A., Chanfreau, G. and Feigon, J. (2004). Structural basis for recognition of the AGNN tetraloop RNA fold by the double-stranded RNA-binding domain of Rnt1p RNase III. *Proc. Natl. Acad. Sci. U.S.A.* **101**, 8307-12.

10. Leulliot, N., Quevillon-Cheruel, S., Graille, M., van Tilbeurgh, H., Leeper, T. C., Godin, K. S., Edwards, T. E., Sigurdsson, S. T., Rozenkrants, N., Nagel, R. J., Ares, M. and Varani, G. (2004). A new alpha-helical extension promotes RNA binding by the dsRBD of Rnt1p RNAse III. *EMBO J.* **23**, 2468-77.

11. Ghazal, G. and Elela, S. A. (2006). Characterization of the reactivity determinants of a novel hairpin substrate of yeast RNase III. *J. Mol. Biol.* **363**, 332-44.

12. Ryter, J. M. and Schultz, S. C. (1998). Molecular basis of double-stranded RNA-protein interactions: structure of a dsRNA-binding domain complexed with dsRNA. *EMBO J.* **17**, 7505-13.

13. Stefl, R., Oberstrass, F. C., Hood, J. L., Jourdan, M., Zimmermann, M., Skrisovska, L., Maris, C., Peng, L., Hofr, C., Emeson, R. B. and Allain, F. H. (2010). The solution structure of the ADAR2 dsRBM-RNA complex reveals a sequence-specific readout of the minor groove. *Cell* **143**, 225-37.

14. Mandel, A. M., Akke, M. and Palmer, A. G., 3rd. (1995). Backbone dynamics of *Escherichia coli* ribonuclease HI: correlations with structure and function in an active enzyme. *J. Mol. Biol.* **246**, 144-63.

15. Lipari, G. and Szabo, A. (1982). Model-free approach to the interpretation of nuclear magnetic resonance relaxation in macromolecules. 2. Analysis of experimental results. *J. Am. Chem. Soc.* **104**, 455970.

16. Lipari, G. and Szabo, A. (1982). Model-free approach to the interpretation of nuclear magnetic resonance relaxation in macromolecules. 1. Theory and range of validity. *J. Am. Chem. Soc.* **104**, 454659.

CHAPTER 2

Structure of a yeast RNase III dsRBD complex with a noncanonical RNA substrate provides new insights into binding specificity of dsRBDs

Article

Structure of a Yeast RNase III dsRBD Complex with a Noncanonical RNA Substrate Provides New Insights into Binding Specificity of dsRBDs

Zhonghua Wang,[1,2,3] Elon Hartman,[1,2,3] Kevin Roy,[1,2] Guillaume Chanfreau,[1,2] and Juli Feigon[1,2,*]
[1]Department of Chemistry and Biochemistry
[2]Molecular Biology Institute
P.O. Box 951569, University of California, Los Angeles, CA 90095-1569, USA
[3]These authors contributed equally to this work
*Correspondence: feigon@mbi.ucla.edu
DOI 10.1016/j.str.2011.03.022

SUMMARY

dsRBDs often bind dsRNAs with some specificity, yet the basis for this is poorly understood. Rnt1p, the major RNase III in *Saccharomyces cerevisiae*, cleaves RNA substrates containing hairpins capped by A/uGNN tetraloops, using its dsRBD to recognize a conserved tetraloop fold. However, the identification of a Rnt1p substrate with an AAGU tetraloop raised the question of whether Rnt1p binds to this noncanonical substrate differently than to A/uGNN tetraloops. The solution structure of Rnt1p dsRBD bound to an AAGU-capped hairpin reveals that the tetraloop undergoes a structural rearrangement upon binding to Rnt1p dsRBD to adopt a backbone conformation that is essentially the same as the AGAA tetraloop, and indicates that a conserved recognition mode is used for all Rnt1p substrates. Comparison of free and RNA-bound Rnt1p dsRBD reveals that tetraloop-specific binding requires a conformational change in helix α1. Our findings provide a unified model of binding site selection by this dsRBD.

INTRODUCTION

Eukaryotic members of the RNase III family of endoribonucleases cleave double-stranded RNA (dsRNA) targets involved in a variety of gene expression pathways (Conrad and Rauhut, 2002; Lamontagne et al., 2001), including the maturation of precursor ribosomal RNA (rRNA) (Elela et al., 1996; Henras et al., 2004; Kufel et al., 1999), small nuclear RNA (snRNA) and small nucleolar RNA (snoRNA) processing (Conrad and Rauhut, 2002; Lamontagne et al., 2001), and RNA interference (RNAi) and microRNA (miRNA) processing (Ketting et al., 2001; Knight and Bass, 2001; Lee et al., 2003b). Rnt1p, the major RNase III present in *Saccharomyces cerevisiae*, plays an essential role in the processing of rRNA, snRNAs, and snoRNAs (Chanfreau et al., 1998a, 1998b; Elela et al., 1996; Kufel et al., 1999) in budding yeast. Rnt1p is also important for mRNA quality control, cleaving

intronic sequences of unspliced pre-mRNAs (Danin-Kreiselman et al., 2003). A Rnt1p target site in the mRNA coding for the essential telomerase protein Est1p has been proposed to be important for maintenance of telomere length through regulation of Est1p expression (Larose et al., 2007). Several studies have indicated that Rnt1p may play a role in transcription termination by cleavage of nascent transcripts (Catala et al., 2008; El Hage et al., 2008; Ghazal et al., 2009; Prescott et al., 2004). Drosha and Dicer, other members of the RNase III family, are involved in miRNA processing and RNAi (Ketting et al., 2001; Lee et al., 2003b). Although the RNAi pathway has been evolutionarily lost in *S. cerevisiae*, it has been found in closely related yeast species such as *S. castellii* and *Kluyveromyces polysporus*. Introduction of *S. castellii* Dicer and Argonaute into *S. cerevisiae* resulted in a functional RNAi pathway (Drinnenberg et al., 2009). Furthermore, budding yeast Dicers are more closely related to Rnt1p than to canonical Dicer, highlighting the importance of this representative of the RNase III family of enzymes.

All RNase III enzymes contain one or two conserved endonuclease domains (endoNDs). Two endoNDs form an intra- or intermolecular dimer to create a large catalytic valley for Mg^{2+}-dependent catalysis (Gan et al., 2005, 2008; Ji, 2006, 2008; MacRae and Doudna, 2007; Nicholson, 1999; Sun et al., 2005). Most RNase III enzymes also have one or more double-stranded RNA binding domains (dsRBDs). The N-terminal region of RNase III enzymes is variable across the family, and may include one or more additional domains with different functions. Rnt1p, like the bacterial RNase III enzymes, contains one endonuclease domain and one dsRBD. However, Rnt1p also has an N-terminal domain unique to yeast RNase IIIs whose function is uncertain but which may be required for the stabilization of Rnt1p homodimers (Lamontagne et al., 2000). RNase IIIs found in budding yeasts have a domain structure similar to that of Rnt1p, whereas most Drosha and Dicer enzymes have one or two dsRBDs, two endoNDs, and an N-terminal accessory domain (MacRae and Doudna, 2007; Nowotny and Yang, 2009).

The dsRBD is the second most abundant RNA binding domain. This domain specifically recognizes dsRNA (Bycroft et al., 1995; Doyle and Jantsch, 2002; Hall, 2002; Kharrat et al., 1995) and has a conserved αββα fold (Bycroft et al., 1995; Kharrat et al., 1995; Nanduri et al., 1998; Ramos et al., 2000; Ryter and Schultz, 1998; Wu et al., 2004). The first crystal structure of a dsRBD/dsRNA complex revealed that helix α1, the

β3-α2 loop, and the β1-β2 loop interact with the sugar-phosphate backbone of successive minor, major, and minor grooves, respectively, along one face of an RNA helix, without any apparent base pair specificity (Ryter and Schultz, 1998). The recognition of dsRNA by dsRBDs plays an important role in the catalytic cleavage or modification of dsRNAs by many RNases (Gan et al., 2008; Ghazal et al., 2009; Ji, 2006, 2008; MacRae and Doudna, 2007; Sun et al., 2005; Wu et al., 2004) and RNA modification enzymes such as ADAR (Stefl et al., 2010; Yamashita et al., 2011). Based on the structures of bacterial RNase III/dsRNA complexes (Gan et al., 2006), dsRBDs are thought to contribute primarily to specificity of binding to dsRNA but not to target site selection (Nicholson, 1999; Shi et al., 2011), although there are two base contacts that have recently been proposed to be sequence specific (Stefl et al., 2010). In contrast, Rnt1p dsRNA substrates are capped by A/uGNN tetraloops located 14–16 bp away from the cleavage site (Chanfreau et al., 2000; Nagel and Ares, 2000), and specificity for these substrates resides in the dsRBD (Chanfreau et al., 2000; Lamontagne and Elela, 2004; Lamontagne et al., 2003; Nagel and Ares, 2000; Wu et al., 2004). Structural studies have revealed that A/uGNN tetraloops adopt a conserved fold (Lebars et al., 2001; Wu et al., 2001, 2004), the shape of which is recognized on the minor groove side by Rnt1p dsRBD (Wu et al., 2004). Surprisingly, the dsRBD has no direct contacts to the conserved A and G bases, which point into the major groove, but rather its helix α1 fits snugly into the minor groove side of the tetraloop and the top of the stem, interacting with the sugar-phosphate backbone and nonconserved 3′ bases. To date, this is the only known example of dsRBD binding specificity through terminal loop recognition. Rnt1p dsRBD is also unusual in containing an additional helix α3, which has been proposed to contribute to recognition of the tetraloop indirectly by stabilizing helix α1 (Leulliot et al., 2004; Wu et al., 2004).

A genome-wide search in *S. cerevisiae* for snoRNA substrates of Rnt1p identified the noncanonical snoRNA substrate snR48 (Ghazal et al., 2005). Unlike most Rnt1p substrates, snR48 contains a Rnt1p recognition site consisting of an AAGU-capped hairpin. It was proposed that the AAGU tetraloop adopts a different fold from the canonical fold of AGNN tetraloops (Gaudin et al., 2006; Ghazal and Elela, 2006), and that Rnt1p distinguishes between these two different "classes" of tetraloop-hairpin substrates using different networks of protein-RNA interactions. To investigate the molecular basis for the recognition of the AAGU hairpin and to gain further understanding of substrate-specific recognition by Rnt1p, we determined the NMR solution structure of Rnt1p dsRBD in complex with a dsRNA hairpin capped by an AAGU tetraloop and investigated in vitro and in vivo cleavage and dsRBD binding. We find that when in complex with the dsRBD, the AAGU tetraloop undergoes a structural rearrangement to adopt a backbone fold and interactions that are essentially the same as those in the complex of the dsRBD with an AGAA hairpin. Comparison of the structures of the complexes to previously determined solution and crystal structures of the free dsRBD showed that the dsRBD helix α1 undergoes a conformational change upon binding to both AAGU and AGAA tetraloops. Taken together, our results provide new insights into substrate-specific recognition by dsRBDs and provide a structural framework for

a conserved general mode of RNA substrate recognition by Rnt1p.

RESULTS

The AAGU Hairpin Binds to and Is Efficiently Cleaved by Rnt1p in the Context of the snR47 Stem Sequence

We investigated, using NMR spectroscopy, the interaction of Rnt1p dsRBD with a 32 nt RNA hairpin containing a 14 bp stem and capped by the AAGU tetraloop (AAGU hairpin) found in the snoRNA snR48 precursor. To facilitate comparisons between this complex (dsRBD/AAGU) and one with a canonical A/uGNN tetraloop, we used the same stem sequence as in the previously determined structure of a Rnt1p dsRBD/snR47h complex (dsRBD/AGAA), where the hairpin sequence was derived from the snoRNA snR47 precursor (Wu et al., 2004). The 2 bp below the tetraloop are the same for snR47 and snR48, but otherwise the stem sequences differ, except for the first and fourth base pairs in our hairpins. Complex formation was initially monitored by chemical shift changes observed in the ^{1}H-^{15}N HSQC spectra of the dsRBD upon the addition of AAGU (see Figure S1 available online). The dsRBD is at or near fast exchange with the hairpin on the NMR timescale, but the complex is saturated at a small excess of RNA, as observed for the dsRBD/AGAA complex, and amide chemical shift changes are very similar (Wu et al., 2004).

To compare the relative binding affinity of Rnt1p dsRBD to AGAA and AAGU hairpins, a series of ^{1}H-^{15}N HSQC spectra of the dsRBD were acquired at various ratios of added AGAA, AAGU, and UUCG hairpins under high-salt conditions. Previous studies have shown that the dsRBD does not specifically recognize a UUCG-capped hairpin (Chanfreau et al., 2000), so this hairpin was used as a comparison for nonspecific binding of the dsRBD to double-stranded RNA. Apparent K_D values calculated from global fitting of the HSQC titration data, assuming a one-site binding model, are 34.1 ± 2.9, 30.1 ± 3.8, and 280 ± 24.6 μM for the AAGU, AGAA, and UUCG hairpins, respectively (Figures 1A–1C). These values indicate that under the NMR conditions, Rnt1p dsRBD binds with the same affinity to both the AAGU and AGAA hairpins. In contrast, nonspecific binding to dsRNA capped by a UUCG tetraloop is about an order of magnitude weaker. This result is consistent with binding assays using full-length Rnt1p, which show it binds with a 5- to 10-fold weaker affinity to non-AGNN-containing tetraloops than to canonical tetraloop-containing substrates (Chanfreau et al., 2000; Nagel and Ares, 2000).

Previously, Rnt1p was reported to require a defined sequence in the stem region of snR48-derived AAGU hairpin substrates for optimal cleavage (Gaudin et al., 2006; Ghazal et al., 2005). To confirm that the snR47-AAGU hybrid hairpin is a good substrate for Rnt1p, we performed Rnt1p cleavage assays with substrates derived from snR47, capped by AGAA, AAGU, or UUCG tetraloops (snR47-AGAA, snR47-AAGU, and snR47-UUCG, respectively) (Figure 2A), under single-turnover conditions (Figure 2B). Both snR47-AAGU and snR47-AGAA showed specific cleavage, whereas snR47-UUCG was almost unreactive over the assayed reaction time. The fact that the snR47-UUCG substrate shows only a 10-fold reduction of binding (Figure 1C) but is almost completely refractory to Rnt1p cleavage confirms that, as shown

13
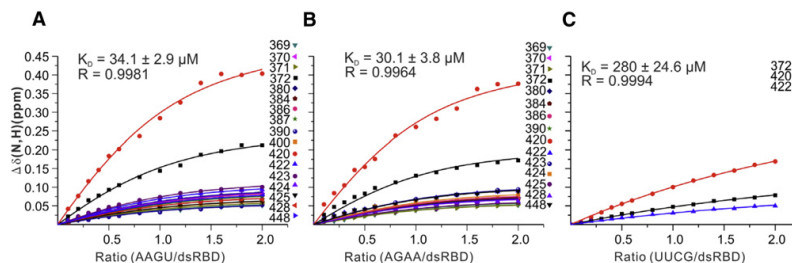
Figure 1. snR47-Derived dsRNA Capped by an AAGU Tetraloop Binds to the Rnt1p dsRBD

HSQC titration curves showing ^{15}N and ^{1}H chemical shift change $\Delta\delta(N,H) = [(\Delta\delta(H_N))^2 + (\Delta\delta(N_H)/4)^2]^{1/2}$ as a function of the concentration ratio for the titration of dsRBD with the (A) AAGU, (B) AGAA, and (C) UUCG hairpins. The continuous lines show the curves for all amides, with chemical shift changes >0.05 ppm fitted globally to a one-site binding model.

previously (Chanfreau et al., 2000; Nagel and Ares, 2000), the differences in binding affinity between different tetraloop-containing stems are not sufficient to explain the strong cleavage discrimination between these substrates. snR47-AAGU also shows more additional cleavage products than snR47-AGAA: one corresponds to an intermediate cleaved in one strand only (band below substrate band in Figure 2B), and the others correspond to some alternate cleavage sites. In vivo, cleavage at any of these alternative sites would still be expected to result in correct subsequent processing, because each of these cleaved intermediates is expected to be used at similar efficiencies by the Rat1p exonuclease (Lee et al., 2003a). Overall, cleavage of the

snR47-AAGU substrate occurred at a slightly slower rate than for snR47-AGAA, but the relative cleavage rates for this noncanonical substrate is comparable to the previously reported relative rates for canonical Rnt1p substrates containing AGAA and UGAA tetraloops (Wu et al., 2001). These results indicate that the AAGU tetraloop in the context of the snR47 stem sequence is sufficient to support cleavage at a rate comparable to A/uGNN tetraloop hairpin substrates.

To further investigate the ability of Rnt1p to recognize and process a substrate carrying an AAGU tetraloop, we analyzed the processing of snR47 mutant derivatives with different types of tetraloops in vivo. We introduced AAGU in place of AGAA in
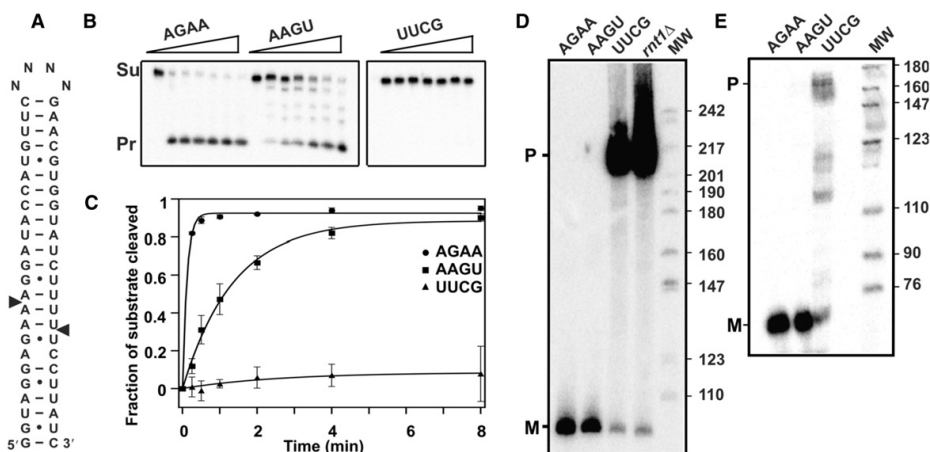
Figure 2. dsRNA Capped by an AAGU Tetraloop Is an Efficient Substrate for Rnt1p

(A) Sequence of snR47-derived RNA substrates, where NNNN is AGAA, AAGU, or UUCG, with the Rnt1p cleavage site indicated by arrowheads.

(B and C) Single-turnover cleavage kinetics for snR47-AGAA, snR47-AAGU, and snR47-UUCG.

(B) Phosphorimages of polyacrylamide gels of RNA from the cleavage reactions. Bands corresponding to the full-length substrate (Su) and the cleavage product (Pr) are indicated.

(C) Plot of fraction of substrate cleaved versus time. Error bars are the standard deviation for three experiments.

(D) Northern blot analysis of snR47 snoRNA expression carrying normal and mutant tetraloop sequences. Strains expressing snR47 with the wild-type (AGAA), AAGU, or UUCG loop sequences and a strain inactivated for Rnt1p (*rnt1Δ*) were analyzed. MW, molecular weight marker (MspI-digested pBR322); P, unprocessed precursor; M, mature snR47 snoRNA.

(E) Primer extension analysis of snR47 snoRNA expression carrying normal and mutant tetraloop sequences. Legends are as in (D).

14
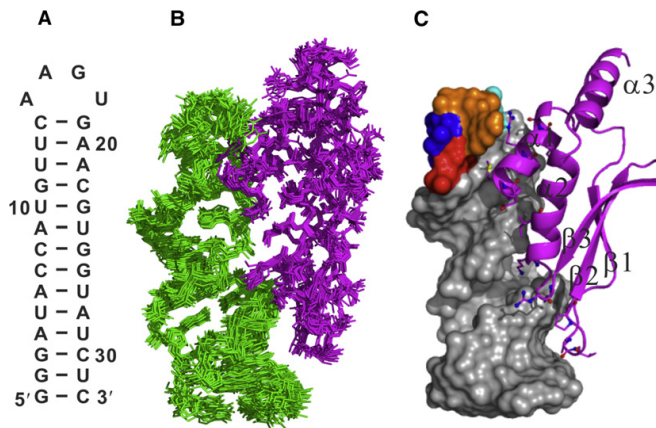
Figure 3. Solution Structure of the Rnt1p dsRBD/AAGU Complex
(A) Sequence and secondary structure of the AAGU hairpin used in the NMR studies.
(B) Superposition of the 16 lowest-energy structures, showing all heavy atoms. The dsRBD is in magenta and the AAGU hairpin is in green.
(C) Lowest-energy structure of the complex. The RNA is shown as a solvent-accessible surface and the protein as ribbons, with the amino acids at the protein-RNA interface shown as ball and sticks, with oxygen in red and nitrogen in blue. The nucleotides in the AAGU tetraloop are colored 5′ to 3′ red (A), blue (A), orange (G), and cyan (U).

the stem-loop sequence upstream from the *snR47* (Chanfreau et al., 1998a) chromosomal locus by homologous recombination (see Experimental Procedures). As controls for inefficient processing and complete loss of Rnt1p function, we generated a strain carrying a UUCG tetraloop and used a strain inactivated for Rnt1p (*rnt1Δ*), respectively. As shown by northern blot in Figure 2D, the AAGU mutant snoRNA precursor was processed as efficiently as the wild-type precursor in vivo, showing high levels of mature snoRNA and no apparent unprocessed precursor accumulation. In contrast, samples extracted from the UUCG tetraloop mutant or from the *rnt1Δ* strain exhibited little or no mature snoRNA and a strong accumulation of unprocessed precursors (Figure 2D). Primer extension analysis of the wild-type (AGAA) and AAGU or UUCG mutant strains confirmed the efficient 5′ end processing of the AAGU mutant and the strong processing defect of the UUCG mutant (Figure 2E). These results indicate that a hairpin capped by an AAGU tetraloop sequence can serve as an efficient recognition site for Rnt1p in vivo, even when placed on a substrate stem that normally contains a canonical AGNN tetraloop. In conclusion, AAGU tetraloop hairpins can be efficiently recognized by Rnt1p in vitro and in vivo, regardless of the stem sequence that they cap.

Overview of the Solution Structure of the Rnt1p dsRBD/AAGU Hairpin Complex

Protein and RNA resonances in the Rnt1p dsRBD/AAGU complex were assigned following previously established protocols (Wu et al., 2005). The protein-RNA interface was well defined by 43 intermolecular NOEs assigned from 2D filtered/edited NOESY (Peterson et al., 2004) (Figure S1). The structure of the dsRBD/AAGU complex has backbone root-mean-square deviations (rmsds) to the mean of 0.55 ± 0.11 Å and 0.64 ± 0.15 Å for the dsRBD and AAGU hairpin, respectively (Figure 3A and Table 1). The dsRBD adopts the standard α1β1β2β3α2 fold (Doyle and Jantsch, 2002), with the additional helix α3 packed against and stabilizing the C-terminal end of helix α1, as previously observed (Leulliot et al., 2004; Wu et al., 2004). The dsRBD binds to one face of the RNA and interacts primarily

with the sugar-phosphate backbone in three successive regions: the tetraloop minor groove and top 2 bp with helix α1, the stem major groove with the N-terminal end of helix α2 and the β3-α2 loop, and the stem minor groove with the β1-β2 loop (Figure 3B). All of the bases in the tetraloop are in the *anti* conformation, and the RNA stem forms an A-form helix.

Analysis of RDCs Indicates that the dsRBD Adopts the Same Conformation in Both the AAGU and AGAA Complexes

We compared the structures of dsRBDs in the dsRBD/AAGU and dsRBD/AGAA complexes using residual dipolar couplings (RDCs) (Cornilescu et al., 1998; Lipsitz and Tjandra, 2004). Structure calculations for the dsRBD/AAGU complex included 83 ^{1}H-^{15}N RDCs in the final refinement step. For comparison purposes, we measured and analyzed a comparable set of 81 RDCs for the dsRBD/AGAA complex, which had been previously determined and refined with 43 RDCs (Wu et al., 2004), and recalculated the structure. We first evaluated the quality of the structures by back-calculating the RDCs from the RDC-refined dsRBD/AAGU and dsRBD/AGAA structures using the program PALES (Zweckstetter and Bax, 2000) (Figures 4A and 4B). The quality factors (Q) are 11.5% and 9.4% for dsRBD/AAGU and dsRBD/AGAA, respectively, indicating an excellent agreement between the structures and their RDC data (Cornilescu et al., 1998). We next evaluated how similar the structures of the dsRBDs in the two complexes were to each other by back-calculating the set of RDCs for each complex using the structures of the other complex. Results for the lowest-energy structure in each structure ensemble are shown in Figures 4C and 4D. R factors for the back-calculated dsRBD/AGAA and dsRBD/AAGU complexes are 0.98, and Q factors are <20% for both cases. Similar results are observed for each set of individual structures in the structure ensembles (Figure S2). These values indicate that the dsRBD conformations in the two complexes are highly similar. The dsRBDs in the two complexes have an rmsd between the two ensembles of 1.18 ± 0.32 Å for all heavy atoms (Figure 4E), which is within experimental error of the pairwise rmsds of each ensemble.

The AAGU Tetraloop in the Complex Adopts a Backbone Fold Similar to that of the AGAA Tetraloop

The solution structure of the free AAGU tetraloop is substantially different from the A/uGNN fold (Gaudin et al., 2006) (Figure 5C;

15

Table 1. Structural Statistics of the Rnt1p dsRBD/AAGU Hairpin Complex

Distance and Dihedral Restraints	Protein	RNA
Total NOE restraints	2095	695
Intraresidue	842	243
Sequential	498	325
Medium (i+2 to i+4)	405	10
Long-range (>i+4)	350	117
Intermolecular NOE restraints	45	
Hydrogen-bond restraints	80	72
RDC restraints	83	
Dihedral-angle restraints	120	225
Structure Statistics (16 Lowest-Energy Structures)		
Number of NOE violations >0.2 Å	0	
Number of NOE violations >0.5 Å	0	
Number of dihedral violations >5°	0	
Number of RDC violations >2 (Hz)	0	
Rmsd of RDC (Hz)	0.878 ± 0.045	
Rmsd from ideal covalent geometry		
Bond lengths (Å)	0.0034 ± 0.0001	
Bond angles (°)	0.7725 ± 0.0057	
Impropers (°)	0.4700 ± 0.0178	
Rmsd from the mean structure	Backbone	Heavy Atoms
Protein (366–448) (Å)	0.54 ± 0.10	0.90 ± 0.14
RNA (3–14, 19–30) (Å)	0.59 ± 0.11	0.55 ± 0.09
Complex (3–14, 19–30, 366–448) (Å)	0.70 ± 0.11	0.85 ± 0.11
Ramachandran statistics		
Most favored regions (%)	78.0	
Additional allowed regions (%)	18.6	
Generously allowed regions (%)	2.1	
Disallowed regions (%)	1.3	

see below). Surprisingly, however, in the dsRBD/AAGU complex, the backbone fold and shape of the minor groove of the tetraloop are highly similar to that of the AGAA tetraloop (Figures 5A and 5B), with an rmsd for all backbone heavy atoms of 1.06 Å for the lowest-energy structures (Figure 5B). As is the case for the AGNN tetraloops (Wu et al., 2004), the first two bases in the AAGU tetraloop, A15 and A16, stack on each other and point into the major groove away from the Rnt1p dsRBD helix α1 in the minor groove. The last two bases, G17 and U18 on the 3′ side, point into the minor groove, and their backbones interact with helix α1 of the dsRBD (Figure 6). Although all point into the minor groove, the positions of these bases, which are not conserved in AGNN tetraloops, differ somewhat among tetraloops.

Although the backbone fold is the same for the AGAA and AAGU tetraloops in complex with the dsRBD, the second base (A16) is in the *anti* conformation and its position is quite different from that of the *syn* G in the AGAA tetraloop. The *syn* conformation positions the G amino group within hydrogen-bonding distance of one of the nonbridging oxygen atoms on its 5′ phosphate group, and therefore presumably stabilizes its stacking on the A (or U). An A in the second position does not have a proton donor at the same position as the G, and therefore cannot

hydrogen bond to the backbone even in the *syn* conformation. Thus, in the complex, the stabilization conferred by a hydrogen bond to the backbone from a *syn* G at position 2 of the tetraloop does not appear to be required for the AAGU tetraloop to adopt the same backbone conformation as an AGAA tetraloop.

In the free AAGU tetraloop, the first two As (A15 and A16) stack on each other and point into the major groove and the backbone turns after the second A, as is the case for the bound AAGU tetraloop; however, the position of the backbone before the turn is substantially different (Figure 5C). On the 3′ side of the loop, the Watson-Crick face of G17 points into the minor groove and the base is nearly coplanar with A16, while U18 points up above G17 and out into the major groove (Gaudin et al., 2006). In contrast, in the dsRBD/AAGU complex, the base of U18 is in the minor groove, and the positions of both G17 and U18 are significantly different, with the base of G17 pointing into the minor groove from near the top of the tetraloop and U18 below G17. Thus, the AAGU tetraloop in the hairpin undergoes a large conformational change upon binding to the dsRBD, to a conformation that presents a minor groove surface and backbone contacts to helix α1 that are highly similar to those in the AGAA tetraloop.

Because the dsRBD has the same binding affinity for the two hairpins but the AAGU tetraloop undergoes a larger conformational change, we measured the binding by isothermal titration calorimetry (Figure S3). Although the two complexes have the same ΔG, the dsRBD/AAGU complex has larger negative values for both ΔH and ΔS. For the dsRBD/AAGU and dsRBD/AGAA complexes, $\Delta H = -1.42 \times 10^4$ versus -0.91×10^4 kcal/mol and $\Delta S = -21.8$ and -3.94 kcal/molK, respectively. These results indicate that although the AAGU/dsRBD complex undergoes a larger change in enthalpy upon complex formation, this is offset by a compensatory decrease in entropy.

Comparison of the Protein-RNA Interfaces in the Rnt1p dsRBD/AAGU and dsRBD/AGAA Complexes

In both the dsRBD/AAGU and dsRBD/AGAA complexes, the β1-β2 loop contacts the stem minor groove of base pairs 2–5, the N-terminal end of helix α2 inserts into the major groove between base pairs 5 and 10, and helix α1 specifically recognizes the minor groove of the tetraloop and top 2 bp (Figures 3 and 6; Table S1). Almost all of the contacts are to the phosphodiester backbone. Detailed comparison of the dsRBD/AAGU and dsRBD/AGAA complexes shows that the interactions between the protein and RNA stem are nearly identical (Figure 6; Figure S4). In the minor groove of the 3 bp adjacent to the tetraloop, the D367 side-chain carboxyl group interacts with A20 2′ OH and A21 2′ OH through potential direct or water-mediated hydrogen bonds, and the side chain of K371 forms potential hydrogen bonds to A20 2′ OH and A21 O4′ for both complexes. On the 3′ side of the tetraloops, the guanidinium group of the R372 stacks onto the ring of the base G17 (in the AAGU tetraloop) or A17 (in the AGAA tetraloop) in the complexes (Figure 6; Figure S4). On the 5′ side of the tetraloop, the nonpolar side chain of M368 stacks onto the A15 ribose, and its sulfur group forms a potential water-mediated hydrogen bond with C14 O2. In the dsRBD/AGAA complex, the R372 guanidinium group and S376 OH form hydrogen bonds with the 2′ OH of A17 and A18, respectively (Figure S4), whereas in the AAGU complex the R372
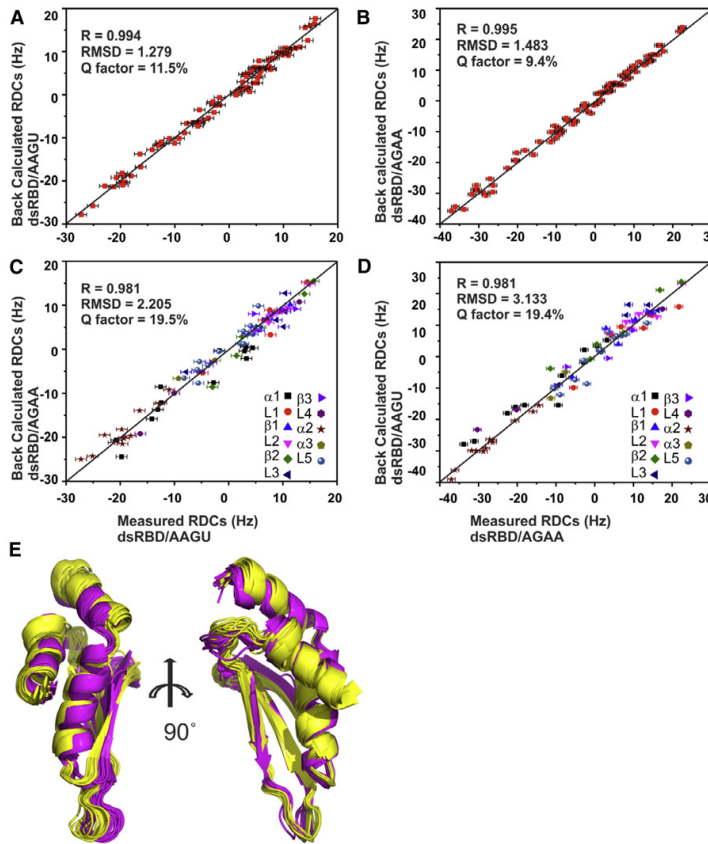
16

Figure 4. Correlation Plots between Experimental and Back-Calculated RDCs for the dsRBD/AAGU and dsRBD/AGAA Hairpin Complexes

(A) dsRBD/AAGU hairpin versus itself.

(B) dsRBD/AGAA hairpin versus itself.

(C) dsRBD/AAGU hairpin versus dsRBD/AGAA hairpin.

(D) dsRBD/AGAA hairpin versus dsRBD AAGU hairpin.

(A–D) R factors, rmsds, and Q values are shown with the plots. Residues in (C) and (D) are shown as follows: $\alpha1$ (367–378), L1 (379–385), $\beta1$ (386–390), L2 (391–399), $\beta2$ (400–405), L3 (406–411), $\beta3$ (412–417), L4 (418–420), $\alpha2$ (421–432), L5 (433–434), and $\alpha3$ (435–448). Error bars are ±1 Hz, which is the standard deviation of the RDC measurement.

(E) Superpositions of the ensembles of the 16 lowest-energy structures of the dsRBD in the dsRBD/AAGU hairpin (magenta) and dsRBD/AGAA hairpin (gold) complexes. The structures were aligned using the secondary-structure elements $\alpha1$, $\beta1$, $\beta2$, $\beta3$, $\alpha2$, and $\alpha3$.

guanidinium group forms a hydrogen bond with the 2′ OH of A15 and G17, and S376 OH forms a hydrogen bond with the 2′ OH of U18 (Figure 6B). These small differences can be attributed to the difference in sequence at these positions. Neither the tetraloop sequence nor the top 2 bp are conserved and, consistent with this, no specific contacts to the bases were observed. Mutation of M368, which has a potential interaction with C14 O2, to alanine, does not affect binding (Henras et al., 2005). Thus, the dsRBD recognizes the A/uGNN and AAGU tetraloops in the same way, by shape-specific binding.

Conformational Changes in the dsRBD upon Binding to Target RNA

Because the structure of the free Rnt1p dsRBD has been reported (Leulliot et al., 2004), we were able to examine any conformational changes that take place in the dsRBD upon binding to the AAGU hairpin as well as the AGAA hairpin in detail. We acquired a set of RDC data for the free dsRBD in solution. Of the NMR solution and two crystal structures (from one asymmetric unit) reported, the experimental RDCs fit best to the crystal structure of chain A (Protein Data Bank [PDB] ID code 1T4O) (Figure S5), so this structure was used for comparison

to our bound complexes. To quantitatively compare the structures of the free and AAGU tetraloop-bound dsRBDs, the experimental RDCs from the secondary-structure elements $\beta1$, $\beta2$, $\beta3$, $\alpha1$, and $\alpha2$ for the dsRBD/AAGU complex were plotted versus the RDCs calculated from the crystal structure (Figure 7A). Helix $\alpha3$ was excluded from this analysis, because it adopts three different orientations in the solution and two crystal structures (Leulliot et al., 2004). The correlation gives a Q factor of 32%, but when the RDCs from helix $\alpha1$ are deleted from the analysis, the Q factor decreases to 16%. Similar results were obtained for dsRBD bound to the AGAA hairpin (Figure 7B). When experimental RDCs from helix $\alpha1$ only are compared (free dsRBD versus dsRBD/AAGU complex and dsRBD/AAGU complex versus dsRBD crystal chain A), poor correlations are obtained (Q = 32% and 49%, respectively) (Figure S5). Taken together, these data indicate that there is a significant change in helix $\alpha1$ when the dsRBD binds to target RNA, consistent with structural differences observed by direct comparison of the structures as described below.

Comparison of the structures of the free and AAGU hairpin-bound dsRBD revealed that all of the regions of the dsRBD that interact with the RNA show significant changes in position between the free and bound dsRBD (Figure 7C). The $\beta1$-$\beta2$ loop, which inserts into the stem minor groove in the complex, points away ∼6 Å in the free dsRBD. The N-terminal end of helix $\alpha2$ and the $\beta3$-$\alpha2$ loop also shift to insert into the major groove. Helix $\alpha1$ rotates about 18° (Figure 7E) and bends slightly from L374 to S376 (Figure 7D) to fit into the convex surface of the tetraloop. In the free dsRBD, helix $\alpha1$ begins at N369, whereas in the complex it begins at L366. Side chains of M368, R372,
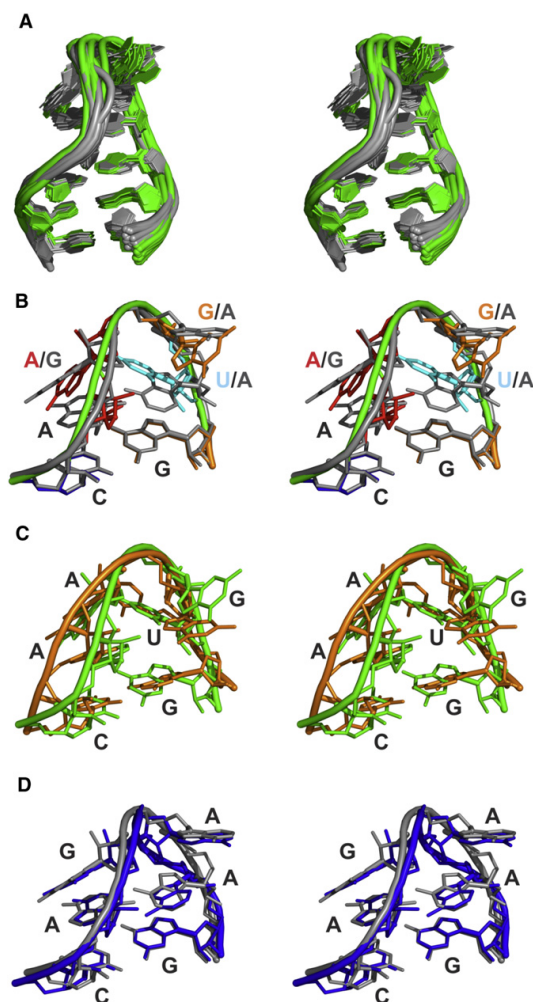
17

Figure 5. Comparison of the Structures of the AAGU and AGAA Tetraloops in the Free and dsRBD-Bound States

Stereo views are shown.

(A) Superposition of the ensemble structures (16 lowest-energy) of the dsRBD-bound AAGU (green) and dsRBD-bound AGAA (gray) tetraloops and the four stem base pairs below the tetraloops. The structures were aligned using residues 11–22.

(B) Superpositions of the lowest-energy structures of the dsRBD-bound AAGU tetraloop and dsRBD-bound AGAA tetraloop (rmsd 0.975 Å). Nucleotides for dsRBD-bound AAGU are shown in red (A), orange (G), dark blue (C), and cyan (U).

(C) Free AAGU tetraloop (gold) and dsRBD-bound AAGU (green) tetraloop (rmsd 1.64 Å).

(D) Free AGAA tetraloop (blue) and dsRBD-bound AGAA (gray) tetraloop (rmsd 0.99 Å).

Superpositions for (B)–(D) include the tetraloops and closing base pair. Rmsds are for backbone heavy atoms.

and S376 all shift position to align along one face of the helix to form van der Waals interactions and hydrogen bonds to the 2′ OH in the tetraloop minor groove (Figures 6A and 7D). Thus, helix α1 undergoes a change in helix length and bend and rotates 18° when it binds to the dsRNA hairpin substrate.

DISCUSSION

Although most dsRBDs bind to dsRNA, the finding that the binding of Rnt1p dsRBD to A/uGNN hairpins is a major determinant of target selection provides the first clear example of a binding specificity for a dsRBD (Chanfreau et al., 1998b, 2000; Nagel and Ares, 2000; Wu et al., 2004). Structural studies revealed that helix α1 recognizes the specific shape of this broad class of tetraloops (Wu et al., 2004). Thus, the discovery of a second class of tetraloops that did not conform to this minimal consensus and had a different free tetraloop structure led to the proposal that Rnt1p bound these substrates in a different way (Gaudin et al., 2006). Comparison of the dsRBD/AAGU structure, reported here, with the dsRBD/AGAA structure revealed that the AAGU hairpin has the same backbone fold in the complex as the AGNN tetraloops, and the dsRBD interactions and RDCs are the same for both complexes. We conclude that a conserved recognition mode is used for all Rnt1p substrates, regardless of their terminal loop sequences.

Conformational analysis of the free Rnt1p dsRBD (Leulliot et al., 2004) versus the dsRBD in the dsRBD/AAGU and dsRBD/AGAA (Wu et al., 2004) complexes revealed that helix α1 has a significant change in conformation upon binding to the tetraloop. We previously compared the structure of Rnt1p dsRBD in complex with the AGAA hairpin to that of a nonspecific complex of XlrpbA dsRBD with dsRNA (Wu et al., 2004). We noted that the two dsRBDs had a difference of ∼15° in the orientation of helix α1 which positions the Rnt1p dsRBD helix α1 to fit perfectly into the minor groove of the AGNN tetraloop and the top of the stem without changing the spacing of contacts to the minor groove and major groove, 1 and 0.5 turns away, respectively. Interestingly, the structure of the free Rnt1p dsRBD is similar to the structure of XlrpbA dsRBD in complex with dsRNA, with an rmsd of 0.41 Å (Figure S6A). Thus, the conformational change in helix α1 may be a key factor in the specific recognition of Rnt1p substrates.

Conformational Change in the AAGU Tetraloop upon dsRBD Binding

For the AGAA tetraloop, the positions of the bases in the free versus bound are very similar, although there is some change in the backbone on the 3′ side of the loop (Figure 5D). Because the structures of the hairpins capped by AGAA, AGUU, and UGCA tetraloops, which are all substrates for Rnt1p, all had a similar fold with a *syn* G (Lebars et al., 2001; Wu et al., 2001) and this fold was retained in the dsRBD/AGAA complex (Wu et al., 2004), it was proposed that the dsRBD recognized the conserved shape of the tetraloop. It was therefore surprising to find that for the AAGU hairpin, the positions of the bases and the backbone trajectory both change significantly in the complex (Figure 5C). Thus, it appears that the AAGU tetraloop and helix α1 of the dsRBD cooperatively fold to form a specific complex with a conserved tetraloop fold. In the complexes, these two
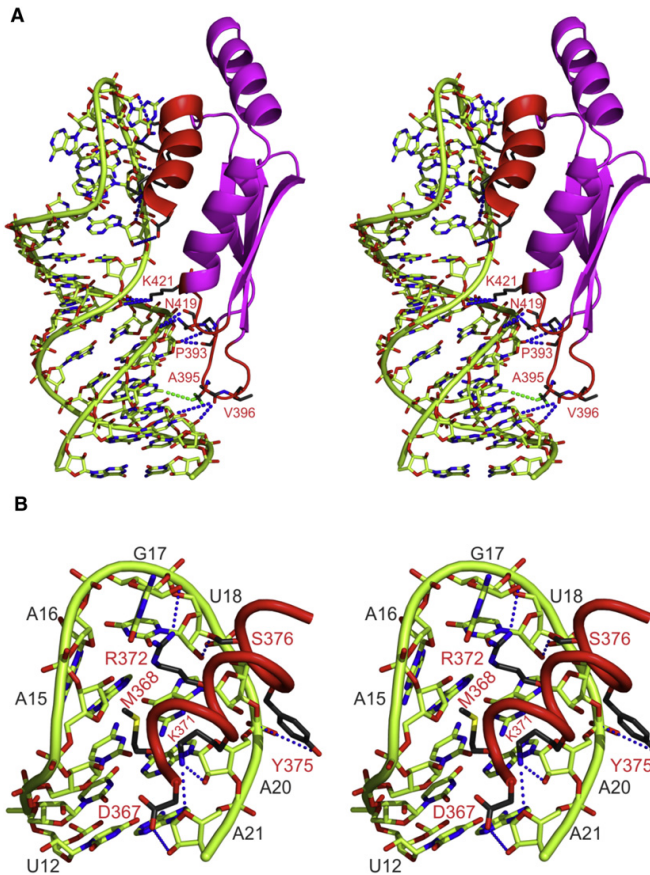
Comparison with Other dsRBD/RNA Complexes

Although the dsRBD is the second most abundant family of RNA recognition motifs, structures of only a few dsRBDs in complex with RNA have been solved. There are now six proteins for which the structures of both the free dsRBD and the dsRBD in complex with RNA have been reported. In addition to Rnt1p dsRBD (Leulliot et al., 2004; Wu et al., 2004; and this work), these include Staufen dsRBD (Bycroft et al., 1995; Ramos et al., 2000), TAR RNA binding protein 2 (TRBP2) (Yamashita et al., 2011), *Arabidopsis* HYL1 dsRBD (Yang et al., 2010), ADAR2 dsRBD1 and dsRBD2 (Stefl et al., 2006, 2010), and *Aquifex aeolicus* RNase III (Gan et al., 2006, 2008; Ramos et al., 2000; Ryter and Schultz, 1998). All of the free dsRBDs, with the exception of ADAR2 dsRBD1 and dsRBD2, superimpose well on each other and have virtually the same angle of helix α1 relative to the other secondary-structure elements (Figure S6). Furthermore, the conformations of the free and RNA-bound dsRBDs of HYL1, TRBP, Staufen, and *A. aeolicus* RNase III are the same, respectively, indicating that helix α1 does not change its conformation upon binding RNA. Of the complexes solved to date, only the dsRBD of Rnt1p and dsRBDs of ADAR2 have different helix α1 positions in complex with RNA relative to the free dsRBD (Figures S6I and S6J). The dsRBDs of ADAR2 have recently been shown to bind dsRNA in a sequence-specific manner, with base recognition via the minor groove from one amino acid each on helix α1 and the β1-β2 loop (Stefl et al., 2010). These two dsRBDs undergo relatively large conformational changes upon RNA binding, similar to Rnt1p. However, in contrast to Rnt1p dsRBD, the position of helix α1 in the free ADAR2 dsRBD1 and dsRBD2 is different compared to Xlrpba and the other dsRBDs (Figure S6).

Rnt1p requires specific tetraloop structures for substrate cleavage both in vivo and in vitro, whereas *A. aeolicus* RNase III, the homolog of *Escherichia coli* RNase III, cleaves dsRNA in vitro with little apparent sequence specificity. Crystal structures of *A. aeolicus* RNase III in complex with RNA have revealed

different tetraloops provide a rare example of two distinct RNA sequences that adopt the same functional fold (Zhang et al., 2010).

Whereas the conformational changes of the free versus bound AAGU tetraloop are larger than for the AGAA tetraloop, both the free and bound tetraloops have features in common that are likely essential for recognition and binding. In all cases, the backbone turns after the second nucleotide, and the position of the backbone in the turn is the same. On the 5′ side of the tetraloop, the first two bases point into the major groove and are stacked on each other. In the complexes, these two bases have no contacts to the dsRBD and the third base is positioned above the binding site. Finally, we note that the ACAA tetraloop has been proposed to have a similar conformation to the AGAA (Staple and Butcher, 2003). However, hairpins capped by ACAA are not cleaved by Rnt1p (Wu et al., 2001). In the ensemble of ACAA tetraloop structures (Staple and Butcher, 2003), about half have a backbone conformation at the turn that is very different from the AGAA and AAGU tetraloops, such that helix α1 would not be able to insert into the minor groove.
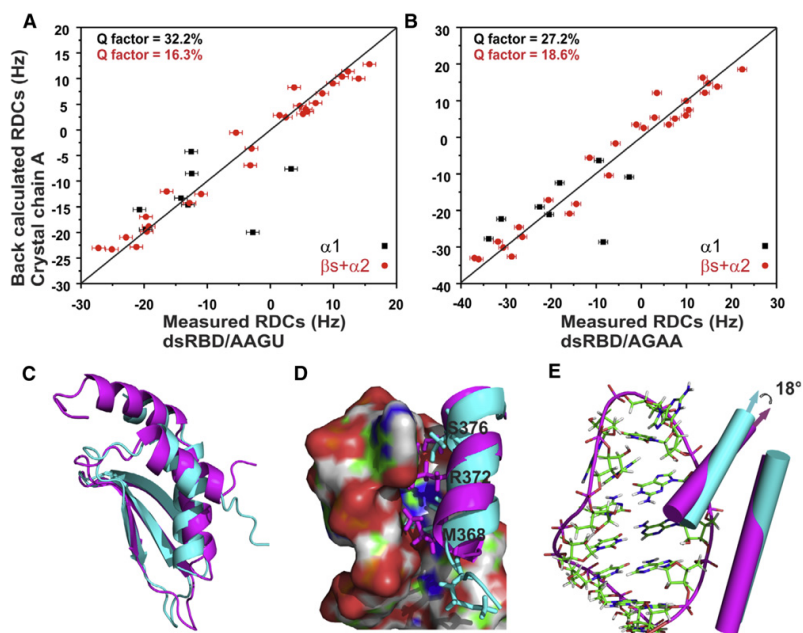
Figure 7. Comparison of the Structures of Free dsRBD and RNA-Bound dsRBD

(A and B) Correlation plots between experimental RDCs for the dsRBD secondary-structure elements in the (A) dsRBD/AAGU complex versus the RDCs calculated for the structure of the free dsRBD (PDB ID code 1T4O chain A) and (B) dsRBD/AGAA complex versus the RDCs calculated for the structure of the free dsRBD. For the correlation plots, the order tensor was determined from secondary-structure elements α2, β1, β2, and β3. RDC values are shown as black squares (α1) and red circles (α2, β1, β2, β3). Q factors were calculated for secondary-structure elements α1, α2, β1, β2, and β3 (black numbers) and for α2, β1, β2, and β3 (red numbers). Error bars are ±1 Hz, which is the standard deviation of the RDC measurement.

(C) Superposition of the free dsRBD and the dsRBD bound to the AAGU hairpin. Superposition is on the secondary-structure elements α2, β1, β2, and β3.

(D) Close-up view showing the interaction of α1 with the minor groove of the AAGU tetraloop and comparison to the free dsRBD. The helices are shown as ribbons, and the conserved side chains M368, R372, and S376 in the free and bound dsRBD are shown as sticks. The RNA is shown as a solvent-accessible surface.

(E) Comparison of the angle of helix α1 in the free and dsRBD-bound AAGU complex. The free dsRBD is in cyan and the bound dsRBD in the AAGU hairpin complex is in magenta.

that, in addition to non-sequence-specific contacts to the backbone, three bases have direct contacts to the dsRBD, two in helix α1 and one in the β1-β2 loop (Gan et al., 2006). One of these, Q157, is conserved in all bacterial RNase IIIs, and deletion of it abolished cleavage and binding. The equivalent residue in Rnt1p does not contact the RNA. The other two residues, including *A. aeolicus* RNase III Q161 in helix α1, have been proposed to give rise to sequence-specific binding (Stefl et al., 2010). Of the sequence- or tetraloop-specific dsRBD/RNA complexes solved to date, *A. aeolicus* RNase III is the only example where there is no significant change in the orientation of the dsRBD helix α1 upon binding to RNA.

In conclusion, our results show that the noncanonical AAGU tetraloop adopts a canonical fold upon binding to the dsRBD and that reorientation of helix α1 plays a major role in substrate-specific recognition. We propose that the Rnt1p dsRBD initially binds nonspecifically to dsRNA and scans along the RNA until it reaches an A/uGNN or AAGU tetraloop. Helix α1 is locked into position by the tetraloop fold like a ball in a glove, allowing subsequent positioning of the active site of Rnt1p at the cleavage site 14–16 bp away.

EXPERIMENTAL PROCEDURES

NMR Sample Preparation

The Rnt1p dsRBD, consisting of residues 366–453, was expressed as a glutathione transferase (GST) fusion protein and purified essentially as described (Wu et al., 2004), except for the addition of 1 mM DTT to the gel-filtration purification step. Details of the purification are given in Supplemental Experimental Procedures. NMR samples were ~1 mM dsRBD in 20 mM sodium phosphate (pH 6.5), 150 mM NaCl, 1 mM DTT. For NMR binding studies, the 32 nt AGAA (Figure 3A), AAGU, or UUCG hairpins were prepared by in vitro transcription using His$_6$-tagged mutant T7 polymerase (P266L) (Guillerez et al., 2005) with a synthetic DNA template and purified on denaturing gels as described (Wu et al., 2001). Unlabeled, uniformly ^{13}C,^{15}N-labeled, and A-, U-, G-, or C-^{13}C,^{15}N-labeled AAGU hairpins were used for structure determination of the dsRBD/AAGU complex. The dsRBD/AAGU complex was prepared at a 1.1:1 ratio (RNA:protein) by adding the dsRBD to the RNA under dilute conditions followed by concentration in NMR buffer to 1 mM complex.

NMR Spectroscopy and Structure Calculations

All NMR spectra were recorded at 25°C on Bruker DRX 500 and 600 MHz spectrometers, except for 2D NOESY spectra of exchangeable proton resonances of RNA, which were recorded at 10°C. The assignments of the Rnt1p dsRBD in the complex were derived from the analysis of 3D CBCANH, 3D CBCA(CO)NH, 3D HCCH-TOCSY, 3D HCCH-COSY, 3D ^{13}C-NOESY-HSQC,

and 3D ^{15}N-NOESY-HSQC experiments (Grzesiek and Bax, 1993; Kay et al., 1994; Schleucher et al., 1994) acquired on ^{13}C,^{15}N-labeled dsRBD in complex with unlabeled AAGU hairpin. The assignments of the AAGU hairpin were derived from 2D HCCH-COSY, 3D HCCH-TOCSY, 2D NOESY, 2D TOCSY (Cromsigt et al., 2001), and a suite of 2D filtered/edited NOESY (Peterson et al., 2004) using unlabeled dsRBD with A-, -G-, -U-, or -C-^{13}C,^{15}N-labeled AAGU. Finally, intermolecular NOEs were derived from 2D filtered/edited NOESY experiments as described (Peterson et al., 2004). One-bond ^{1}H-^{15}N RDCs were measured from HSQC-IPAP experiments (Ottiger et al., 1998) in the presence and absence of C12E5/hexanols (Ruckert and Otting, 2000) on a 600 MHz spectrometer. A total of 84, 81, and 83 RDCs were obtained for the free dsRBD, dsRBD/AGAA complex (Wu et al., 2004), and dsRBD/AAGU complex, respectively. Structure calculations were performed essentially as described (Peterson et al., 2004), and details are given in Supplemental Experimental Procedures. For comparison purposes, the dsRBD/AGAA complex was re-refined with the larger set of RDCs (81 versus 43).

Determination of Apparent K_D from ^{1}H-^{15}N HSQC Chemical Shift Titrations

The AAGU, AGAA, and UUCG hairpins were individually titrated into 0.1 mM ^{15}N-labeled dsRBD samples prepared in 500 μl high-salt NMR buffer (20 mM sodium phosphate [pH 6.5], 300 mM NaCl, 1 mM DTT) up to RNA:protein ratios of 2:1 (Figure 1). The higher-salt conditions (300 mM NaCl), instead of the 150 mM NaCl used for the structure studies, were used in order to minimize nonspecific binding. ^{1}H-^{15}N HSQC spectra were recorded for each titration point. The apparent dissociation constant K_D was obtained from changes in weighted chemical shift differences $\Delta\delta(N,H) = [(\Delta\delta(H_N))^2 + (\Delta\delta(N_H)/4)^2]^{1/2}$, assuming a one-site binding model. The titration curves were fitted globally using the following equation (Fielding, 2007):

$$\Delta\delta(N, H) = \left[\Delta\delta(N,H)_{max}/2P_0\right]\left[(P_0 + L_0 + K_D) - \left[(P_0 + L_0 + K_D)^2 - 4P_0L_0\right]^{1/2}\right],$$

where $\Delta\delta(N,H)_{max}$ is the average chemical shift difference between the free and bound forms, and P_0 and L_0 are the total concentration of dsRBD and AAGU hairpin, respectively.

Cleavage Kinetics Assays

Full-length Rnt1p was expressed with an N-terminal His$_6$ tag in BL-21 (DE3) Gold cells and purified on a GE Healthcare HisTrap Ni^{2+}-affinity column, followed by anion-exchange (HiTrap Q) and gel-filtration (HiLoad S75) chromatography. Purified Rnt1p was concentrated to ~5 mg/ml. For kinetics assays, 52 nt RNA hairpins snR47-AGAA, snR47-AAGU, or snR47-UUCG (Figure 2A) were ^{32}P end labeled with T4 polynucleotide kinase. Cleavage reactions were prepared under single-turnover conditions with 25 nM RNA and 1 μM Rnt1p in 20 mM Tris (pH 8.0), 150 mM NaCl at 25°C, and reactions were initiated by adding MgCl$_2$ to a final concentration of 5 mM. Ten microliter aliquots were removed at time points of 0.25, 0.5, 1, 2, 4, and 8 min, and quenched with 10 μl of formamide gel-loading buffer with 20 mM EDTA. Samples were run on a 10% denaturing polyacrylamide gel (19:1 acrylamide:bisacrylamide), dried, and imaged on a Molecular Imager FX Pro Plus (Bio-Rad). Bands in the gel image corresponding to the uncleaved fraction of the substrate were quantified using ImageJ (NIH). Plotted values are the average of three experiments.

In Vivo Analysis of Tetraloop Mutants

Tetraloop mutants (AAGU or UUCG) were inserted into the tetraloop upstream from the snR47 snoRNA gene using the delitto perfetto method (Storici et al., 2001). A core Kan^R-URA3 cassette was inserted between the second and third positions of the snR47 snoRNA tetraloop, and double-stranded DNA oligonucleotides were used to excise the core sequence and introduce the AAGU or UUCG sequence. Genomic DNA sequences were confirmed by sequencing. Strains were grown in YPD and harvested, and northern blot and primer extension analysis were performed as described (Chanfreau et al., 1998a; Henras et al., 2005).

ACCESSION NUMBERS

Coordinates and restraints for the 16 lowest-energy structures of the Rnt1p dsRBD/AAGU complex have been deposited in the Protein Data Bank under ID code 2LBS, and chemical shifts have been deposited in the BioMagResBank under accession number 17574.

SUPPLEMENTAL INFORMATION

Supplemental Information includes Supplemental Experimental Procedures, six figures, and one table and can be found with this article online at doi:10. 1016/j.str.2011.03.022.

REFERENCES

Bycroft, M., Grunert, S., Murzin, A.G., Proctor, M., and St Johnston, D. (1995). NMR solution structure of a dsRNA binding domain from *Drosophila* staufen protein reveals homology to the N-terminal domain of ribosomal protein S5. EMBO J. *14*, 3563–3571.

Catala, M., Tremblay, M., Samson, E., Conconi, A., and Abou Elela, S. (2008). Deletion of Rnt1p alters the proportion of open versus closed rRNA gene repeats in yeast. Mol. Cell. Biol. *28*, 619–629.

Chanfreau, G., Legrain, P., and Jacquier, A. (1998a). Yeast RNase III as a key processing enzyme in small nucleolar RNAs metabolism. J. Mol. Biol. *284*, 975–988.

Chanfreau, G., Rotondo, G., Legrain, P., and Jacquier, A. (1998b). Processing of a dicistronic small nucleolar RNA precursor by the RNA endonuclease Rnt1. EMBO J. *17*, 3726–3737.

Chanfreau, G., Buckle, M., and Jacquier, A. (2000). Recognition of a conserved class of RNA tetraloops by *Saccharomyces cerevisiae* RNase III. Proc. Natl. Acad. Sci. USA *97*, 3142–3147.

Conrad, C., and Rauhut, R. (2002). Ribonuclease III: new sense from nuisance. Int. J. Biochem. Cell Biol. *34*, 116–129.

Cornilescu, G., Marquardt, J.L., Ottiger, M., and Bax, A. (1998). Validation of protein structure from anisotropic carbonyl chemical shifts in a dilute liquid crystalline phase. J. Am. Chem. Soc. *120*, 6836–6837.

Cromsigt, J., van Buuren, B., Schleucher, J., and Wijmenga, S. (2001). Resonance assignment and structure determination for RNA. Methods Enzymol. *338*, 371–399.

Danin-Kreiselman, M., Lee, C.Y., and Chanfreau, G. (2003). RNAse III-mediated degradation of unspliced pre-mRNAs and lariat introns. Mol. Cell *11*, 1279–1289.

Doyle, M., and Jantsch, M.F. (2002). New and old roles of the double-stranded RNA-binding domain. J. Struct. Biol. *140*, 147–153.

Drinnenberg, I.A., Weinberg, D.E., Xie, K.T., Mower, J.P., Wolfe, K.H., Fink, G.R., and Bartel, D.P. (2009). RNAi in budding yeast. Science *326*, 544–550.

Elela, S.A., Igel, H., and Ares, M., Jr. (1996). RNase III cleaves eukaryotic pre-ribosomal RNA at a U3 snoRNP-dependent site. Cell *85*, 115–124.

El Hage, A., Koper, M., Kufel, J., and Tollervey, D. (2008). Efficient termination of transcription by RNA polymerase I requires the 5′ exonuclease Rat1 in yeast. Genes Dev. *22*, 1069–1081.

Fielding, L. (2007). NMR methods for the determination of protein-ligand dissociation constants. Prog. Nucl. Magn. Reson. Spectrosc. *51*, 219–242.

Gan, J., Tropea, J.E., Austin, B.P., Court, D.L., Waugh, D.S., and Ji, X. (2005). Intermediate states of ribonuclease III in complex with double-stranded RNA. Structure *13*, 1435–1442.

21

Gan, J., Tropea, J.E., Austin, B.P., Court, D.L., Waugh, D.S., and Ji, X. (2006). Structural insight into the mechanism of double-stranded RNA processing by ribonuclease III. Cell *124*, 355–366.

Gan, J., Shaw, G., Tropea, J.E., Waugh, D.S., Court, D.L., and Ji, X. (2008). A stepwise model for double-stranded RNA processing by ribonuclease III. Mol. Microbiol. *67*, 143–154.

Gaudin, C., Ghazal, G., Yoshizawa, S., Elela, S.A., and Fourmy, D. (2006). Structure of an AAGU tetraloop and its contribution to substrate selection by yeast RNase III. J. Mol. Biol. *363*, 322–331.

Ghazal, G., and Elela, S.A. (2006). Characterization of the reactivity determinants of a novel hairpin substrate of yeast RNase III. J. Mol. Biol. *363*, 332–344.

Ghazal, G., Ge, D., Gervais-Bird, J., Gagnon, J., and Abou Elela, S. (2005). Genome-wide prediction and analysis of yeast RNase III-dependent snoRNA processing signals. Mol. Cell. Biol. *25*, 2981–2994.

Ghazal, G., Gagnon, J., Jacques, P.E., Landry, J.R., Robert, F., and Elela, S.A. (2009). Yeast RNase III triggers polyadenylation-independent transcription termination. Mol. Cell *36*, 99–109.

Grzesiek, S., and Bax, A. (1993). The importance of not saturating H$_2$O in protein NMR. Application to sensitivity enhancement and NOE measurements. J. Am. Chem. Soc. *115*, 12593–12594.

Guillerez, J., Lopez, P.J., Proux, F., Launay, H., and Dreyfus, M. (2005). A mutation in T7 RNA polymerase that facilitates promoter clearance. Proc. Natl. Acad. Sci. USA *102*, 5958–5963.

Hall, K.B. (2002). RNA-protein interactions. Curr. Opin. Struct. Biol. *12*, 283–288.

Henras, A.K., Bertrand, E., and Chanfreau, G. (2004). A cotranscriptional model for 3′-end processing of the *Saccharomyces cerevisiae* pre-ribosomal RNA precursor. RNA *10*, 1572–1585.

Henras, A.K., Sam, M., Hiley, S.L., Wu, H., Hughes, T.R., Feigon, J., and Chanfreau, G.F. (2005). Biochemical and genomic analysis of substrate recognition by the double-stranded RNA binding domain of yeast RNase III. RNA *11*, 1225–1237.

Ji, X. (2006). Structural basis for non-catalytic and catalytic activities of ribonuclease III. Acta Crystallogr. D Biol. Crystallogr. *62*, 933–940.

Ji, X. (2008). The mechanism of RNase III action: how Dicer dices. Curr. Top. Microbiol. Immunol. *320*, 99–116.

Kay, L.E., Xu, G.Y., and Yamazaki, T. (1994). Enhanced-sensitivity triple-resonance spectroscopy with minimal H$_2$O saturation. J. Magn. Reson. *109*, 129–133.

Ketting, R.F., Fischer, S.E., Bernstein, E., Sijen, T., Hannon, G.J., and Plasterk, R.H. (2001). Dicer functions in RNA interference and in synthesis of small RNA involved in developmental timing in *C. elegans*. Genes Dev. *15*, 2654–2659.

Kharrat, A., Macias, M.J., Gibson, T.J., Nilges, M., and Pastore, A. (1995). Structure of the dsRNA binding domain of *E. coli* RNase III. EMBO J. *14*, 3572–3584.

Knight, S.W., and Bass, B.L. (2001). A role for the RNase III enzyme DCR-1 in RNA interference and germ line development in *Caenorhabditis elegans*. Science *293*, 2269–2271.

Kufel, J., Dichtl, B., and Tollervey, D. (1999). Yeast Rnt1p is required for cleavage of the pre-ribosomal RNA in the 3′ ETS but not the 5′ ETS. RNA *5*, 909–917.

Lamontagne, B., and Elela, S.A. (2004). Evaluation of the RNA determinants for bacterial and yeast RNase III binding and cleavage. J. Biol. Chem. *279*, 2231–2241.

Lamontagne, B., Tremblay, A., and Abou Elela, S. (2000). The N-terminal domain that distinguishes yeast from bacterial RNase III contains a dimerization signal required for efficient double-stranded RNA cleavage. Mol. Cell. Biol. *20*, 1104–1115.

Lamontagne, B., Larose, S., Boulanger, J., and Elela, S.A. (2001). The RNase III family: a conserved structure and expanding functions in eukaryotic dsRNA metabolism. Curr. Issues Mol. Biol. *3*, 71–78.

Lamontagne, B., Ghazal, G., Lebars, I., Yoshizawa, S., Fourmy, D., and Elela, S.A. (2003). Sequence dependence of substrate recognition and cleavage by yeast RNase III. J. Mol. Biol. *327*, 985–1000.

Larose, S., Laterreur, N., Ghazal, G., Gagnon, J., Wellinger, R.J., and Elela, S.A. (2007). RNase III-dependent regulation of yeast telomerase. J. Biol. Chem. *282*, 4373–4381.

Lebars, I., Lamontagne, B., Yoshizawa, S., Aboul-Elela, S., and Fourmy, D. (2001). Solution structure of conserved AGNN tetraloops: insights into Rnt1p RNA processing. EMBO J. *20*, 7250–7258.

Lee, C.Y., Lee, A., and Chanfreau, G. (2003a). The roles of endonucleolytic cleavage and exonucleolytic digestion in the 5′-end processing of *S. cerevisiae* box C/D snoRNAs. RNA *9*, 1362–1370.

Lee, Y., Ahn, C., Han, J., Choi, H., Kim, J., Yim, J., Lee, J., Provost, P., Radmark, O., Kim, S., and Kim, V.N. (2003b). The nuclear RNase III Drosha initiates microRNA processing. Nature *425*, 415–419.

Leulliot, N., Quevillon-Cheruel, S., Graille, M., van Tilbeurgh, H., Leeper, T.C., Godin, K.S., Edwards, T.E., Sigurdsson, S.T., Rozenkrants, N., Nagel, R.J., et al. (2004). A new α-helical extension promotes RNA binding by the dsRBD of Rnt1p RNAse III. EMBO J. *23*, 2468–2477.

Lipsitz, R.S., and Tjandra, N. (2004). Residual dipolar couplings in NMR structure analysis. Annu. Rev. Biophys. Biomol. Struct. *33*, 387–413.

MacRae, I.J., and Doudna, J.A. (2007). Ribonuclease revisited: structural insights into ribonuclease III family enzymes. Curr. Opin. Struct. Biol. *17*, 138–145.

Nagel, R., and Ares, M., Jr. (2000). Substrate recognition by a eukaryotic RNase III: the double-stranded RNA-binding domain of Rnt1p selectively binds RNA containing a 5′-AGNN-3′ tetraloop. RNA *6*, 1142–1156.

Nanduri, S., Carpick, B.W., Yang, Y., Williams, B.R., and Qin, J. (1998). Structure of the double-stranded RNA-binding domain of the protein kinase PKR reveals the molecular basis of its dsRNA-mediated activation. EMBO J. *17*, 5458–5465.

Nicholson, A.W. (1999). Function, mechanism and regulation of bacterial ribonucleases. FEMS Microbiol. Rev. *23*, 371–390.

Nowotny, M., and Yang, W. (2009). Structural and functional modules in RNA interference. Curr. Opin. Struct. Biol. *19*, 286–293.

Ottiger, M., Delaglio, F., and Bax, A. (1998). Measurement of J and dipolar couplings from simplified two-dimensional NMR spectra. J. Magn. Reson. *131*, 373–378.

Peterson, R.D., Theimer, C.A., Wu, H., and Feigon, J. (2004). New applications of 2D filtered/edited NOESY for assignment and structure elucidation of RNA and RNA-protein complexes. J. Biomol. NMR *28*, 59–67.

Prescott, E.M., Osheim, Y.N., Jones, H.S., Alen, C.M., Roan, J.G., Reeder, R.H., Beyer, A.L., and Proudfoot, N.J. (2004). Transcriptional termination by RNA polymerase I requires the small subunit Rpa12p. Proc. Natl. Acad. Sci. USA *101*, 6068–6073.

Ramos, A., Grunert, S., Adams, J., Micklem, D.R., Proctor, M.R., Freund, S., Bycroft, M., St Johnston, D., and Varani, G. (2000). RNA recognition by a Staufen double-stranded RNA-binding domain. EMBO J. *19*, 997–1009.

Ruckert, M., and Otting, G. (2000). Alignment of biological macromolecules in novel nonionic liquid crystalline media for NMR experiments. J. Am. Chem. Soc. *122*, 7793–7797.

Ryter, J.M., and Schultz, S.C. (1998). Molecular basis of double-stranded RNA-protein interactions: structure of a dsRNA-binding domain complexed with dsRNA. EMBO J. *17*, 7505–7513.

Schleucher, J., Schwendinger, M., Sattler, M., Schmidt, P., Schedletzky, O., Glaser, S.J., Sorensen, O.W., and Griesinger, C. (1994). A general enhancement scheme in heteronuclear multidimensional NMR employing pulsed field gradients. J. Biomol. NMR *4*, 301–306.

Shi, Z., Nicholson, R.H., Jaggi, R., and Nicholson, A.W. (2011). Characterization of *Aquifex aeolicus* ribonuclease III and the reactivity epitopes of its pre-ribosomal RNA substrates. Nucleic Acids Res. *39*, 2756–2768.

Staple, D.W., and Butcher, S.E. (2003). Solution structure of the HIV-1 frameshift inducing stem-loop RNA. Nucleic Acids Res. *31*, 4326–4331.

22

Stefl, R., Xu, M., Skrisovska, L., Emeson, R.B., and Allain, F.H. (2006). Structure and specific RNA binding of ADAR2 double-stranded RNA binding motifs. Structure 14, 345–355.

Stefl, R., Oberstrass, F.C., Hood, J.L., Jourdan, M., Zimmermann, M., Skrisovska, L., Maris, C., Peng, L., Hofr, C., Emeson, R.B., and Allain, F.H. (2010). The solution structure of the ADAR2 dsRBM-RNA complex reveals a sequence-specific readout of the minor groove. Cell 143, 225–237.

Storici, F., Lewis, L.K., and Resnick, M.A. (2001). In vivo site-directed mutagenesis using oligonucleotides. Nat. Biotechnol. 19, 773–776.

Sun, W., Pertzev, A., and Nicholson, A.W. (2005). Catalytic mechanism of Escherichia coli ribonuclease III: kinetic and inhibitor evidence for the involvement of two magnesium ions in RNA phosphodiester hydrolysis. Nucleic Acids Res. 33, 807–815.

Wu, H., Yang, P.K., Butcher, S.E., Kang, S., Chanfreau, G., and Feigon, J. (2001). A novel family of RNA tetraloop structure forms the recognition site for Saccharomyces cerevisiae RNase III. EMBO J. 20, 7240–7249.

Wu, H., Henras, A., Chanfreau, G., and Feigon, J. (2004). Structural basis for recognition of the AGNN tetraloop RNA fold by the double-stranded RNA-binding domain of Rnt1p RNase III. Proc. Natl. Acad. Sci. USA 101, 8307–8312.

Wu, H., Finger, L.D., and Feigon, J. (2005). Structure determination of protein/RNA complexes by NMR. Methods Enzymol. 394, 525–545.

Yamashita, S., Nagata, T., Kawazoe, M., Takemoto, C., Kigawa, T., Güntert, P., Kobayashi, N., Terada, T., Shirouzu, M., Wakiyama, M., et al. (2011). Structures of the first and second double-stranded RNA-binding domains of human TAR RNA-binding protein. Protein Sci. 20, 118–130.

Yang, S.W., Chen, H.Y., Yang, J., Machida, S., Chua, N.H., and Yuan, Y.A. (2010). Structure of Arabidopsis HYPONASTIC LEAVES1 and its molecular implications for miRNA processing. Structure 18, 594–605.

Zhang, Q., Kim, N.K., Peterson, R.D., Wang, Z., and Feigon, J. (2010). Structurally conserved five nucleotide bulge determines the overall topology of the core domain of human telomerase RNA. Proc. Natl. Acad. Sci. USA 107, 18761–18768.

Zweckstetter, M., and Bax, A. (2000). Prediction of sterically induced alignment in a dilute liquid crystalline phase: aid to protein structure determination by NMR. J. Am. Chem. Soc. 122, 3791–3792.

23

2.1   Supplemental Information

Supplemental Information for

Structure of a yeast RNase III dsRBD complex with a non-canonical RNA substrate provides new insights into binding specificity of dsRBDs

Zhonghua Wang#, Elon Hartman#, Kevin Roy,
Guillaume Chanfreau, and Juli Feigon*

Department of Chemistry and Biochemistry, and Molecular Biology Institute,
P.O. Box 951569, University of California, Los Angeles, CA 90095-1569,
USA

#These authors contributed equally to this work.
*Author to whom correspondence should be addressed.
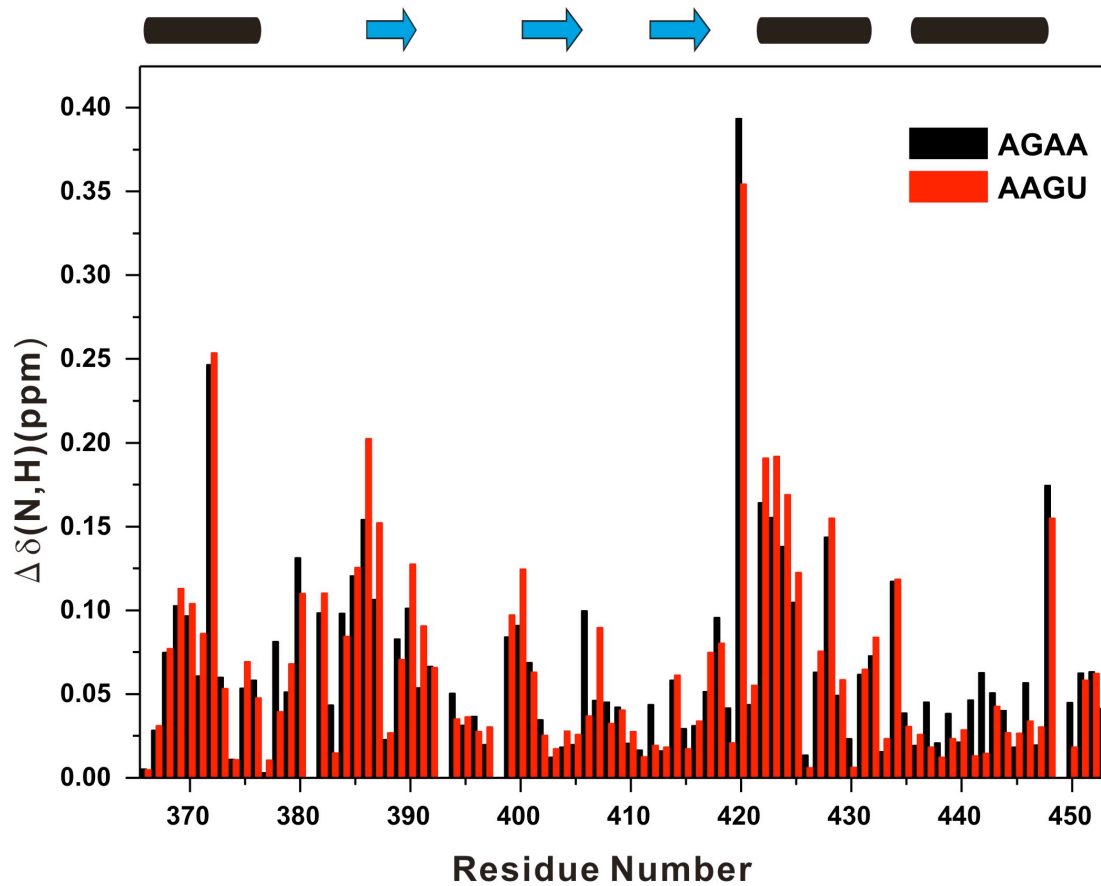
Figure S1, related to Figure 3 and 6. Plot of amide chemical shift changes for the Rnt1p dsRBD upon addition of AGAA (black) and AAGU (red) hairpins. Ratio of dsRBD to hairpin RNA is 1:1.1 in 150 mM KCl at the final titration point. ^{15}N and ^{1}H chemical shift change $\Delta\delta(N,H) = [(\Delta\delta(H_N)^2 + (\Delta\delta(N_H)/4)^2]^{\frac{1}{2}}$ is plotted against residue number.
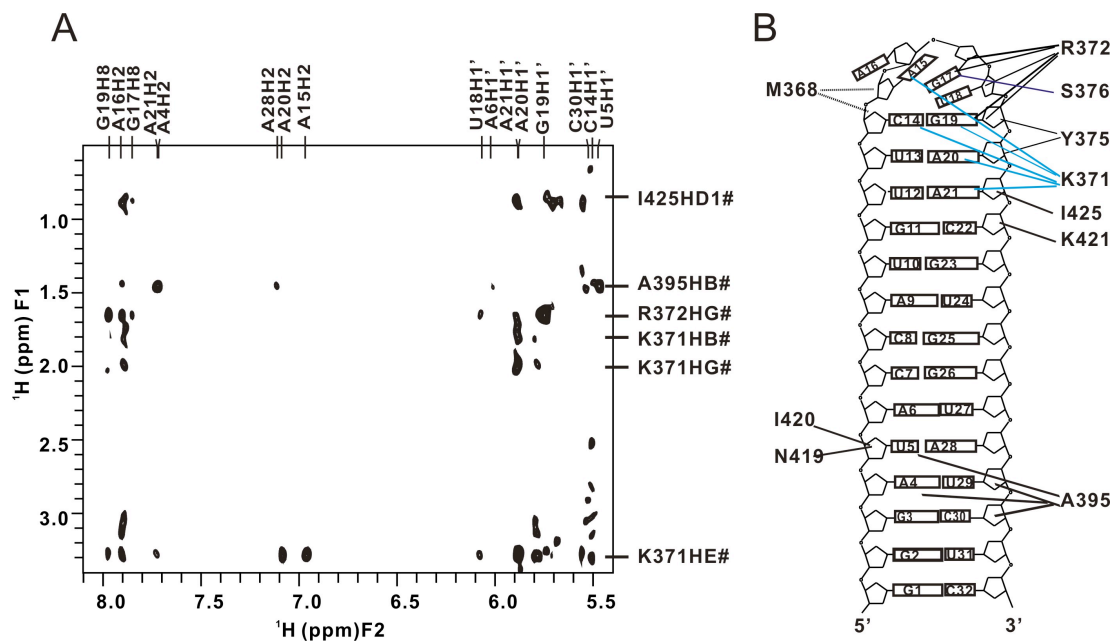
Figure S2, related to Figure 3 and Table 1. (A) Portion of an F2f NOESY spectrum acquired on a ^{13}C, ^{15}N labeled Rnt1p dsRBD with unlabeled AAGU sample in D_2O showing intermolecular NOEs. The interacting residues are labeled by residue type with number followed by atom type. (B) The AAGU tetraloop sequence and secondary structure with a schematic overview of intermolecular NOEs observed between Rnt1p dsRBD and AAGU hairpin.
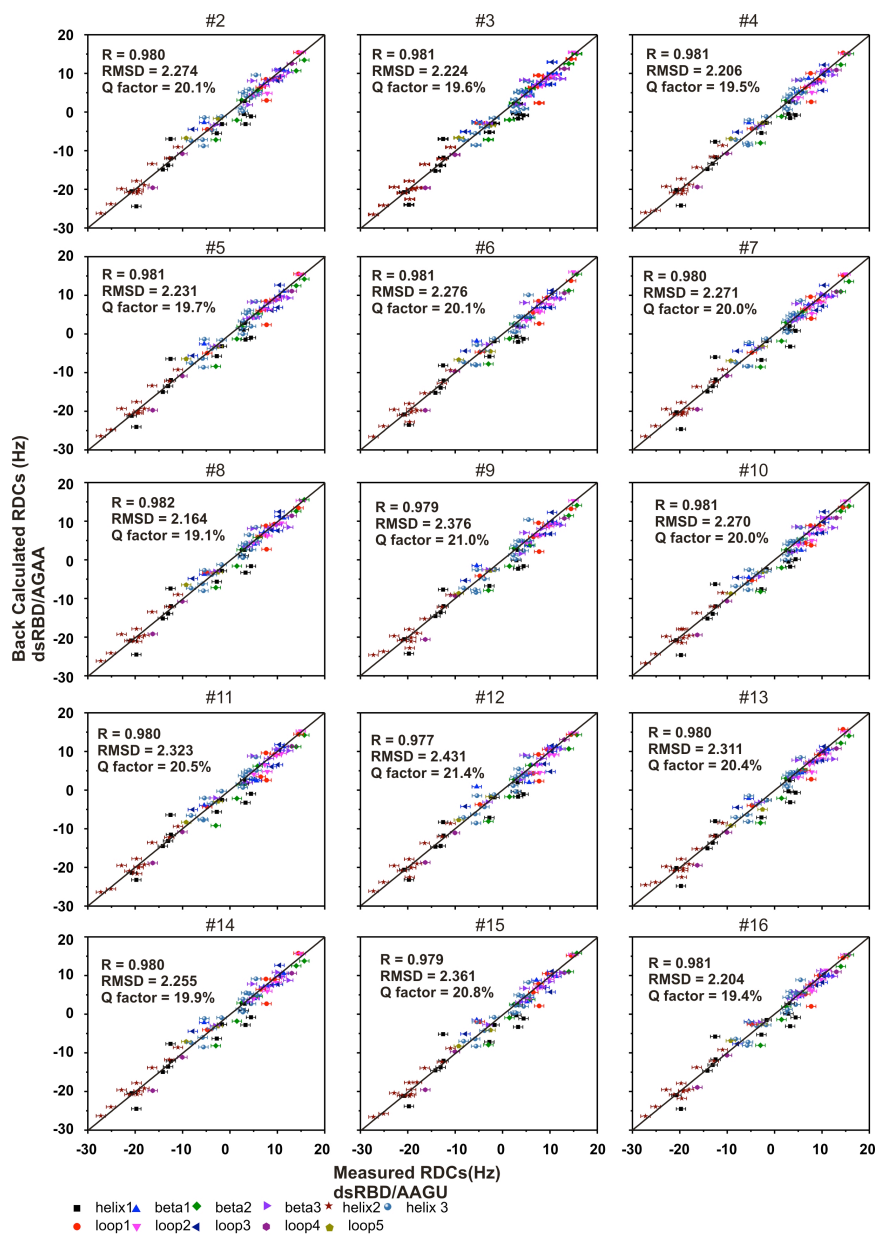
Figure S3, related to Figure 4. Correlation plots of RDC between experimental and back-calculated values for all ensemble structures. The experimental RDCs of the dsRBD from the dsRBD/AAGU RNA hairpin complex fit into other structures of the dsRBD in the dsRBD/AGAA RNA hairpin complex.
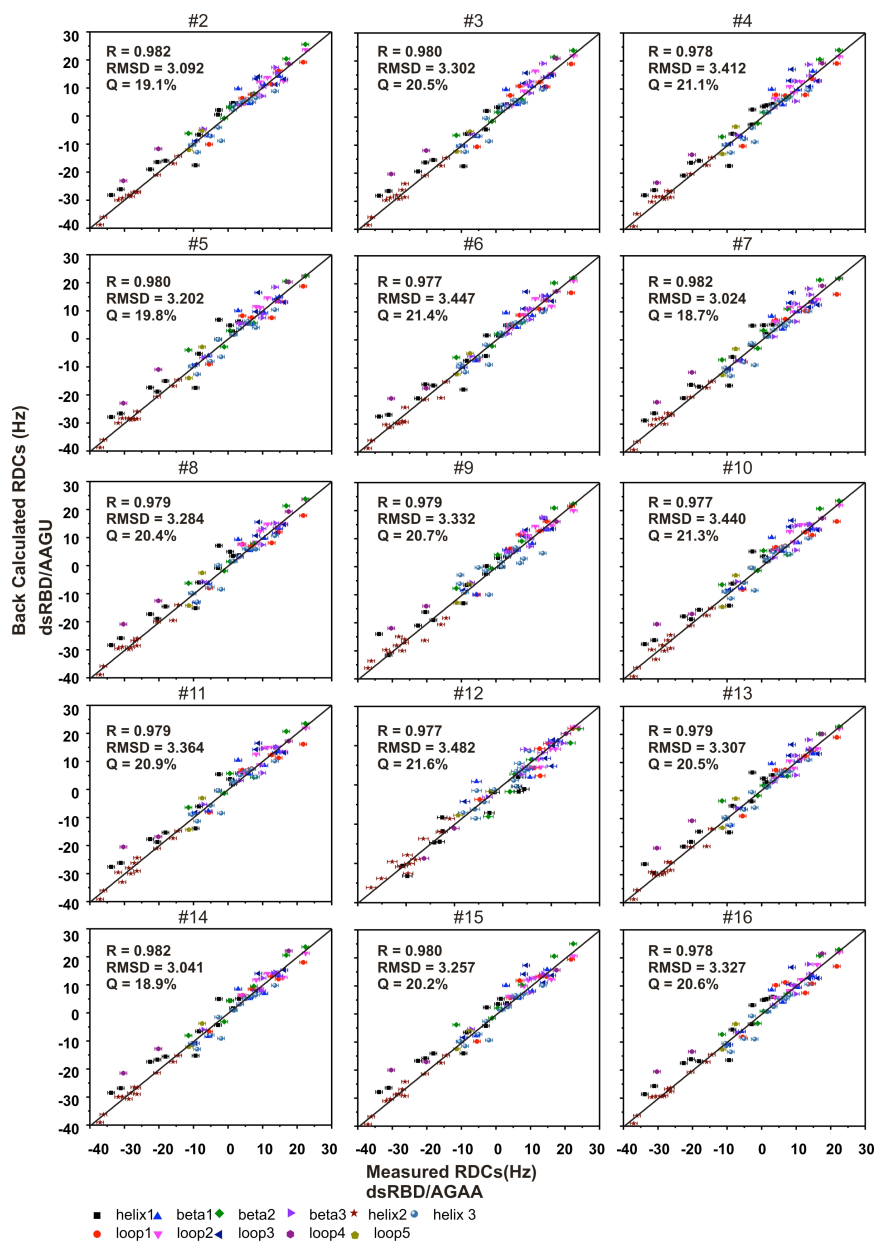
Figure S4, related to Figure 4. The correlation plots of RDC between experimental and back-calculated values for all ensemble structures. The experimental RDCs of the dsRBD from the dsRBD/AGAA RNA hairpin complex fit into other structures of the dsRBD in the dsRBD/AAGU RNA hairpin complex.
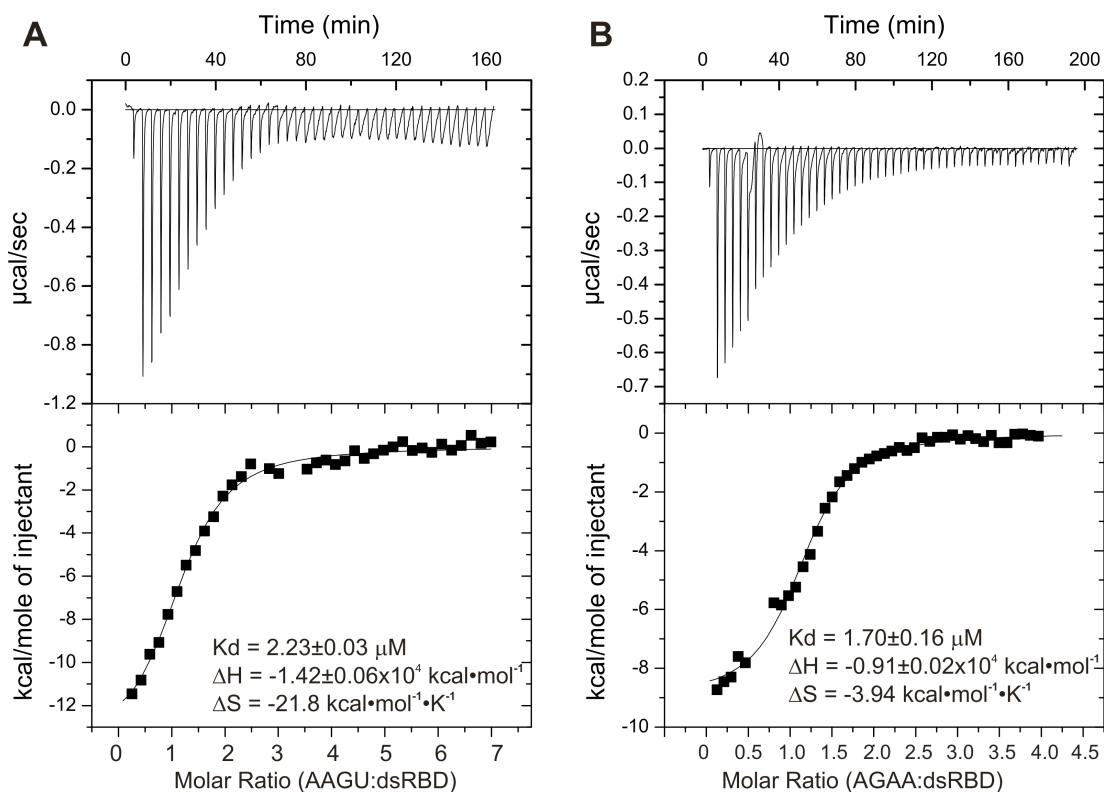
Figure S5, related to Figure 5. Representative isothermal titration calorimetry plots of dsRBD with (A) AAGU hairpin and (B) AGAA hairpin. Samples are in 300 mM NaCl, 20 mM NaPhosphate, pH 6.5. Data was fit to a one-site binding model. Both RNAs show approximately the same affinity. Note that K_Ds measured by ITC are about 2 μM, which is about an order of magnitude less than the apparent K_D values obtained by NMR. This difference is due to the different way in which the K_Ds are determined, but the relative values are the same.
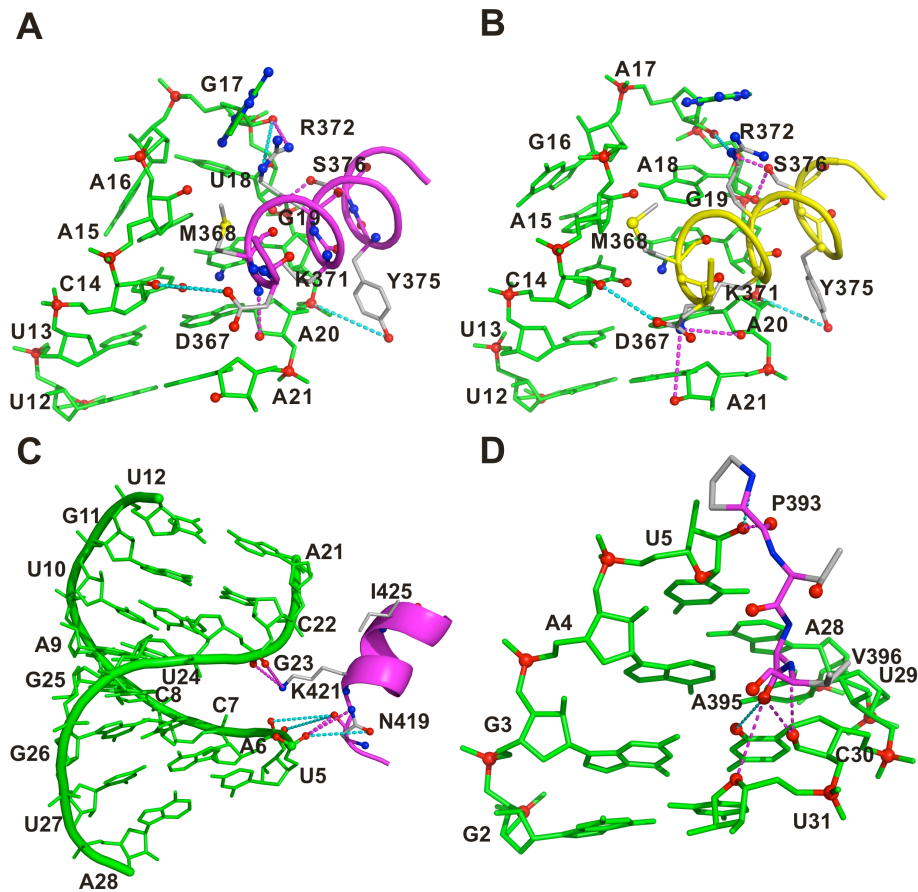
Figure S6, related to Figure 6. Interactions between the Rnt1p dsRBD and RNA. (A, B) Position of helix α1 and side chain interactions in the tetraloop minor groove of the (A) dsRBD/AAGU hairpin and (B) dsRBD/AGAA hairpin complexes. (C) Position of helix α2 and side chain interactions in the RNA stem major groove in the dsRBD/AAGU hairpin complex. (D) Position of the β1-β2 loop and side chain interactions in the RNA stem minor groove in the dsRBD/AAGU hairpin complex. The dsRBD bound to AAGU hairpin is magenta and to AGAA hairpin is orange, the amino acids side chains that interact with RNA are shown in gray sticks, oxygen is red and nitrogen is blue. The RNA is green sticks with oxygens in red. Dashed lines connect heavy atoms that are <3 Å (pink) and <5 Å (blue) corresponding to potential hydrogen bonds and water mediated hydrogen bonds, respectively.
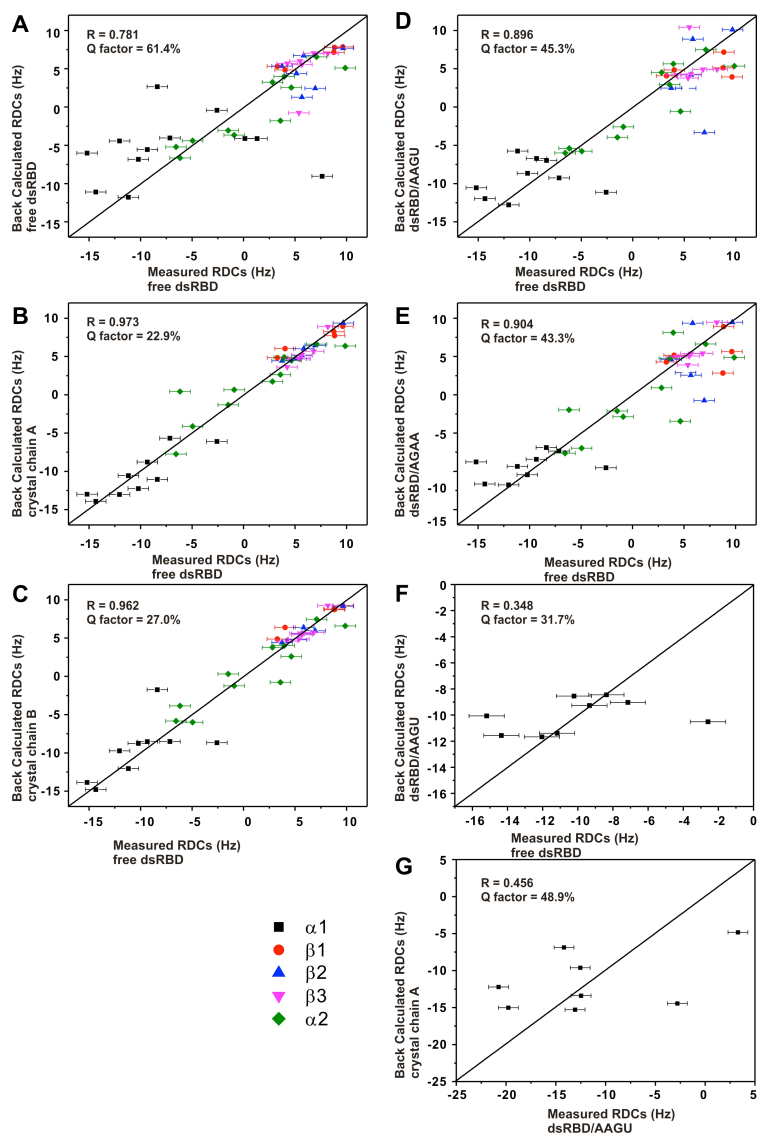
Figure S7, related to Figure 7. Correlation plots between experimental RDCs from the free dsRBD and back calculated RDCs to the structure of the (A) free dsRBD in solution, (B) dsRBD crystal structure chain A, (C) dsRBD crystal structure chain B, (D) AAGU/dsRBD complex, and (E) AGAA/dsRBD complex. The order tensor was determined from the secondary structure elements α1, β1, β2, β3, and α2. (F-G) Correlation plots between experimental RDCs from free dsRBD helix α1 and back-calculated RDCs to helix α1 in the (F) dsRBD/AAGU complex and (G) chain A of the crystal structure.

31
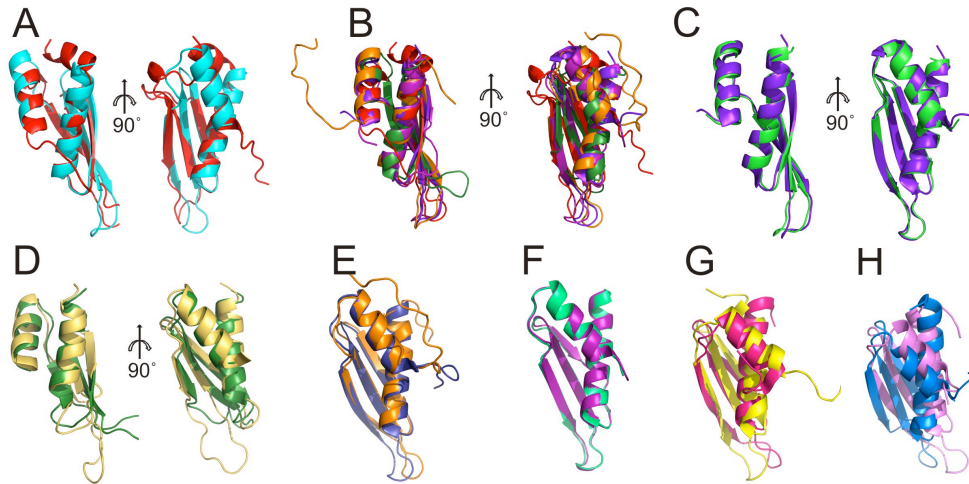
Figure S8, related to Figure 4 and 7. Structure comparison of free vs bound dsRBDs. All structures were aligned to α2β1β2β3. (A) Superposition of Xlrbpa (Cyan, PDB: 1DI2) and free Rnt1p dsRBD (Red, PDB: 1T4O). (B) Superposition of free structures of Rnt1p dsRBD (Red, PDB: 1T4O), Aa RNase III dsRBD (Purple blue, PDB: 2NUE), Arabidopsis HYL1 dsRBD (Purple, PDB: 3ADG), TAR RNA-binding protein 2 (TRBP2) (Orange, PDB: 2CPN) and Staufen dsRBD (Forest, PDB: 1STU). (C) Superposition of free (Purple blue, PDB: 2NUE) vs bound (Green, PDB: 2NUF) Aa RNase III dsRBD. (D) Superposition of staufen free (forest green, PDB: 1STU) vs bound dsBRD (yellow-orange, PDB: 1EKZ). (E) Superposition of TRBP2 free (orange, PDB: 2CPN) vs bound (deep blue, PDB: 3ADL). (F) Superposition of Arabidopsis HYL1 dsRBD free (purple, PDB: 3ADG) vs bound (light green, PDB: 3ADI). (G) Superposition of dsRBD1 of ADAR2 free (hot pink, PDB: 2B7T) vs bound (yellow, PDB: 2L3C). (H) Superposition of dsRBD2 of ADAR2 free (marine blue, PDB: 2B7V) vs bound (violet, PDB: 2L2K).
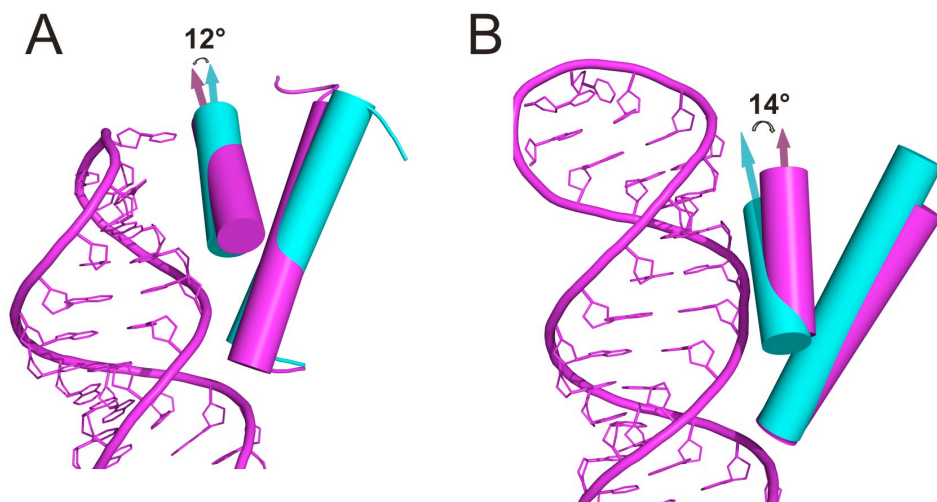
Figure S9, related to Figure 4 and 7. Comparison of the angle of helix α1 in the free and dsRBD bound ADAR2 complex. (A) dsRBD1 of ADAR2 (B) dsRBD2 of ADAR2. The free dsRBD is cyan and the bound dsRBD is magenta.

Table S1. Comparison of intermolecular NOEs in the dsRBD/AAGU and dsRBD/AGAA complexes

Resi#	Atom	dsRBD/AAGU	dsRBD/AGAA
371	HB#	20 H1'	18H2, 20H1'
	HG#	20 H1'	20H1', 20H2
	HD#	20 H1'	20H1', 20H2
	HE#	14H1', 18H1', 20H1', 20H2, 20H8, 15H2	14H1', 18H1', 20H1', 20H2, 20H8
372	HG#	17H8,17H1', 17H2',18H1', 18H2', 18H4', 18H6,19H8,19H1',19H2',19H4'	17H1',17H2',17H2,18H1',18H2', 18H2,18H3',18H8,19H1',19H8
	HD#	N/A	17H2
375	HD#	19H1', 19H5'#, 19H4', 20H5'#	19H5'#, 19H4'
	HE#	19H5'#, 19H4', 20H5'#, 20H4',	20H5'#, 20H4',
377	HD#	N/A	17H2, 18H2
395	HB#	5H1', 4H1', 4H2, 30H1', 28H2, 29H1'	5H1', 4H1', 4H2, 30H1', 28H2, 29H1'
419	HB#	5H3'	5H3'
420	HD1#	5H3', 5H5'#	5H3', 5H5'#
	HG2#	5H3', 5H5'#	5H3', 5H5'#
	HG1#	N/A	5H3', 5H5'#
421	HN	22 H5'#	22 H5'#
425	HG1#	21H4'	N/A
	HD1#	21H1', 21H4'	21H1', 21H4', 22H6

Supplemental Experimental Procedures

Rnt1p dsRBD sample preparation. The Rnt1p dsRBD, consisting of residues 366-453, was expressed as a glutathione transferase (GST) fusion protein containing a thrombin cleavage site in BL21 (DE3) Gold cells (Stratagene) and purified by glutathione-sepharose affinity chromatography. The purified GST-tagged dsRBD was cleaved using thrombin and the cleaved dsRBD was then purified using gel-filtration chromatography on a Superdex S75 column (GE Healthcare) with a running buffer as previously described [1] with the addition of 1 mM DTT (20 mM sodium phosphate, pH 6.5, 150 mM NaCl, 1mM DTT, referred to as NMR buffer). The purified dsRBD was then concentrated to ~1 mM using Amicon ultrafiltration.

NMR structure calculations For the structure determination of the dsRBD/AAGU complex, a total of 2095 and 695 experimental distance restraints for the dsRBD and AAGU hairpin, respectively, were obtained from NOE intensities and classified as strong (1.8-3.0 Å), medium (1.8-4.5 Å) and weak (1.8-6.0 Å). For the dsRBD, 148 dihedral angles were derived from TALOS [2]. For the AAGU hairpin, the ribose conformations and χ angles were analyzed as described [3]. Dihedral angles ($\alpha,\beta,\gamma,\varepsilon$) were included in structure calculations as described [1]. The structures were calculated using the NIH-Xplor package [4] following standard protocols. Briefly, the calculation started from extended protein and RNA conformations in random orientations and separated by 70 Å. The protein and RNA were then folded simultaneously during 40,000 steps of high temperature dynamics with a time step of 0.002 fs. The structures were cooled down using 75 ps of slow cooling from 2000K to 100K. The final structures were obtained after refinement with 83 RDCs during a second slow cooling from 1000 K to 100 K. The axial (-30 Hz) and rhombic (0.66) components of the alignment tensor were derived from a grid-search procedure [5]. The force constant for the RDCs was gradually increased from 0.001 to 0.2 Kcal.mol^{-1}.Hz^{-2}. The sixteen lowest energy structures were selected, and the structures were analyzed using MOLMOL [6] and PYMOL [7]. Hydrogen bonds between protein and RNA were calculated based on heavy atom distances and angles (<3.4 Å and >120º for direct and 5.0 Å for water mediated hydrogen bonds). For comparison purposes, the dsRBD/AGAA

complex was re-refined using same protocol as described [1] but with the larger set of RDCs (81 vs 43).

Isothermal Titration Calorimetry

All samples were dialyzed against high salt buffer (300 mM NaCl, 20mM NaPi at pH 6.5) before ITC experiments. The ITC experiments were performed using a VP-ITC instrument (Microcal) at 25ºC. For each experiment, we used 20uM dsRBD in 1.43ml sample cell, and titrated RNA (0.6mM) into dsRBD. All isotherms were fit using the OriginR v7.0 software (MicrocalTM). Data were corrected for heats of ligand dilution prior to fitting by globally subtracting the average of 3-5 data points from the saturated tail.

Supplemental References

1. Wu, H., Henras, A., Chanfreau, G., and Feigon, J. (2004). Structural basis for recognition of the AGNN tetraloop RNA fold by the double-stranded RNA-binding domain of Rnt1p RNase III. Proc Natl Acad Sci U S A *101*, 8307-8312.

2. Cornilescu, G., Delaglio, F., and Bax, A. (1999). Protein backbone angle restraints from searching a database for chemical shift and sequence homology. J Biomol NMR *13*, 289-302.

3. Wu, H., Yang, P.K., Butcher, S.E., Kang, S., Chanfreau, G., and Feigon, J. (2001). A novel family of RNA tetraloop structure forms the recognition site for Saccharomyces cerevisiae RNase III. EMBO J *20*, 7240-7249.

4. Schwieters, C.D., Kuszewski, J.J., Tjandra, N., and Clore, G.M. (2003). The Xplor-NIH NMR molecular structure determination package. J Magn Reson *160*, 65-73.

5. Clore, G.M., Gronenborn, A.M., and Tjandra, N. (1998). Direct structure refinement against residual dipolar couplings in the presence of rhombicity of unknown magnitude. J Magn Reson *131*, 159-162.

6. Koradi, R., Billeter, M., and Wuthrich, K. (1996). MOLMOL: a program for display and analysis of macromolecular structures. J Mol Graph *14*, 51-55, 29-32.

7. DeLano, W.L. (2002). The PyMOL Molecular Graphics System.

CHAPTER 3

Intrinsic dynamics of an extended hydrophobic core in the *S. cerevisiae* RNase III dsRBD contributes to recognition of specific RNA binding sites

3.1 Abstract

The *S. cerevisiae* RNase III enzyme Rnt1p preferentially binds to dsRNA hairpin substrates with a conserved (A/u)GNN tetraloop fold, via shape-specific interactions by its dsRBD helix $\alpha 1$ to the tetraloop minor groove. To investigate whether conformational flexibility in the dsRBD regulates the binding specificity, we determined the backbone dynamics of the Rnt1p dsRBD in the free and AGAA hairpin-bound states using NMR spin relaxation experiments. The intrinsic μs-ms timescale dynamics of the dsRBD suggests that helix $\alpha 1$ undergoes conformational sampling in the free state, with large dynamics at some residues in the $\alpha 1$-$\beta 1$ loop ($\alpha 1$-$\beta 1$ hinge). To correlate free dsRBD dynamics with structural changes upon binding, we determined the solution structure of the free dsRBD used in the previously determined RNA-bound structures. The Rnt1p dsRBD has an extended hydrophobic core comprising helix $\alpha 1$, the $\alpha 1$-$\beta 1$ loop, and helix $\alpha 3$. Analysis of the backbone dynamics and structures of the free and bound dsRBD reveals that slow-timescale dynamics in the $\alpha 1$-$\beta 1$ hinge are associated with concerted structural changes in the extended hydrophobic core that govern binding of helix $\alpha 1$ to AGAA tetraloops. The dynamic behavior of the dsRBD bound to a longer AGAA hairpin reveals that dynamics within the hydrophobic core differentiate between specific and nonspecific sites. Mutations of residues in the $\alpha 1$-$\beta 1$ hinge result in changes to the dsRBD stability and RNA-binding affinity, and cause defects in snoRNA processing *in vivo*. These results reveal that dynamics in the extended hydrophobic core are important for binding site selection by the Rnt1p dsRBD.

3.2 Introduction

RNase III enzymes process double-stranded RNA (dsRNA) substrates for many non-coding RNA precursors, including pre-rRNAs, -snoRNAs, and -snRNAs, as well as miRNA and siRNA.[1-3] RNase III family members typically have one or two

double-stranded RNA-binding domains (dsRBDs) and one or two endonuclease domains (endoNDs), which cleave dsRNA substrates as a dimer. Each endoND cleaves the backbone of one RNA strand via a two-Mg^{2+} catalytic mechanism, leaving a two-nucleotide $3'$ overhang on processed RNAs, a defining feature of RNase III cleavage.[4,5] In *S. cerevisiae*, Rnt1p is the only characterized RNase III enzyme, and is involved in the processing of the pre-rRNA precursor,[6,7] and of the precursors of many snoRNAs[8-10] and snRNAs.[11-14] For most of these non-coding RNAs, Rnt1p cleavage provides a site for subsequent processing by the Rat1p or Xrn1p exonucleases or the exosome.[14-17] Rnt1p activity is also important for the quality control of mRNA, processing unspliced mRNAs.[18,19] Rnt1p cleavage can influence transcription termination by cleaving stem-loop structures that are found downstream from normal polyadenylation signals.[20,21] Finally, Rnt1p cleavage limits the expression of a number of mRNAs.[15,22-24] Thus, Rnt1p activity controls the production of a large number of cellular transcripts. Rnt1p has a characteristic substrate specificity, cleaving the dsRNA stem of (A/u)GNN tetraloop hairpins 14 and 16 bp from the conserved tetraloop on its RNA targets.[25,26] Selective binding by the dsRBD to (A/u)GNN tetraloop hairpins, a unique feature of Rnt1p, determines target site selection.[26]

Although *S. cerevisiae* does not have RNAi machinery, other budding yeasts carry out RNAi with a Dicer, called Dcr1, which is evolutionarily related to Rnt1.[27] Dcr1 resembles Rnt1 in having a single endoND that dimerizes intermolecularly, unlike other eukaryotic Dicers, which have two tandem endoNDs that dimerize intramolecularly. The Dcr1 endoND is followed by a dsRBD, but has an additional dsRBD separated by a long linker sequence. How these dsRBDs contribute to substrate recognition and processing is unknown, although the endoND-adjacent dsRBD in Dcr1 is required for siRNA processing. Intriguingly, *Candida albicans* Dcr1 has been found to carry out both RNAi and Rnt1 functions.[28]

Canonical dsRBDs have an $\alpha\beta\beta\beta\alpha$ secondary structure motif and interact

with a broad range of dsRNA substrates. Residues in helix $\alpha 1$, the $\beta 1$-$\beta 2$ loop and helix $\alpha 2$ mediate interactions with successive RNA minor, major, and minor grooves on one face of the duplex, respectively.[29] The dsRBDs generally recognize dsRNA without any additional substrate specificity, a binding mode typified by the crystal structure of the Xlrbpa dsRBD in complex with A-form dsRNA.[30] In contrast, the structure of human ADAR dsRBD in complex with dsRNA revealed that this and other dsRBDs, notably *A. aeolicus* RNase III dsRBD, can have some sequence specificity for their dsRNA substrates though hydrophobic contacts between dsRBD side chains and nucleotide bases.[31] Additionally, some dsRBDs have a canonical dsRBD fold but do not independently bind to dsRNA with high affinity, such as the human Drosha dsRBD.[32]

The Rnt1p dsRBD is unique among dsRBDs studied to date in recognizing RNA hairpins capped by a tetraloop with the consensus sequence (A/u)GNN,[25] through structure-specific recognition of the tetraloop fold by helix $\alpha 1$, with no base-specific contacts.[33] Binding of the Rnt1p dsRBD to the conserved tetraloop fold is required for correct substrate cleavage,[25] although cleavage independently from the presence of the tetraloop can be observed *in vitro* in specific conditions.[24,26] The structure of the Rnt1p dsRBD differs from canonical dsRBDs in having an additional C-terminal helix $\alpha 3$ that has been proposed to contribute to specific recognition of Rnt1p substrates by indirectly reshaping the RNA binding surface.[33,34] Our recent structure of the dsRBD bound to an AAGU tetraloop hairpin,[35] a specific but non-canonical substrate,[8,36] showed that the dsRBD employs a single binding mode for AGAA and AAGU tetraloop hairpins, with the AAGU tetraloop adopting the same shape as the AGAA tetraloop upon binding by the dsRBD. The identification of a single binding mode for two substrates with dissimilar sequences and conformations in the free state provided further evidence for the structure-specific, rather than sequence-specific, nature of the interaction between the Rnt1p dsRBD and target RNAs. This study further showed that conforma-

tional changes in the tetraloop-binding helix $\alpha 1$ are important for allowing the dsRBD to adopt the bound conformation.[35]

The dynamic properties of biomolecules often contribute to their biological functions by enabling conformational changes necessary for binding and catalysis. Moreover, conformational flexibility can allow proteins to sample functionally important alternative conformations.[37,38] Here, we have investigated the intrinsic backbone dynamics of the Rnt1p dsRBD using NMR ^{15}N spin relaxation measurements. Further, we have examined the relationship between dsRBD dynamics and structural changes that occur upon binding to AGAA tetraloop hairpins. Slow-timescale dynamics of the dsRBD indicate that helix $\alpha 1$, which interacts with the tetraloop in the complex, undergoes conformational sampling in the free state, with particularly large dynamics at a hinge within the $\alpha 1$-$\beta 1$ loop. Upon binding to RNA, dynamics at the $\alpha 1$-$\beta 1$ hinge are partially quenched. We have determined the solution structure of the free dsRBD for the same construct previously used for the structures of Rnt1p dsRBD/RNA complexes, enabling precise comparison between free and bound states. Changes in the structure and dynamics of the dsRBD upon binding to an AGAA hairpin substrate for regions distal to the binding face reveal a network of hydrophobic residues within $\alpha 1$, the $\alpha 1$-$\beta 1$ loop, and $\alpha 3$ with specific dynamic properties that facilitate binding to specific tetraloops. Mutation of individual residues in the $\alpha 1$-$\beta 1$ hinge causes changes in dsRBD conformation and stability and results in defects in snoRNA processing *in vivo*. These results show that the intrinsic dynamics of the dsRBD contributes to the selection of specific tetraloop-hairpin substrates by Rnt1p, and that helix $\alpha 1$, the $\alpha 1$-$\beta 1$ loop, and helix $\alpha 3$ cooperatively contribute to regulation of the dynamics of the RNA-binding region of the dsRBD through interactions within an extended hydrophobic core.

3.3 Materials and Methods

NMR sample preparation The Rnt1p dsRBD (residues 366-453 of Rnt1p) and single residue mutants were expressed as a glutathione S-transferase (GST) fusion proteins containing a thrombin cleavage site using the pGEX-2T vector (GE Healthcare) in BL21 (DE3) Gold cells (Stratagene).[33] The ^{15}N-labeled and ^{13}C,^{15}N-labeled GST-dsRBD fusion proteins were expressed at 30°C and 37°C, respectively, for 16 h in M9 minimal media containing 1 g/L ^{15}N-labeled ammonium chloride and 1 g/L ^{13}C glucose. GST-dsRBD was purified using a GSTrap 4B glutathione sepharose column (GE Healthcare), followed by a HiLoad 26/60 Superdex 75 pg (S75) gel-filtration column (GE Healthcare). GST-dsRBD was cleaved with 10 units of thrombin (GE Healthcare) per mg of fusion protein for 24 h at a concentration of about 1 mg/mL in a buffer containing 20 mM Tris-HCl, pH 7.5, 150 mM NaCl, and 2.5 mM CaCl$_2$. Cleaved dsRBD was purified on an S75 gel-filtration column in NMR buffer (20 mM sodium phosphate, pH 6.5, 150 mM NaCl, and 1 mM DTT) and concentrated to about 1 mM.[35]

RNA samples were prepared by *in vitro* transcription from a synthetic dsDNA template using mutant T7 RNA polymerase (P266L)[39] and purified on a 15% denaturing polyacrylamide gel containing 8 M urea as previously described.[40] RNA samples were electroeluted, further purified on a HiTrap Q anion exchange column (GE Healthcare), exchanged into NMR buffer using an Amicon Ultra centrifugal filter, and concentrated to about 1 mM. RNAs were then refolded by heating to 95°C and slow cooling to 4°C. dsRBD/RNA complexes for NMR spectroscopy were prepared by adding RNA to protein at a 1.1:1 ratio of RNA:protein and concentrated to 0.8-1 mM.

NMR spectroscopy for structure calculations NMR spectra for structure determination were recorded on Bruker DRX 500 and 600 MHz spectrometers at 25°C. The assignments for the Rnt1p dsRBD were derived from analy-

sis of 3D CBCANH, 3D CBCA(CO)NH, 3D HCCH-TOCSY, 3D HCCH-COSY, 3D ^{13}C-NOESY-HSQC and 3D ^{15}N-NOESY-HSQC experiments[41-43] acquired on ^{13}C,^{15}N-labeled dsRBD. One-bond ^{1}H-^{15}N RDCs were measured from HSQC-IPAP experiments[44] in the presence and absence of the RDC alignment medium $C_{12}E_5$/Hexanol[45] on the 600 MHz spectrometer. A total of 84 RDCs were obtained for the free dsRBD. For structure determination of the free dsRBD, a total of 2068 experimental distance restraints were obtained from NOE intensities and classified as strong (1.8-3.0 Å), medium (1.8-4.5 Å) and weak (1.8-6.0 Å). 138 dihedral angles were derived from TALOS.[46] Structures were calculated using the NIH-Xplor package[47] following standard protocols. Briefly, the calculation started from the extended protein in random orientations. The protein was then folded during 40,000 steps of high temperature dynamics with a time step of 0.002 fs. The structures were cooled down using 75 ps of slow cooling from 2000 K to 100 K. The final structures were obtained after refinement with 52 RDCs (only RDCs from secondary structure elements were used for structure calculations) during a second slow cooling from 1200 K to 100 K. The axial (-30 Hz) and rhombic (0.52) components of the alignment tensor were derived from a grid-search procedure.[48] The force constant for the RDCs was gradually increased from 0.001 to 0.2 kcal $\cdot$ mol^{-1} $\cdot$ Hz^{-2}. The twenty lowest energy structures were selected, and the structures were analyzed using MOLMOL[49] and PyMOL.[50]

NMR spectroscopy for spin relaxation experiments R_1, R_2, and ^{1}H-^{15}N nuclear Overhauser enhancement (NOE) values were measured for the free dsRBD and the dsRBD/AGAA and dsRBD/AGAA22 complexes at 20°C on a Bruker DRX 600 MHz spectrometer. R_1 experiments used the following time delays: for the free dsRBD, 41, 161, 299, 299, 437, and 644 ms; for the dsRBD/RNA complexes, 46, 207, 207, 575, 575, and 989 ms. R_2 rates were determined with Carr-Purcell-Meiboom-Gill experiments, with the following time delays: for the

free dsRBD, 11.2, 22.4, 22.4, 44.8, 67.2, 67.2, and 89.6 ms; for the dsRBD/RNA complexes, 11.2, 22.4, 22.4, 33.5, 33.5, and 44.8 ms. Spectra were processed using NMRPipe/NMRDraw, and peak intensities were obtained using NMRView. Relaxation rates were determined by fitting the expression for relaxation decay, $I(R) = I_0 e^{-Rt}$, to the peak intensities using in-house software.

Model-free analysis of relaxation data Initial estimates of the rotational correlation time and the diffusion tensor for the free $dsRBD_{366-453}$ (2LUQ; reported here) and RDC-refined dsRBD-AGAA complex (PDB ID 2LUP) were obtained using the program HYDRONMR[51,52] and were subsequently optimized using the program ModelFree 4.20[53] prior to model selection. Relaxation parameters were interpreted using the Lipari-Szabo model-free formalism to obtain values for motional parameters describing the dynamic behavior of backbone amide bond vectors.[54,55] ModelFree[53] was used to fit relaxation data for each residue to one of five increasingly complex models using optimized initial estimates of the diffusion tensor and correlation time, where model 1 includes the parameter S_s^2; model 2, S_s^2 and τ_e; model 3, S_s^2 and R_{ex}; model 4, S_s^2, τ_e, and R_{ex}; and model 5, S_s^2, S_f^2, and τ_e. Following model selection for all residues, global and internal parameters were optimized with a grid-search algorithm using an axially symmetric diffusion tensor (Tables 3.1 and 3.2). For model-free analysis, bond lengths of 1.02 Å and CSA values of -160 p.p.m. were used. Using a bond length of 1.04 Å results in small changes in the values of model-free parameters ($<5\%$) but does not change the outcome of our analysis. To confirm that the R_{ex} terms that we observe reflect backbone chemical exchange rather than diffusion anisotropy, we checked that the most significant N-H bond vectors for the free dsRBD are not aligned with the long axis of the diffusion tensor by calculating the angle between the N-H bond and the diffusion tensor z-axis, as defined by the fitted diffusion tensor obtained after model-free analysis.

In vivo **analysis of RNT1 hinge mutants**   All strains were derived from the BMA64 background. The rnt1::TRP deletion mutant and RNT1 K371A dsRBD mutant were described previously[9,56]. The dsRBD hinge mutants (I378A, G379A, G379P) and the catalytic mutant (E320K) were constructed using the delitto perfetto method.[57] A strain carrying the CORE KanR-URA3 cassette at position S376 was transformed with double-stranded DNA oligonucleotides to excise the CORE sequence and introduce the appropriate mutation in the hinge (I378A, G379A, or G379P), while the E320K mutant was produced from a strain with the CORE KanR-URA3 insertion at position E320. Genomic DNA sequences were confirmed by sequencing. Strains were grown in YPD and RNA was harvested and analyzed by Northern blot as described[9] with the following modifications: 10 μg of RNA was denatured with glyoxal, run on 1X BPTE 2% agarose gels as described[58] and transferred to Hybond-N+ membranes (GE Healthcare).

Accession numbers   Coordinates for the 20 lowest energy structures of the Rnt1p dsRBD$_{366-453}$ have been deposited in the Protein Data Bank under accession code 2LUQ, and chemical shifts have been deposited in the Biological Magnetic Resonance Data Bank under accession code 18535.

3.4   Results

Solution structure of the Rnt1p dsRBD$_{366-453}$ Three structures of the free Rnt1p dsRBD have been reported: a solution structure (PDB ID 1T4N; residues 364-450) and two crystal structures from one asymmetric unit (PDB ID 1T4O; construct includes residues 364-471; crystal structure chain A, residues 362-443; and crystal structure chain B, residues 361-448).[34] Helix α3 has a different length and orientation in each of these structures, and this heterogeneity was inferred to reflect dynamics for this helix in solution. Helix α3, unique to the Rnt1p

dsRBD, was proposed to contribute to specific RNA binding by reshaping the RNA-binding surface of the dsRBD through steric effects on helix $\alpha1$ and the $\alpha1$-$\beta1$ loop. However, in the crystal structures, helix $\alpha3$ of chain A terminates at residue 443 due to disorder in the crystal, and the position of helix $\alpha3$ of chain B is affected by crystal packing. In the solution structure, there are three non-native residues beyond 447 in helix $\alpha3$. We previously acquired residual dipolar couplings (RDCs) for the free dsRBD to determine which of the reported structures most closely reflects the conformation of the dsRBD in solution. We showed that the measured RDCs for the free dsRBD correlate best to the back-calculated RDCs for chain A of the crystal structure, although its helix $\alpha3$ is shorter than in the other reported structures of the free and bound dsRBD.[35] However, the large difference between the measured and back-calculated RDCs for helix $\alpha3$ in the free dsRBD suggested that none of the structures of the free protein accurately describe the orientation of helix $\alpha3$ in solution (Fig. 3.10).

In order to be able to completely describe the structural changes in the Rnt1p dsRBD upon RNA substrate binding, we determined the solution structure of the free dsRBD (residues 366-453), including an extensive set of RDCs (Fig. 3.1A, B). This is the same construct used for the solution structures of the dsRBD/RNA hairpin complexes.[33,35] The structures of the dsRBD are well converged, with a backbone RMSD to the mean of 0.56 ± 0.11 (Fig. 3.1A and Table 3.1). Comparison of our solution structure with the previously determined structures of Rnt1p dsRBD shows that the positions of the three β-strands and helix $\alpha2$, which comprise a hydrophobic core common to all dsRBDs, are nearly identical (RMSD < 1.3 Å; RMSD for the $\alpha2$ and the β sheets between crystal structures is $\sim$0.8 Å, between the NMR structure is $\sim$1.2 Å) (Fig. 3.1C). The $\beta1$-$\beta2$ loop shows evidence of flexibility in all of the reported structures, based on high B factors in the crystal structures and a larger range of conformations in the solution ensembles, especially for the previously determined solution structure.[34] This is consistent

with our characterization of the dynamics discussed below. However, there are significant differences in the orientations of helix $\alpha1$, helix $\alpha3$, and the $\alpha1$-$\beta1$ loop (Fig. 3.1D, E), particularly between the two solution structures. In our solution structure of the dsRBD$_{366-453}$, residue I448 is part of helix $\alpha3$, which is the non-native Ala in the previously determined solution structure. Interestingly, as shown below, I448 has one of the largest chemical shift changes upon binding to RNA substrate (see Fig. 3.6). The overall fold of the $\alpha1$-$\beta1$ loop is the same for our solution structure and the two crystal structures, although the position of the loop is different (Fig. 3.1E). Detailed analysis of our solution structure of Rnt1p dsRBD reveals interactions among residues from helices $\alpha1$ and $\alpha3$ and the $\alpha1$-$\beta1$ loop that constitute an extended hydrophobic core not present in other dsRBDs. In canonical dsRBDs, residues in helix $\alpha1$ and the $\alpha1$-$\beta1$ loop are typically solvent exposed. While contiguous with the hydrophobic core common to all dsRBDs, formed by contacts among helix $\alpha2$ and the β-sheets, this extended hydrophobic core constitutes a distinct internal network of hydrophobic interactions, indicating a potential functional role in tetraloop-specific recognition by the Rnt1p dsRBD.

Structural comparison of free and RNA-bound Rnt1p dsRBD reveals concerted changes in the extended hydrophobic core Comparison of the solution structure of the free dsRBD$_{366-453}$ with the dsRBD in complex with AGAA (Fig. 3.2) and AAGU tetraloop hairpins confirms the previously described conformational changes in the dsRBD at the RNA-binding interface that were based on comparison to crystal structure chain A[33,35] and provides additional details. Upon binding to the tetraloop minor groove, helix $\alpha1$ is extended three residues at its N-terminus, rotates 18°, bends between residues L374 and S376, and translates toward the RNA. This reorientation of helix $\alpha1$ is required for shape-specific binding to the tetraloop minor groove, which is different from the minor
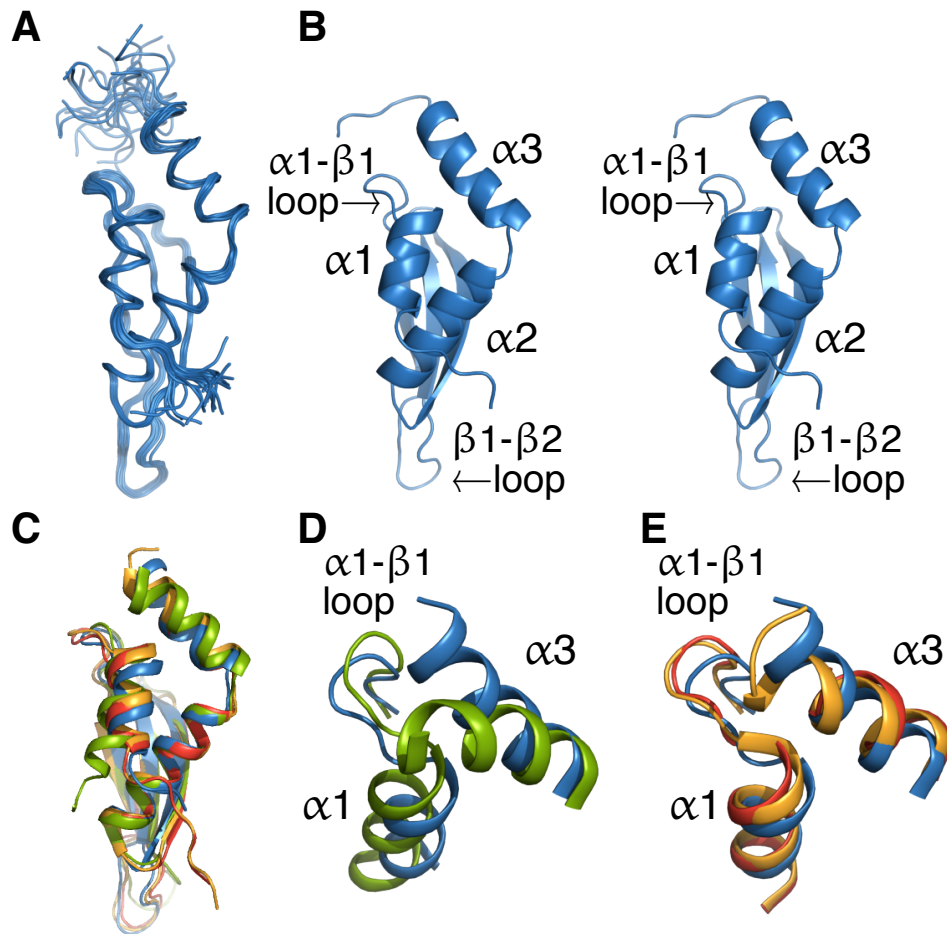
Fig. 3.1. Solution structure of the Rnt1p dsRBD$_{366-453}$ (A) Superposition of the 20 lowest energy structures of the free dsRBD. (B) Stereoview of the lowest energy structure of the free dsRBD. (C) Comparison of the dsRBD determined here (blue) with previously determined solution (1T4N; residues 364-447) (green) and crystal (IT4O; residues 362-471) chain A (red) and chain B (orange) structures. (D and E) Comparison of helix $\alpha1$, the $\alpha1$-$\beta1$ loop, and helix $\alpha3$ in (D) the solution structures of the dsRBD$_{366-453}$ and dsRBD$_{364-450}$ (IT4N) and (E) the solution structure of the dsRBD$_{366-453}$ and the crystal structures chain A and chain B. In all structures, helix $\alpha1$ begins at residue 369. Helix $\alpha3$ has three non-native residues beyond residue 447 in the solution structure IT4N. Helix $\alpha3$ ends at 443 in the crystal structure (IT4O) chain A, at 448 in the crystal structure (IT40) chain B, and at 448 in our solution structure. Structures in C-E are aligned on $\alpha2$, $\beta1$, $\beta2$, and $\beta3$.

Fig. 3.2. Comparison of the free RDC-refined dsRBD (this work) with the RDC-refined dsRBD/AGAA complex (PDB 2LUP). (A) Comparison of free and RNA bound dsRBD, with side chains of residues that interact with the RNA shown. (B) Overlay of free and RNA-bound dsRBD structures, aligned on $\alpha2$, $\beta1$, $\beta2$, and $\beta3$.
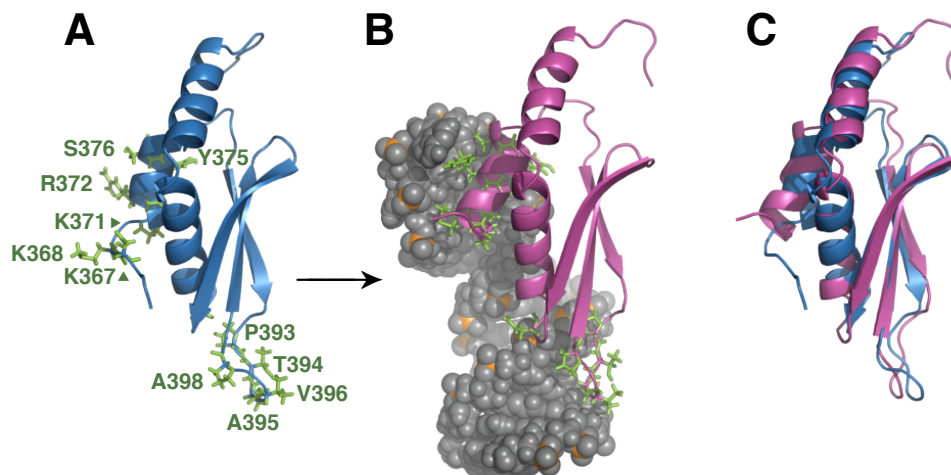
groove of A-form RNA. The $\beta1$-$\beta2$ loop, which interacts with the stem minor groove one helical turn away, moves toward the RNA by about 6 Å compared to its position in the free dsRBD. In the intervening major groove, helix $\alpha2$ and the $\beta3$-$\alpha2$ loop shift positions for side chain interactions with the phosphodiester backbone. The side chains of the interacting residues all change positions.

In addition to these conformational changes for residues at the RNA-binding interface, the solution structure of Rnt1p dsRBD$_{366-453}$ reveals specific changes in the positions of some residues at the interface between helix $\alpha1$ and helix $\alpha3$, which are distal from the protein/RNA interface. Superposition of the free and RNA-bound dsRBD on the core $\alpha2$, $\beta1$, $\beta2$, and $\beta3$ elements reveals that helix $\alpha1$, helix $\alpha3$, and the $\alpha1$-$\beta1$ loop all change positions significantly between the free and bound states (Fig. 3.3A). However, when the free and bound dsRBD are aligned on $\alpha1$ and $\alpha3$ it becomes clear that these changes are concerted, i.e., the backbones of all three of these elements are nearly superimposed indicating that they all translate in space together (Fig. 3.3B). The concerted movement

50
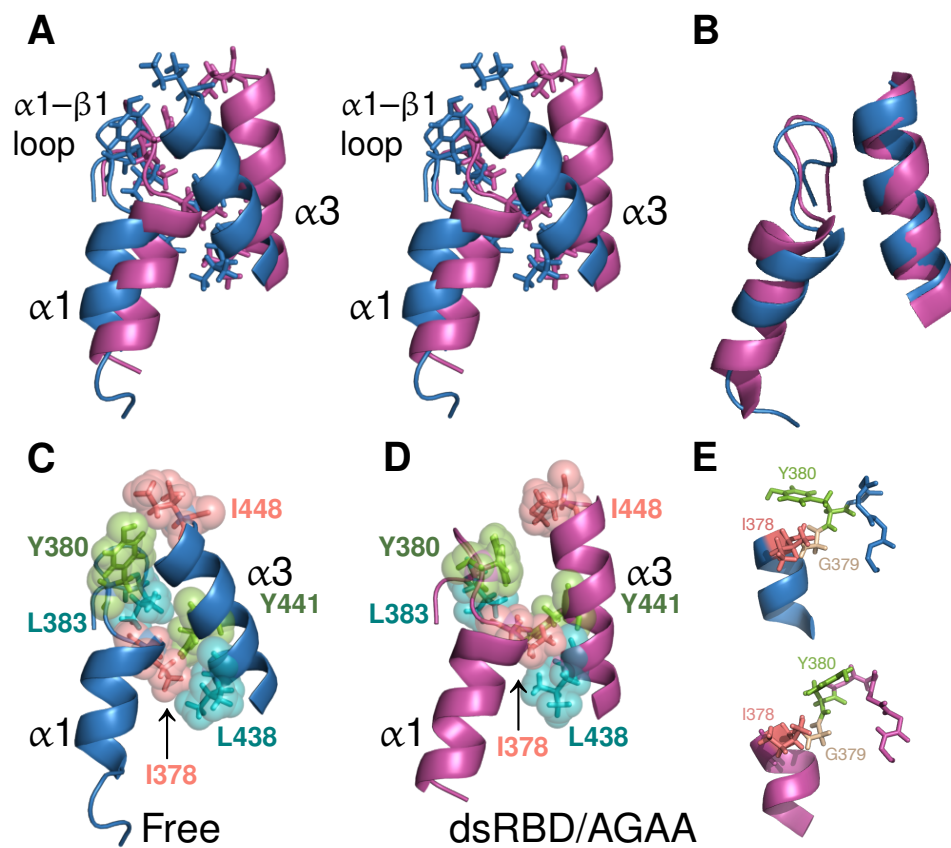
Fig. 3.3 The α1-α3 extended hydrophobic interface. (A) The hydrophobic interface between helix α1 and α3 in the free dsRBD (blue) and dsRBD/AGAA complex (magenta). Side chains are shown for hydrophobic residues contributing to the interface. The structures are aligned on α2, β1, β2, and β3 (not shown). Space-filling model of the hydrophobic core in the (B) free dsRBD and (C) dsRBD/AGAA complex. (D) The dsRBD and dsRBD/AGAA complex aligned on α1 and α3, illustrating the similar relative orientation of the helices in free and bound states. (E) The dynamic hinge in the α1-β1 loop, comprising residues 378-380, for free (top) and bound (bottom) dsRBDs.

51

of helix $\alpha1$ and helix $\alpha3$ upon RNA binding includes some reorientation of side chains in the hydrophobic core (Fig. 3.3C–E). The I378 side chain is in the *trans* rotamer conformation in the free dsRBD, but the *gauche−* conformation in the RNA-bound state (Fig. 3.3C, D). This side chain rotation may be necessary to maintain close hydrophobic contacts between $\alpha1$ and $\alpha3$ in the complex. The Y380 ring rotates to a position perpendicular to its position in the free state (Fig. 3.3E). The backbone of the $\alpha1$-$\beta1$ loop moves from its position in the free dsRBD by about 4 Å to accommodate the changes in position of $\alpha1$ and the $\alpha1$-$\beta1$ side-chains in the bound dsRBD. These changes in side-chain conformation allow the extended hydrophobic core to maintain most of the hydrophobic contacts in the bound state.

Backbone dynamics of the free dsRBD To investigate whether the concerted conformational changes in the extended hydrophobic core contribute to tetraloop-specific recognition and, more generally, how conformational flexibility within the free dsRBD affects substrate specificity and binding, we investigated the backbone dynamics of free and RNA bound dsRBDs using NMR spin-relaxation experiments (Fig. 3.4). The measured ^{15}N relaxation data, R_1, R_2, and ^{1}H-^{15}N heteronuclear nuclear Overhauser enhancement (NOE) were analyzed using the Lipari-Szabo model-free formalism to obtain a quantitative description of the backbone dynamics, where the order parameter (S^2) and the internal correlation time (τ_e) describe the amplitude and timescale of backbone dynamics, respectively. In addition, to fully describe internal motions, model-free analysis also includes a term to account for chemical exchange at the μs-ms timescale (R_{ex}). Overall, the S^2 values obtained from model-free analysis indicate that the dsRBD is relatively rigid for all structured residues at the ps-ns timescale, with an average S^2 value of 0.86 (Fig. 3.5A). The single exception is residue N399, which has an S^2 value of 0.6, and is adjacent to a proline (P398) in the $\beta1$-$\beta2$ loop. We were unable to

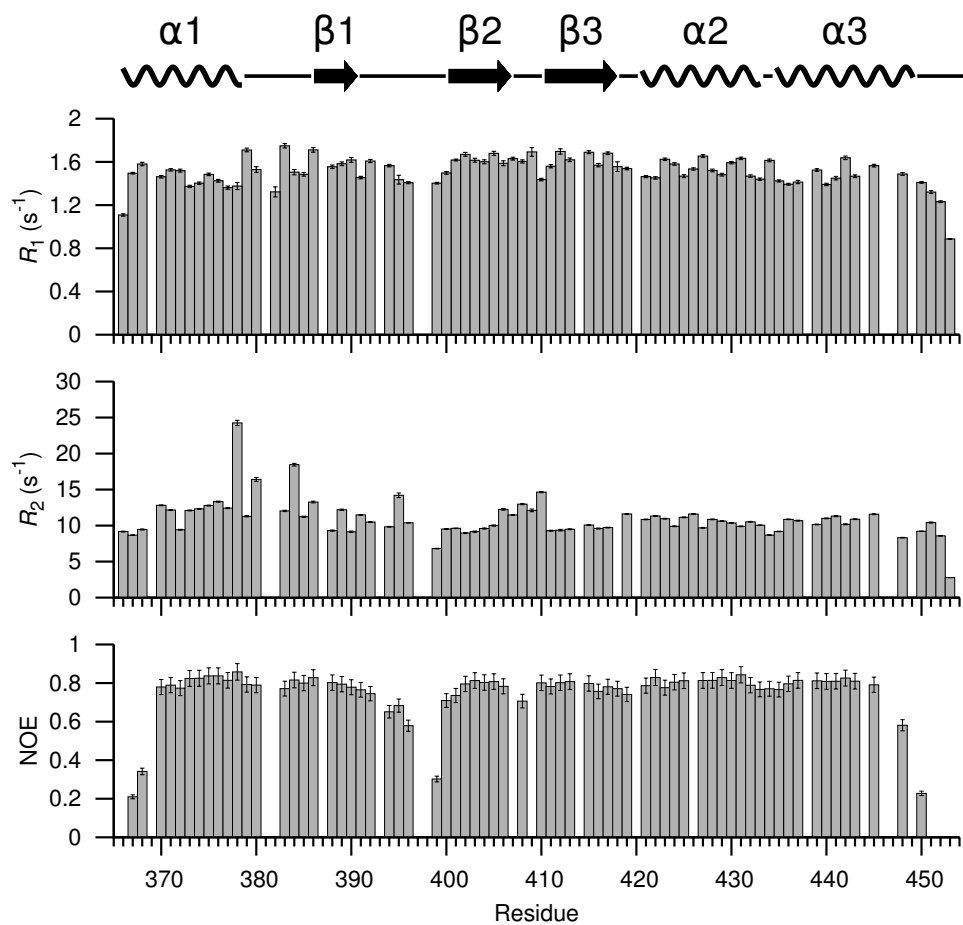**Fig. 3.4.** [15]N relaxation parameters for the free dsRBD at 150 mM NaCl and 20°C. Error bars reflect the fitting error for R_1 and R_2 values and the estimated error in the measurement for NOE values based on the noise in the spectrum.

determine relaxation parameters for residue D397 on the other side of the proline due to spectral overlap. The conformational flexibility in the $\beta 1$-$\beta 2$ loop, as evidenced by the low S^2 value of N399, is consistent with the multiple conformations for the $\beta 1$-$\beta 2$ loop in the NMR structure ensembles and high B-factors in the crystal structures of the free dsRBD.[34]

Slow-timescale motions, as reflected by the inclusion of an R_{ex} term during model-free analysis, are present in some residues in helix $\alpha 1$, the $\alpha 1$-$\beta 1$ loop, strand $\beta 1$, the $\beta 1$-$\beta 2$ loop, the $\beta 2$-$\beta 3$ loop, and residues Y441 and R445 in helix $\alpha 3$ (Fig. 3.5A, B). The R_{ex} values in the $\beta 1$-$\beta 2$ loop and the end of $\beta 1$ are consistent with the observed flexibility in this region and proposed P393 *cis-trans* isomerization[34]. Within the extended hydrophobic core, a cluster of residues in helix $\alpha 1$ and the $\alpha 1$-$\beta 1$ loop exhibit notable R_{ex}. One of these residues, I378, has an unusually large value for μs-ms timescale exchange, with an R_{ex} value of 15 s^{-1}. I378 is the C-terminal residue in helix $\alpha 1$ and its hydrophobic side chain is part of the extended hydrophobic core. This large R_{ex} could be due to I378 undergoing jumps between the *trans* and *gauche*$-$ rotamers.[59] Residue R384, which is in the $\alpha 1$-$\beta 1$ loop, also has a high R_{ex} value ($\sim$8 s^{-1}) (Fig. 3.5A, B). Based on the conformational changes in residues within the $\alpha 1$-$\beta 1$ loop (Fig. 3.3E) and the large slow-timescale dynamics for residues 378-380 (Fig. 3.5A), we identify these residues as a dynamic hinge that we propose allows conformational sampling by helix $\alpha 1$. Since I378 is in the *trans* and *gauche*$-$ conformations in the free dsRBD and RNA-bound dsRBD, respectively, this would suggest that the hinge samples the bound conformation. The $\beta 2$-$\beta 3$ loop has low B-factors in the crystal structure and is well defined in the solution structures, but there is R_{ex} for some residues. Examination of the structure of the free dsRBD reveals that the residues in the $\beta 2$-$\beta 3$ loop that exhibit R_{ex} interact with residues in helix $\alpha 3$ and the $\alpha 1$-$\beta 1$ loop and would be sensitive to conformational changes in the extended hydrophobic core. The presence of a dynamic hinge and chemical exchange in the

extended hydrophobic core imply that the tetraloop-binding helix $\alpha1$ samples the bound state in the free dsRBD.

Dynamics of the dsRBD in the dsRBD/AGAA complex To determine whether specific RNA substrate binding changes the μs-ms dynamics observed in the free dsRBD, we collected R_1, R_2 and heteronuclear NOE values for the dsRBD/AGAA hairpin complex whose structure was previously reported[33] (Fig. 3.11). The AGAA hairpin, consisting of a 14-bp dsRNA stem capped by an AGAA tetraloop, is a model substrate derived from the Rnt1p recognition motif in the Rnt1p pre-snoRNA substrate snR47. This RNA provides a minimal binding site for the dsRBD, with only 2-3 bp extending below the interaction of the $\beta1$-$\beta2$ loop in the minor groove. The average R_1 and R_2 values on the dsRBD/AGAA hairpin complex are lower and higher, respectively, than those of the free protein, as would be expected for the increased molecular weight of the complex. Heteronuclear NOE values indicate that the dsRBD in the complex is rigid overall, except for the N- and C-termini and the $\beta1$-$\beta2$ loop. Several residues in the $\beta1$-$\beta2$ loop have heteronuclear NOE values between 0.4 and 0.6, indicating that this loop remains flexible in the dsRBD/AGAA hairpin complex.

Binding of the dsRBD to the AGAA hairpin results in an overall increase in the S^2 values of most of the protein residues (average increase of 0.15) (Fig. 3.5A, C). Exceptions are small decreases (<0.1) for helix $\alpha1$ residues K371 and S376, which interact with the minor groove of the AGAA tetraloop, Y380 and L383 in the extended hydrophobic core in the $\alpha1$-$\beta1$ loop, and the single residue R433 between $\alpha2$ and $\alpha3$ (Fig. 3.5C). R_{ex} values increase for most of the residues in helix $\alpha1$, with particularly large increases for K371 and S376, which contact the RNA backbone. Helix $\alpha3$, which has only two residues with R_{ex} in the free dsRBD, also shows R_{ex} for most residues. In contrast, the dynamic hinge residues I378 and Y380, both of which exhibit slow-timescale motions in the free protein, have lower
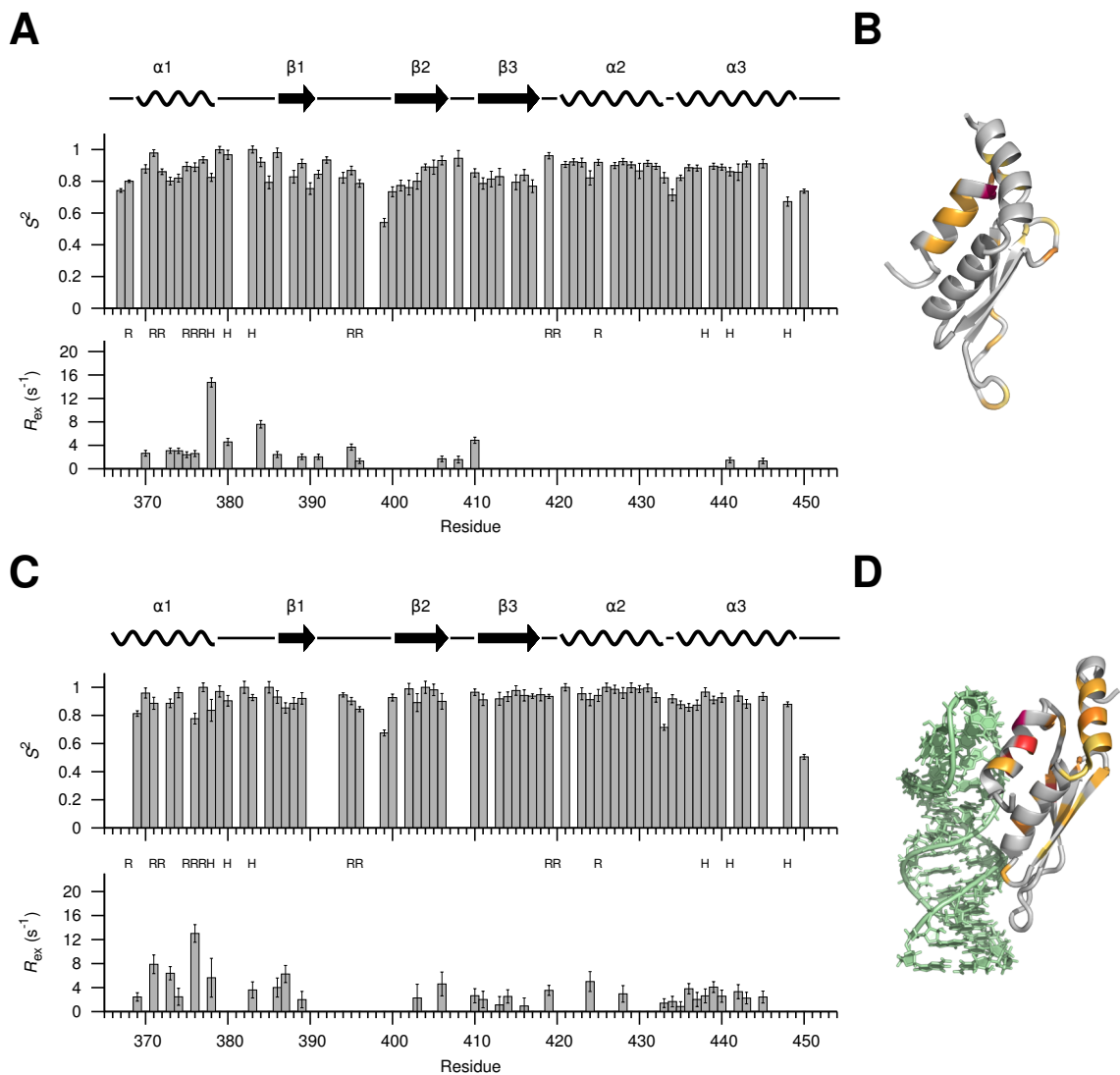
Fig. 3.5. Fast- and slow-timescale dynamics of the free dsRBD and the dsRBD/AGAA complex at 150 mM NaCl. (A) S_2 and R_{ex} model-free parameters for the free dsRBD. (B) Structure of free dsRBD with residues that show R_{ex} highlighted. (C) S_2 and R_{ex} model-free parameters for the dsRBD/AGAA complex. (D) Structure of dsRBD in the dsRBD/AGAA complex with residues that show R_{ex} highlighted. Residues labeled "R" contact the RNA, and residues labeled "H" are part of the extended hydrophobic core.

R_{ex} values in the complex. Dynamics in helix $\alpha 1$ likely reflect flexibility at the protein-RNA interface. For helix $\alpha 3$, the uniform increase in R_{ex} could originate from propagation of the dynamics in helix $\alpha 1$ via the extended hydrophobic core, and/or from an increase in entropy of the dsRBD in the bound state, an effect that has been observed in other RNA-binding proteins.[60] A395 and V396, near P398 in the $\beta 1$-$\beta 2$ loop, which contact the minor groove of the dsRNA stem, also have lower R_{ex} values in the complex (Fig. 3.5C, D). The decrease in slow-timescale motions for residues in the dynamic hinge and the $\beta 1$-$\beta 2$ loop indicates that some slow-timescale dynamics present in the free dsRBD are quenched upon binding to RNA.

Helix $\alpha 1$ residue S376 has no R_{ex} term in the free dsRBD but has the largest R_{ex} value in the dsRBD/AGAA complex. Helix $\alpha 1$ bends at S376 to insert into the minor groove, and the S376 side-chain contacts the RNA backbone on the 3$'$ side of the AGAA tetraloop. This correlation between changes in structure and dynamics suggests that the dynamic properties of S376 might have a functional role in allowing the dsRBD to adopt the bound conformation. Alternatively, chemical exchange at S376 might be caused by exchange between the specifically and nonspecifically bound states, reflecting the role of this residue in recognizing the backbone of the tetraloop.

To verify that the observed R_{ex} is attributable only to the intrinsic dynamics of the dsRBD and not to nonspecific protein-protein interactions or to exchange between the free and bound state,[61] we measured R_2 values at concentrations of 1 mM and 0.5 mM for the dsRBD/AGAA complex and the free dsRBD (Fig. 3.12). In the absence of these possible additional contributions to chemical exchange, R_2 values and NMR linewidths would be expected to be the same at both concentrations. In both cases, R_2 values and NMR linewidths for two protein concentrations are nearly identical, indicating that the dynamics determined by model-free analysis arise only from the intrinsic dynamics of the dsRBD and not

from other possible contributions to chemical exchange.

In summary, two distinct changes in dsRBD dynamics in the extended hydrophobic core are observed upon substrate binding. First, there is a general increase in slow-timescale dynamics for residues in helices $\alpha 1$ and $\alpha 3$ that is associated with concerted changes in the extended hydrophobic core. Second, there is a decrease in slow-timescale dynamics for residues in the $\alpha 1$-$\beta 1$ hinge and the $\beta 2$-$\beta 3$ loop, due to locking in of helix $\alpha 1$ by shape-specific binding to the tetraloop minor groove.

Ionic strength dependence of dynamics for the dsRBD in the dsRBD/ AGAA complex Previous NMR titration and isothermal titration calorimetry (ITC) experiments revealed that the dsRBD can bind to the AGAA hairpin both specifically and nonspecifically at 150 mM NaCl, with saturation of the RNA at a protein:RNA ratio of 2:1.[35] The relaxation data discussed above for the dsRBD/AGAA complex were measured at a protein:RNA ratio of 1:1.1 and were expected to primarily reflect values for the dsRBD bound to the specific site. To further confirm this, we investigated the binding and dynamics of the dsRBD/AGAA hairpin complex at 300 mM NaCl (Fig. 3.13). At this salt concentration, nonspecific binding should be minimal. Chemical shift mapping for the dsRBD upon RNA binding at 300 mM NaCl revealed chemical shift changes similar in pattern to those for the complex at 150 mM NaCl, but with a much smaller magnitude (Fig. 3.6). This is consistent with the lower binding affinity of the dsRBD for RNA at a higher salt concentration, as measured by NMR titration and ITC.[35] At 300 mM NaCl, the dsRBD exhibits R_{ex} values similar overall to those observed at 150 mM NaCl (compare Fig. 3.7A, B with Fig. 3.5C, D). This observation is consistent with a single, specific binding site on the AGAA hairpin. Hence, the dsRBD is fully bound to the AGAA hairpin at the specific binding site under the conditions used for spin relaxation experiments at a high concentration
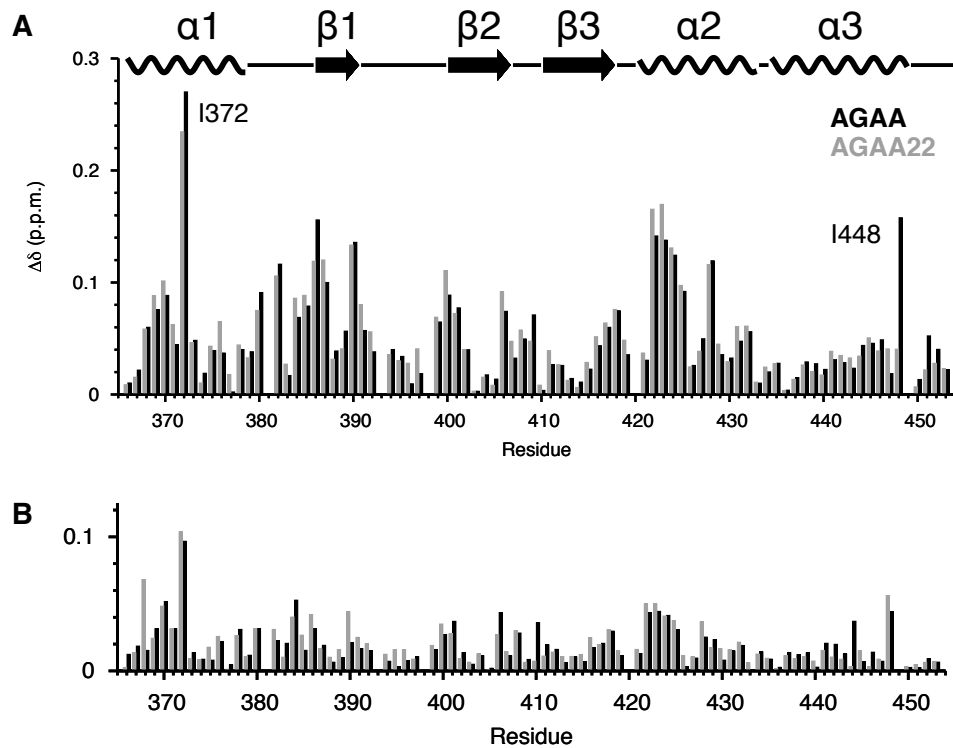
Fig. 3.6. The effect of substrate length and salt concentration on chemical shift. Chemical shift mapping of the dsRBD at (A) 150 mM and (B) 300 mM NaCl bound to a tetraloop hairpin RNA with a 14-bp stem (AGAA) (black) and a tetraloop hairpin RNA with a 22-bp stem (AGAA22) (gray).
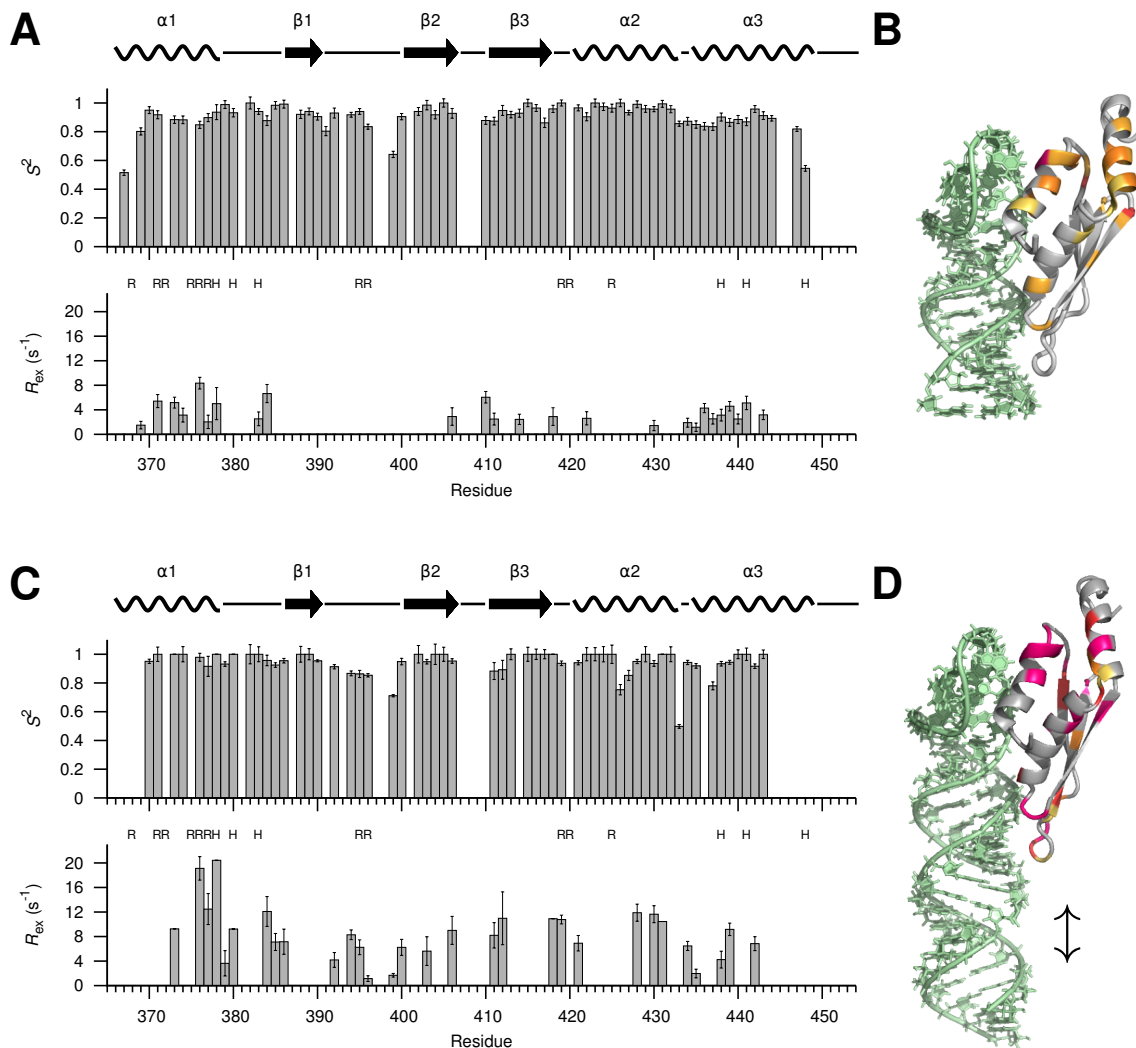
Fig. 3.5. Fast- and slow-timescale dynamics of the dsRBD/AGAA and the dsRBD/AGAA22 complexes at 300 mM NaCl. (A) S_2 and R_{ex} model-free parameters for the dsRBD/AGAA complex. (B) Structure of dsRBD/AGAA complex with residues that show R_{ex} highlighted. (C) S_2 and R_{ex} model-free parameters for the dsRBD/AGAA22 complex. (D) Structure of dsRBD in the dsRBD/AGAA22 complex with residues that show R_{ex} highlighted. Residues labeled "R" contact the RNA, and residues labeled "H" are part of the extended hydrophobic core.

of the complex and 150 mM or 300 mM NaCl.

Dynamics of the dsRBD in the presence of both specific and nonspecific binding sites   As discussed above, the dsRNA construct was designed such that it has a minimal binding site for the dsRBD. To investigate whether there is a difference in dsRBD dynamics when both nonspecific and specific binding sites are present we collected NMR spin relaxation data for Rnt1p dsRBD in complex with an AGAA tetraloop hairpin with a 22-bp stem (AGAA22) at 300 mM NaCl (Fig. 3.14). AGAA22 has a stem that is eight base pairs longer than the AGAA hairpin (14 bp), allowing for nonspecific binding to the longer dsRNA stem in addition to specific binding site at the AGAA tetraloop. Because of the longer stem, Rnt1p dsRBD can potentially exchange between the specific site and nonspecific sites on AGAA22. AGAA22 more closely reflects native conditions for substrate binding by Rnt1p dsRBD, as the stem length is the same as the stem in the pre-snR47 snoRNA (excluding a single bulge). In general, the values for chemical exchange, as described by R_{ex}, are significantly larger for dsRBD/AGAA22 than for dsRBD/AGAA. Slow-timescale dynamics for dsRBD/AGAA22 are present for residues in helices $\alpha1$ and $\alpha3$ in or near the extended hydrophobic core, residues throughout the RNA-binding interface, including helix $\alpha2$ and the $\beta1$-$\beta2$ loop, and in $\beta2$ and $\beta3$. In dsRBD/AGAA, there was no R_{ex} for any residues in the $\beta1$-$\beta2$ loop, while in dsRBD/AGAA22 most of the $\beta1$-$\beta2$ loop residues show R_{ex} (Fig. 3.7C, D). The R_{ex} in the $\beta1$-$\beta2$ loop is both larger and present in more residues than in the free dsRBD (Fig. 3.5A). Under the experimental conditions of 300 mM NaCl and excess RNA, the dsRBD is relatively selective for specific binding, so the additional contribution to R_{ex} arising from the presence of additional nonspecific binding sites can be attributed to exchange between tetraloop (specific) and stem (nonspecific) binding sites. It is notable that all of the elements of the dsRBD that interact with the minor and major groove of the dsRNA stem show more

conformational exchange than when only a specific binding site is available. The additional protein dynamics for the dsRBD/AGAA22 complex, compared to the dsRBD/AGAA complex, also reveal the significance of conformational changes in the extended hydrophobic core, in addition to residues at the RNA binding interface, in binding site selection. We conclude that the difference in R_{ex} for the complex with AGAA22 *versus* AGAA reflects some nonspecific binding to the dsRNA on the longer substrate. Furthermore, once helix $\alpha 1$ locks in to the tetraloop, the rest of the dsRBD locks into place, resulting in a decrease of R_{ex} in the $\beta 1$-$\beta 2$ loop for AGAA *versus* AGAA22.

Hydrophobic interactions with the $\alpha 1$-$\beta 1$ loop maintain dsRBD stability
To extend insights from our characterization of dsRBD structure and dynamics, we further investigated the importance of residues in the $\alpha 1$-$\beta 1$ loop for RNA binding by generating four dsRBD mutants with single mutations in the $\alpha 1$-$\beta 1$ loop: I378A, G379P, G379A, and Y380A. These three residues are part of the $\alpha 1$-$\beta 1$ hinge in the extended hydrophobic core. The side chains of I378 and Y380 change position between the free and RNA-bound states and maintain hydrophobic contacts with residues in helix $\alpha 3$. The ϕ and ψ angles for G379 also change between free and bound states, due to conformational changes in the hydrophobic core (Fig. 3.3C–E). The ^{1}H-^{15}N HSQC spectrum of I378A was poorly dispersed (Fig. 3.15), and the CD spectrum showed no evidence for secondary structure (Fig. 3.16), indicating that the majority of the protein is unfolded at 25°C. However, in freshly prepared protein samples, there appears to be about 10% folded protein based on the ^{1}H-^{15}N HSQC. Addition of RNA to I378A results in some chemical shift changes indicative of binding for the peaks from the folded protein, but fewer than for the wild-type dsRBD, and the protein unfolds over time. Thus, we conclude that the mutation I378A destabilizes the protein and may also lower RNA binding affinity. Since I378 interacts with residue Y441, which is in helix

$\alpha 3$ and part of the extended hydrophobic core, we tested the importance of this interaction by making a Y441A mutation. Y441A is also unstable in solution and precipitates after about 20 min at 25°C, and ^{1}H-^{15}N HSQC spectra indicate that it is unfolded prior to precipitation. We note that the mutation R445A, in helix $\alpha 3$, was previously shown to destabilize the extended hydrophobic core of the dsRBD.[33,34] This residue is close to the $\alpha 1$-$\beta 1$ loop residue S382, and shows R_{ex} in both the free and bound dsRBD.

For the G379P mutant, CD spectra indicate that the T_m decreases by $\sim$6°C and that melting is less cooperative. The ^{1}H-^{15}N HSQC (Fig. 3.15) has chemical shift changes throughout helices $\alpha 1$ and $\alpha 3$, and none of the resonances for the $\alpha 1$-$\beta 1$ loop are observed (Fig. 3.15 and 3.16). Analysis of the backbone chemical shifts for dsRBD G379P indicates that the C-terminal end of helix $\alpha 1$ and all of helix $\alpha 3$ are altered relative to the WT dsRBD (Fig. 3.17). Addition of the AGAA hairpin to G379P up to a 2:1 excess of RNA resulted in almost no changes in the ^{1}H-^{15}N HSQC spectrum, indicating that the G379P substitution essentially abrogates binding of the dsRBD to RNA. G379A had a substantially altered ^{1}H-^{15}N HSQC spectrum (Fig. 3.15) and is unstable, as the protein precipitated after 20 min at 25°C. However, in the presence of the AGAA hairpin, the G379A mutant gives ^{1}H-^{15}N HSQC spectra indicating that G379A forms a stable complex (Fig. 3.15). Lastly, we found that Y380A degrades during expression, implying that the mutation of this residue also significantly destabilizes the protein.

In summary, all of the mutations in the $\alpha 1$-$\beta 1$ loop and $\alpha 3$ destabilize the extended hydrophobic core to some extent and have variable effects on RNA binding. For the G379P mutation, changes to the extended hydrophobic core completely disrupt RNA binding, although this mutation has the smallest effect on dsRBD stability. For G379A, binding to RNA helps stabilize the folded state of the dsRBD. Because all of the residue substitutions in the extended hydrophobic core affect protein stability, we were not able to assess their effects on dynamics in-

dependently. Nevertheless, these results support a central structural role for the $\alpha 1$-$\beta 1$ loop and extended hydrophobic core in maintaining dsRBD stability.

Effect of $\alpha 1$-$\beta 1$ loop mutations on snoRNA processing *in vivo* To determine whether the mutations in the $\alpha 1$-$\beta 1$ hinge have an effect on cleavage of Rnt1p substrates *in vivo*, we introduced the single mutations I378A, G379A, and G379P into the RNT1 gene and examined by northern blot the effect of these mutations on the processing of snR36 and snR47 snoRNAs *in vivo*. For comparison, we included in the analysis strains harboring a previously studied mutation in helix $\alpha 1$ that affect processing (K371A),[33] a catalytically inactive mutant (E320K), and a RNT1 deletion (rnt1Δ). Unlike the previously studied K371A mutant, all three $\alpha 1$-$\beta 1$ loop mutants exhibit temperature-sensitive growth defects (Fig. 3.8A, B). The growth defects for strains bearing the I378A and G379A mutations are comparable and relatively modest, while the G379P strain had a growth defect comparable to the rnt1Δ strain. This is consistent with the *in vitro* results that showed that while stable, dsRBD G379P does not bind RNA.

The strain bearing the I378A mutation shows an inhibition of snoRNA processing comparable to the K371A mutation, with a slight processing defect for snR47 and a more pronounced defect for snR36 (Fig. 3.8C). snR36 was previously observed to be more sensitive than snR47 to mutations in the Rnt1p dsRBD, because of the presence of a large bulge after the fourth base pair below the tetraloop.[56] The G379A strain exhibited only minor effects on snoRNA processing *in vivo*. Although it has a growth defect comparable to I378A, the dsRBD is stabilized by binding to RNA, which may explain the difference in effect on snoRNA processing. The G379P strain, in contrast, showed severe processing defects for both substrates. The processing defects in strains bearing the I378A, G379P, and G379A mutations are consistent with NMR and CD results that indicate that these mutations introduce changes in stability and RNA-binding affinities of the

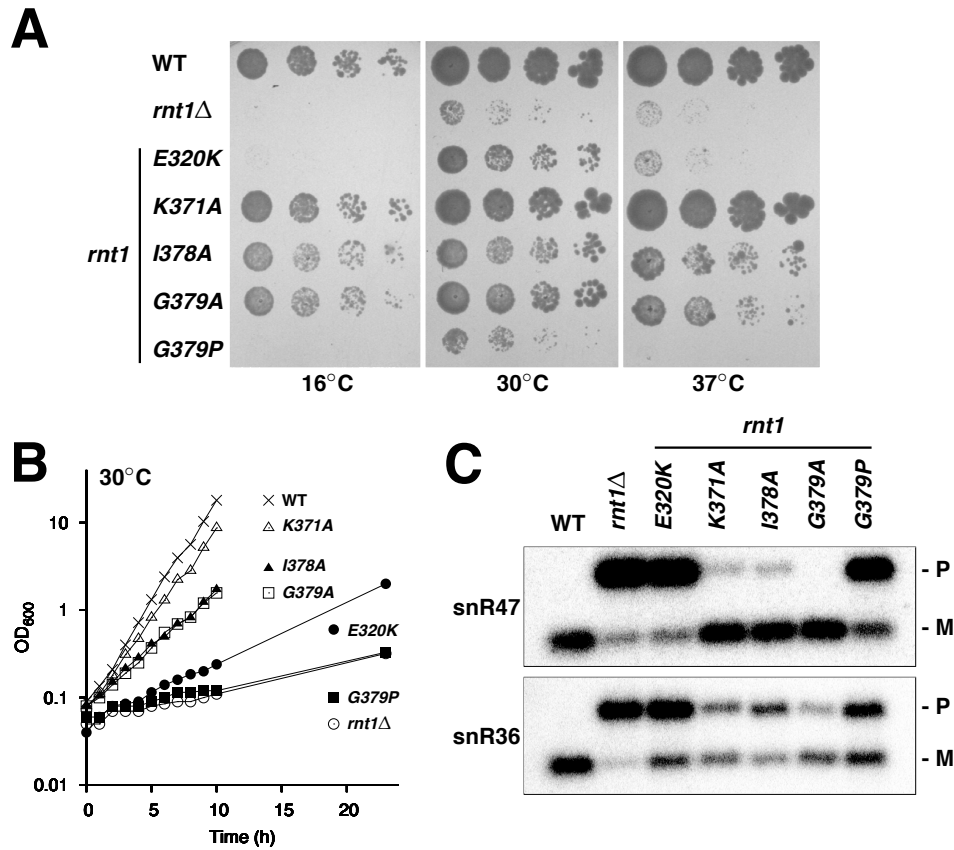**Fig. 3.8.** *In vivo* analysis of dsRBD $\alpha1$-$\beta1$ loop mutants. (A) Growth of wild-type dsRBD and dsRBD hinge mutants, with serial dilutions at 16, 30, and 37°C. (B) Growth curve for the wild-type dsRBD and dsRBD hinge mutants at 30°C. (C) Northern blot analysis of snR47 and snR46 snoRNA processing for wild-type dsRBD and dsRBD hinge mutants, showing unprocessed precursor (P) and mature snoRNAs (M).

dsRBDs. We conclude that mutations in the α1-β1 hinge, all of which destabilize the extended hydrophobic core and affect RNA binding to different extents, compromise the function of Rnt1p *in vivo*.

3.5 Discussion

dsRBDs recognize dsRNA primarily by interactions with the phosphodiester backbone of successive minor, major, and minor grooves via the β1-β2 loop, the N-terminal end of helix α2, and helix α1, respectively. The dsRBD of Rnt1p is unusual in that helix α1 recognizes a tetraloop through shape-specific recognition of its minor groove.[33] The Rnt1p dsRBD also has an additional helix α3, which packs against the α1-β1 loop to form a distinctive extended hydrophobic core. All dsRBDs have a conserved hydrophobic core, with residues contributed by the C-terminal residues of helix α1, helix α2, and strand β3. Hydrophobic interactions among these residues in the core of the protein stabilize the folded conformation of the dsRBD.[29,62] The unique hydrophobic interface between helices α1 and α3 in the Rnt1p dsRBD is contiguous with the conserved hydrophobic core. Through a detailed analysis of the structures and dynamics of the free and bound dsRBDs, we have shown that this extended hydrophobic core plays an essential role in enabling defined conformational changes associated with RNA substrate recognition. Residues in the α1-β1 loop that interact with helix α3 to form the extended hydrophobic core constitute a dynamic hinge that allows a concerted change in the positions of helix α1 and helix α3 between the free and bound states, a key feature of substrate recognition by the Rnt1p dsRBD (Fig. 3.3). The importance for RNA binding of residues in the extended hydrophobic core, which includes the α1-β1 hinge, is further supported by the results of mutagenesis of individual residues on snoRNA processing *in vivo* (Fig. 3.8).

Helix α3 has been previously proposed to contribute to specific RNA binding

indirectly by affecting the length and orientation of helix $\alpha 1$ in the free protein.[34] However, the orientation of helix $\alpha 1$ in the free dsRBD is the same as other dsRBDs that bind to dsRNA nonspecifically. Our results show that the helix $\alpha 3$ contributes to substrate-specific binding by participating in the reorientation of helix $\alpha 1$ in the bound state through concerted structural changes in the extended hydrophobic core.

The free dsRBD samples multiple conformations   Backbone dynamics of the free dsRBD obtained via model-free analysis of NMR spin relaxation data reveal extensive slow-timescale dynamics primarily localized in the RNA binding interface and extended hydrophobic core, including helix $\alpha 1$, $\alpha 1$-$\beta 1$ loop, and $\beta 1$-$\beta 2$ loop, as well as limited dynamics in helix $\alpha 3$. Our comparison of free and bound structures shows that upon binding of the RNA substrate, the $\alpha 1$-$\beta 1$ loop changes conformation to allow helix $\alpha 1$ and $\alpha 3$ to undergo concerted changes in orientation and side chain position in order for helix $\alpha 1$ to be able to bind to the minor grove of the substrate tetraloop (Fig. 3.2 and 3.3). The $\beta 1$-$\beta 2$ loop also translocates about 6 Å to bind to the minor grove of dsRNA one helical turn away from the tetraloop (Fig. 3.2). Thus, the dynamic behavior of the free dsRBD on both fast and slow timescales is associated with conformational changes within the extended hydrophobic core that accompany substrate recognition. This localized flexibility supports the notion that conformational adaptation upon substrate binding is enabled by the dynamics of the free dsRBD. Mutations of residues in the $\alpha 1$-$\beta 1$ loop affect the stability and RNA-binding properties of the dsRBD, revealing that the interactions of the $\alpha 1$-$\beta 1$ loop with helix $\alpha 3$ are essential for dsRBD stability and function.

The observed dynamics of the $\alpha 1$-$\beta 1$ loop in the free dsRBD and the concerted movement of helices $\alpha 1$ and $\alpha 3$ led us to propose that residues 378-380 in the $\alpha 1$-$\beta 1$ loop serve as a dynamic hinge enabling conformational exchange between the

free and bound states. One possible model for the contribution of the α1-β1 hinge is that hinge dynamics on the μs-ms timescale backbone facilitate conformational sampling by helix α1. Moreover, hinge dynamics would facilitate concerted movement of helices α1 and α3 upon binding because hinge residues I378 and Y380 are also part of the extended hydrophobic core. These dynamics, along with those of the β1-β2 loop, are partially quenched upon binding to the specific site on target substrates (Fig. 3.9). We cannot exclude, however, that the dsRBD experiences a combination of conformational selection and induced fit to achieve its final bound conformation.

Previous studies of the contribution of protein dynamics to RNA recognition have shown that high-affinity binding to RNA is generally associated with the presence of extensive R_{ex} throughout an RNA-binding domain. NMR relaxation studies of the two dsRBDs of protein kinase R (PKR) indicated that residues that directly interact with the RNA and throughout helix α1, sheet β1, and helix α2 have slow-timescale motions for PKR dsRBD1, which binds to dsRNA with high affinity. In contrast, there are but few such motions for PKR dsRBD2, which has weaker binding affinity for dsRNA.[63] Dynamics within the PKR dsRBD1 were proposed to allow for adaptation to non-uniform RNA substrates. The observed R_{ex} within PKR dsRBD1 and Rnt1p dsRBD are different in both the distribution and extent of slow-timescale dynamics. Thus, dsRBDs with different dsRNA substrates can have different dynamic modes despite having similar structures in the free state. Here, we have shown the first example where dynamic properties of a dsRBD are associated with defined structural changes in the protein that take place upon binding to RNA.

Substrate binding induces changes in backbone dynamics   In complex with RNA, dynamics in Rnt1p dsRBD are present throughout the extended hydrophobic core and RNA-binding interface, corresponding to binding-induced con-
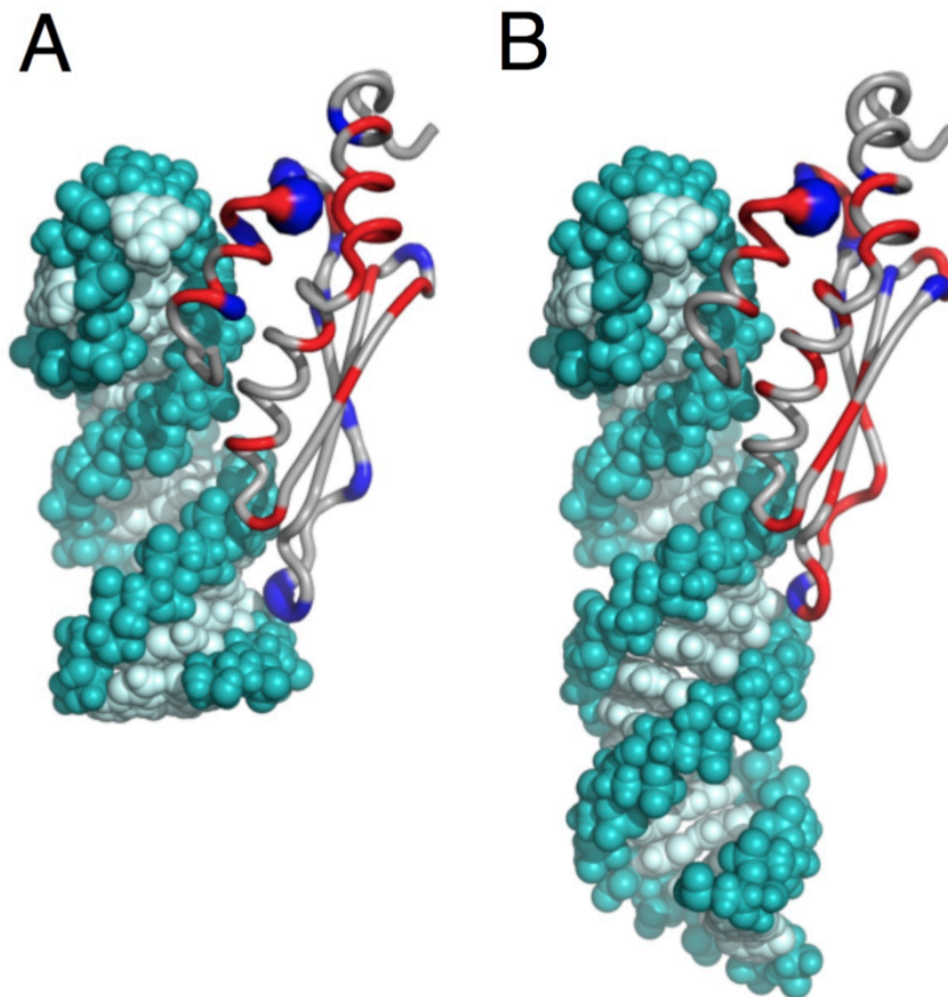
Fig. 3.9. dsRBD dynamics are associated with concerted structural changes necessary for binding. Change in R_{ex} for free *versus* RNA-bound dsRBD for (A) the dsRBD/AGAA complex and (B) the dsRBD/AGAA22 complex. The model of the dsRBD/AGAA22 complex with dsRBD bound specifically at the tetraloop is based on the structure of the dsRBD/AGAA complex. ΔR_{ex} (R_{ex} [free dsRBD] minus R_{ex} [dsRBD in complex with RNA]) is shown in red (increase in R_{ex}) and blue (decrease in R_{ex}). The relative magnitude of the change in R_{ex} is represented by the tube width.

formational changes. Changes in R_{ex} between free and AGAA tetraloop hairpin-bound dsRBDs are shown in Fig. 3.9. Residues within the $\alpha 1$-$\beta 1$ hinge that are dynamic in the free dsRBD are partly or completely quenched, while residues within helix $\alpha 1$ and $\alpha 3$ have even larger slow-timescale dynamics in the complex. Residues at the N-terminus of helix $\alpha 1$ in the complex fold only upon binding to RNA,[35] and these residues also have a decrease in slow timescale dynamic upon binding. Two residues within the $\beta 1$-$\beta 2$ loop also have lower R_{ex} in the complex than in the free dsRBD, which is consistent with the stable interaction of this loop with the stem minor groove.

An increase of the prevalence of chemical exchange upon substrate binding appears to be a common feature of nucleic acid binding proteins, as well as proteins involved in protein-protein interactions.[31,64] Typically, this increase in R_{ex} is observed to occur at sites distant from the interface with the partner molecular and implies an indirect role for conformational flexibility in binding. The increase in R_{ex} is often distributed throughout the protein and is not well correlated with specific structural changes. In contrast, for Rnt1p dsRBD the observed increase in R_{ex} for regions of the protein distal from the RNA binding surface, particularly in the C-terminus of helix $\alpha 3$, is correlated with conformational changes associated with RNA binding. The counterintuitive increase in dynamics for regions of the dsRBD distal to the RNA-binding face reveals that a broad network of residues within the dsRBD contributes to conformational adaptation to the specific tetraloop binding site. The results of these experiments highlight the importance of protein conformational flexibility, particularly within the extended hydrophobic core, in binding of the Rnt1p dsRBD to RNA tetraloop hairpin substrates.

Dynamics reflect binding site exchange on a long substrate   Because the dsRBD binds to the minimal substrate (AGAA) at 300 mM NaCl only at the

specific tetraloop site, slow-timescale dynamics are likely to be limited to intrinsic dynamics of the bound state, reflecting intrinsic conformational entropy of the dsRBD in complex with RNA. However, exchange between specific and nonspecific sites becomes significant in the dsRBD/AGA22 complex, as the longer stem allows for nonspecific binding away from the tetraloop. In the dsRBD/AGAA22 complex, chemical exchange values are quantitatively higher and are present throughout the dsRBD. Hence, dynamics within the dsRBD in the dsRBD/AGAA22 complex suggest that the dsRBD distinguishes between specific and nonspecific complexes after binding to the dsRNA substrate through conformational exchange. Increased dynamics throughout the extended hydrophobic core and RNA-binding interface, compared to the dsRBD/AGAA complex (Fig. 3.9B), suggests that flexibility within the RNA-bound dsRBD remains important for selection of the specific binding site even after the dsRBD is bound to RNA. Moreover, elevated R_{ex} values of helix α1 and β1-β2 loop would be expected to be present at the RNA-binding interface for dsRBD/AGAA22 complex if the dsRBD searches between the specific tetraloop site and nonspecific stem region, since contacts to the RNA stem in the nonspecific complex would not be identical to the specific complex.

Comparison to budding yeast Dicer Budding yeast Dicers have two dsRBDs: the first (dsRBD1) is located immediately adjacent to the endoND, as in Rnt1p, and the second (dsRBD2), is at the C-terminus of the protein and separated from dsRBD1 by a long intervening sequence with no known structural motifs. The *S. castellii* Dcr1 dsRBD1, but not dsRBD2, was shown to be necessary for efficient processing of long dsRNA substrates to 23-nt fragments and for specificity of the enzyme for dsRNA over ssRNA.[65] Dcr1, however, does not have tetraloop specificity. A superimposition of the crystal structure of the free *K. polysporus* Dcr1 dsRBD1 and the solution structure of the free Rnt1p dsRBD (Fig. 3.18) indicates that the two dsRBDs have the same overall conformation, including a short helix

$\alpha3$ in Dcr1, but differ in regions that are important for specific RNA binding by Rnt1p dsRBD. Notably, in Dcr1 there are no interactions between the $\alpha1$-$\beta1$ loop and helix $\alpha3$ because helix $\alpha3$ is shorter in the Dcr1 dsRBD1, and the $\alpha1$-$\beta1$ loop adopts a different conformation compared to the Rnt1p dsRBD. Although Dcr1 dsRBD1 has some conserved hydrophobic residues in the $\alpha1$-$\beta1$ loop, e.g. L278 and I280 in *K. polysporus* Dcr1 correspond to Rnt1p dsRBD hinge residues I378 and Y380, it does not appear to have an extended hydrophobic core. L278 cannot undergo the rotameric change that we see for I378, and the I280 side-chain is oriented toward the outside of the protein. These residues do not interact with helix $\alpha3$ and do not appear to constitute an analogous hinge. Interestingly, *K. polysporus* Dcr1 L275 has hydrophobic interactions with the conserved residue Y341, which is in the loop extending past helix $\alpha3$ in the dsRBD1. We speculate that the absence in Dcr1 dsRBD1 of an extended hydrophobic core involving the $\alpha1$-$\beta1$ loop results in the loss of tetraloop specificity for *K. polysporus* and *S. castellii* Dcr1. Nevertheless, structural features within this region that are unique to the Dcr1 dsRBD may affect its binding affinity to Dcr1 substrates. Interestingly, *C. albicans* Dcr1 is able to carry out both Rnt1 and Dcr1 functions,[28] suggesting that its dsRBD1 may retain the structural features necessary for tetraloop recognition, including the extended hydrophobic core.

3.6 Supplemental Information

Table 3.1. Structural statistics of Rnt1p dsRBD

Distance and dihedral restraints	
Total NOE restraints	2068
Intraresidue	581
Sequential	472
Medium ($i+2$ to $i+4$)	489
Long range ($>i+4$)	526
Hydrogen bond restraints	62
RDC restraints	55
Dihedral angle restraints	138
Structure statistics (20 lowest-energy structures)	
No. of NOE violations $>$0.2 Å	0
No. of dihedral violations $>$5°	0
No. of RDC violations $>$2 Hz	0
RMSD of RDC (Hz)	0.20±0.02
RMSD from ideal covalent geometry	
Bond lengths (Å)	0.001±0.0001
Bond angles (°)	0.313±0.005
Impropers (°)	0.255±0.008
RMSD from the mean structure (Å)	
Backbone (residues 366–448)	0.56±0.11
Heavy atoms (residues 366–448)	1.05±0.09
Ramachandran statistics	
Most favored regions (%)	77.3
Additional allowed regions (%)	19.9
Generously allowed regions (%)	2.4
Disallowed regions (%)	0.4

Table 3.2. Model-free parameters.

	free dsRBD				dsRBD/AGAA14, 150 mM				dsRBD/AGAA14, 300 mM				dsRBD/AGAA22, 300 mM			
	Residue	S^2	τ_e	Model	Residue	S^2	τ_e	Model	Residue	S^2	τ_e	Model	Residue	S^2	τ_e	Model
	367	0.74	212.37	2	367	0.52	933.83	5	367	0.66	953.07	2				
	368	0.8	301.44	2	369	0.8	867.25	4	369	0.79	1146.08	4				
	370	0.88	0	3	370	0.95	0	1	370	0.96	413.61	4	370	0.96	1000	2
	371	0.98	0	1	371	0.91	0	3	371	0.94	0	3	371	1	0	1
	372	0.86	0	1				3								
	373	0.8	0	3	373	0.88	0	3	373	0.94	0	3	373	1	0	3
	374	0.82	0	3	374	0.88	0	3	374	0.93	0	3	374	1	0	1
	375	0.89	0	3	376	0.85	0	4	376	0.89	0	3	376	0.96	1000	4
	376	0.89	0	3	377	0.9	45.74	4	377	0.99	0	1	377	0.92	0	3
	377	0.94	0	1	378	0.93	104.28	1					378	1	0	1
	378	0.82	0	3	379	0.99	0	1					379	0.93	1000	4
	379	1	0	1	380	0.9	0	1	380	0.95	319.16	4	380	0.98	1000	2
	380	0.97	0	3	382	0.97	290.98	4	382	0.97	289.05	2	382	0.99	379.59	2
	383	1	0	1	383	0.95	924.19	4	383	0.94	1250.97	4	383	0.97	1000	2
	384	0.92	0	3	384	0.87	40.15	1	384	1	0	0	384	0.95	956.69	2
	385	0.79	3000	5	385	0.98	0	1	385	0.99	0	1	385	0.93	1000	4
	386	0.98	0	3	386	0.99	0	1	386	0.97	0	1	386	0.96	1000	2
	388	0.83	3000	5	388	0.92	0	1	388	0.9	47.88	2	388	1	0	1
	389	0.91	0	3	389	0.92	0	2	389	0.9	31.16	4	389	0.97	1000	2
	390	0.75	3000	5	390	0.91	57.92	5					390	0.9	999.37	5
	391	0.84	0	3	391	0.81	1395.09	2								
	392	0.93	0	1	392	0.93	142.14	2					392	0.92	1000	2
	394	0.82	876.3	5	394	0.92	767.54	2	394	0.93	714.07	4	394	0.88	904.99	5
	395	0.87	62.06	4	395	0.94	187.67	2	395	0.89	102.46	4	395	0.87	1000	5
	396	0.79	66.77	4	396	0.84	78.69	5	396	0.9	556.86	2	396	0.87	721.56	4
	399	0.54	791.1	5	399	0.65	804.38	2	399	0.68	952.3	5	399	0.72	927.49	4

ID				ID				ID				ID			
400	0.73	1715.9	5	400	0.91	47.1	2	400	0.95	62.76	4	400	0.93	1000	5
401	0.77	2011.68	5												
402	0.76	3000	5	402	0.94	121.91	1	402	1	0	1	402	0.97	1000	2
403	0.8	3000	5	403	0.98	0	1	403	0.97	0	2	403	0.95	1000	5
404	0.89	0	1	404	0.92	0	1	404	0.93	0	3	404	0.95	1000	2
405	0.89	3000	5	405	0.97	696.38	4	405	0.9	42.16	2	405	1	0	1
406	0.93	0	3	406	0.92	55.59	4	406	0.97	123.2	2	406	0.96	1000	2
408	0.95	522.02	4												
410	0.85	0	3	410	0.87	25.63	4	410	0.99	0	3				
411	0.79	2832.32	5	411	0.87	23.46	2	411	0.91	37.3	4	411	0.98	432.84	5
412	0.81	3000	5	412	0.95	164.61	1	412	1	0	1	412	0.89	975.83	2
413	0.83	3000	5	413	0.92	0	3	413	0.95	0	1	413	1	0	1
				414	0.93	0	1	414	0.94	0	3				
415	0.79	3000	5	415	1	0	1	415	1	0	1	415	1	0	1
416	0.84	1332.7	5	416	0.96	0	5	416	0.98	164.13	2	416	1	0	1
417	0.77	3000	5	417	0.86	1337.63	4	417	0.97	965.58	2	417	1	0	1
				418	0.96	763.76	1	418	0.97	590.6	2	418	0.98	1000	1
419	0.96	0	1	419	1	0	2	419	0.98	477.88	4	419	0.98	391.75	2
421	0.91	0	1	421	0.97	121.07	4	421	0.95	87.76	4	421	0.94	1000	4
422	0.92	0	1	422	0.9	35.3	1					422	1	0	3
423	0.92	1401.94	2	423	1	0	1	423	0.95	717.92	2	423	1	0	1
424	0.82	3000	5	424	0.97	0	1	424	0.96	0	0	424	1	0	1
425	0.92	0	1	425	0.96	0	1	425	0.94	0	3	425	1	0	1
				426	1	0	2					426	0.77	0	1
427	0.9	0	1	427	0.94	1006.45	1	427	0.74	1966.7	5	427	0.84	1000	5
428	0.92	0	1	428	0.96	0	1	428	0.99	0	1	428	0.95	1000	4
429	0.9	0	1	429	0.92	0	4	429	0.91	0	3	429	1	0	1
430	0.87	3000	5	430	0.96	627.89	1	430	0.98	0	3	430	0.97	464.69	2
431	0.91	0	1	431	0.99	0	1	431	1	0	3	431	1	0	3
432	0.89	0	1	432	0.95	0	2	432	0.87	30.87	4	432	1	0	1
433	0.82	1459.51	5	433	0.86	66.1	4	433	0.81	24.52	2	433	0.46	1000	5

ID			
434	0.71	3000	5
435	0.82	0	1
436	0.89	0	1
437	0.88	0	1
439	0.9	0	1
440	0.89	0	1
441	0.86	0	3
442	0.86	3000	5
443	0.91	0	1
445	0.91	0	3
448	0.67	1099.48	5
450	0.74	185.37	2

ID			
434	0.87	30.33	4
435	0.85	29.95	4
436	0.84	40.02	4
437	0.83	26.86	4
438	0.9	65.89	4
439	0.86	29.14	4
440	0.88	29.43	4
441	0.86	27.67	1
442	0.96	0	3
443	0.91	0	1
444	0.88	38.63	2
447	0.82	86.76	5
448	0.55	715.07	

ID			
434	0.92	0	3
435	0.9	54.13	2
436	0.92	53.32	4
437	0.87	23.12	2
439	0.93	52.84	4
440	0.95	0	3
442	1	0	1
443	0.97	100.7	4
445	0.94	536.04	4
448	0.89	707.63	4
450	0.56	853.51	5

ID			
434	0.94	1000	2
435	0.91	1000	4
437	0.79	1000	5
438	0.93	1000	4
439	0.94	1000	4
440	1	0	3
441	0.99	0	3
442	0.91	1000	4

Table 3.3 Diffusion tensor parameters.

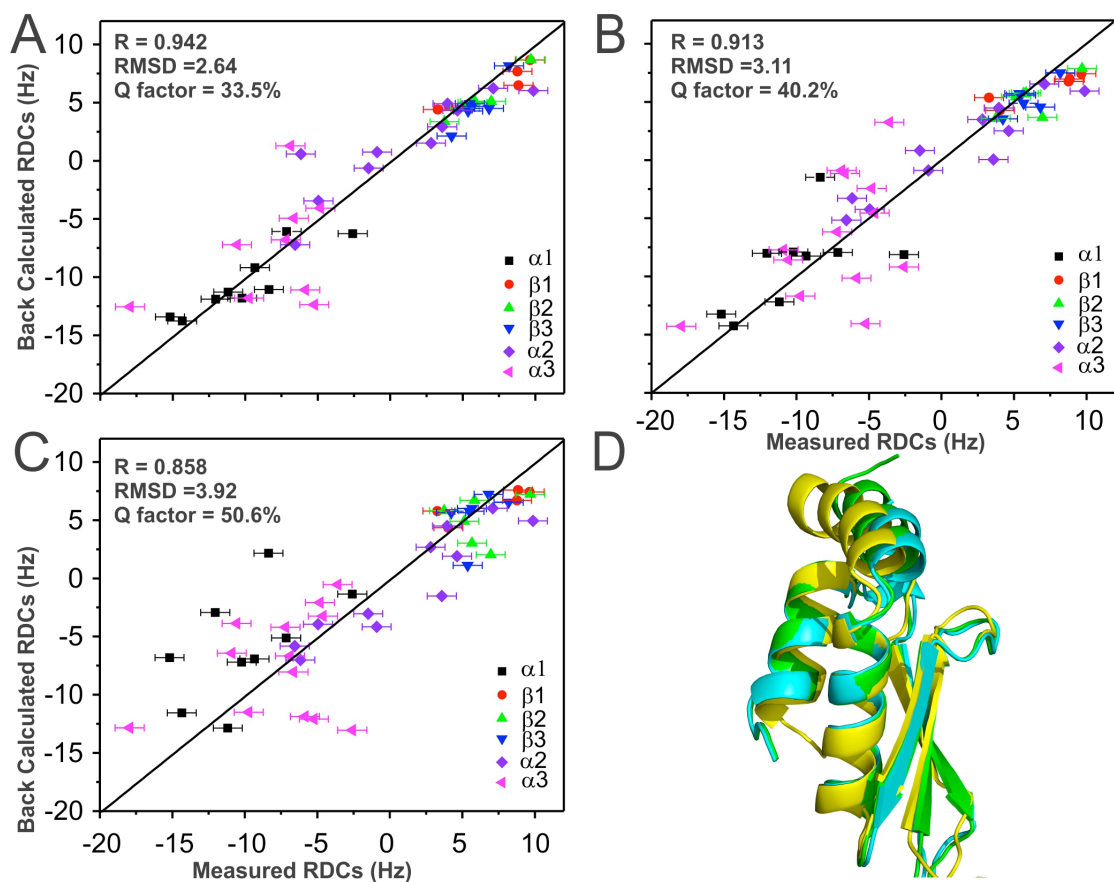| RNA	τ_m (ns)	$D_{\parallel/\perp}$
dsRBD (150 mM NaCl)		
HYDRONMR	8.0	1.84
ModelFree-optimized	7.83	1.60
dsRBD/AGAA (150 mM NaCl)		
HYDRONMR	15.6	1.83
ModelFree-optimized	15.53	1.42
dsRBD/AGAA (300 mM NaCl)		
HYDRONMR	15.6	1.83
ModelFree-optimized	13.27	1.47
dsRBD/AGAA22 (300 mM NaCl)		
HYDRONMR	23.1	2.36
ModelFree-optimized	18.64	1.26

Fig. 3.10. Correlation plots for experimental and back-calculated RDCs for the free dsRBD. (A) Crystal structure (1T4O, chain A) *versus* the free dsRBD. (B) Crystal structure (1T4O, chain B) *versus* the free dsRBD. (C) Solution structure (1T4N) *versus* the free dsRBD. (D) Superposition of the solution structure (orange), crystal structure, chain A (cyan), crystal structure, chain B (magenta), and the bound dsRBD (green). The red arrows indicate the movement of helix α1 and helix α3. The structures were aligned using helix α2, and sheets β1, β2, and β3.
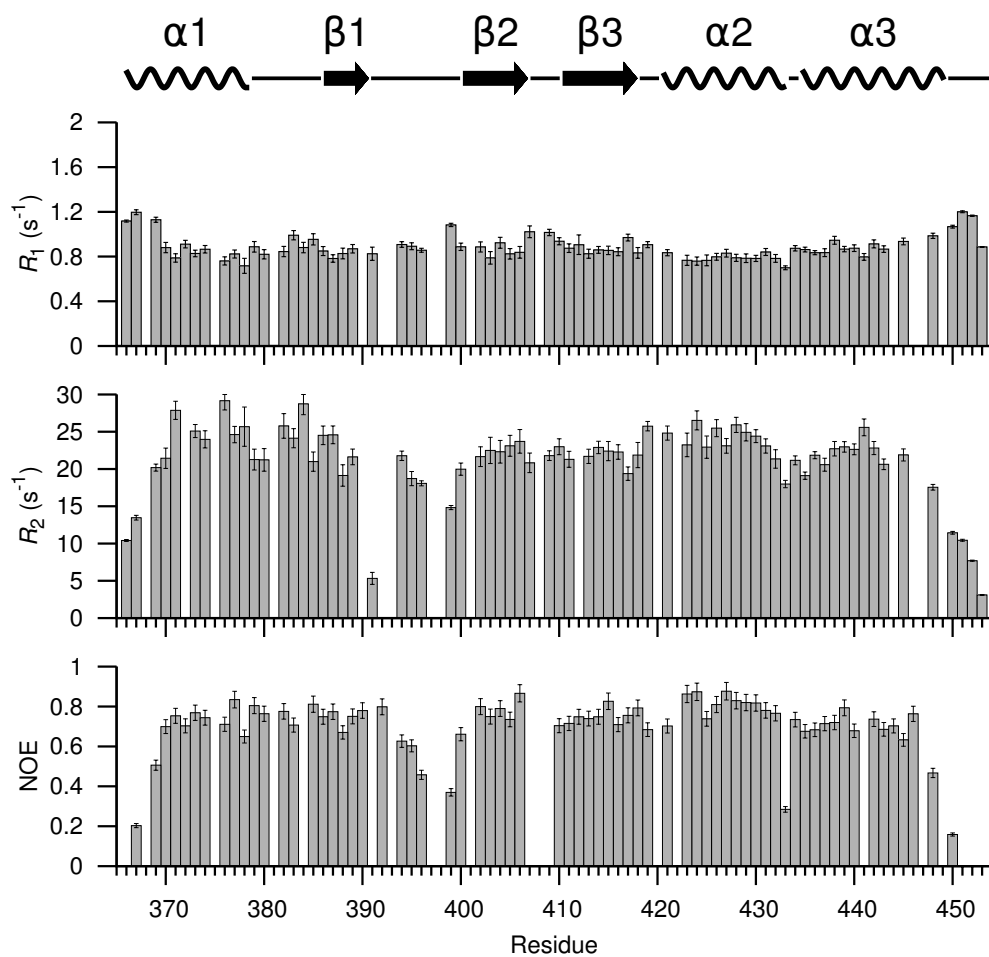
Fig. 3.11. ^{15}N relaxation parameters for dsRBD/AGAA at 150 mM NaCl at 20°C. Error bars reflect the fitting error for R_1 and R_2 values and the estimated error in the measurement for NOE values based on the noise in the spectrum.

Fig. 3.12. Comparison of R_2 values for the dsRBD/AGAA14 complex at 1 mM (red) and 0.5 mM (violet).

Fig. 3.13. ^{15}N relaxation parameters for dsRBD/AGAA at 300 mM NaCl at 20°C. Error bars reflect the fitting error for R_1 and R_2 values and the estimated error in the measurement for NOE values based on the noise in the spectrum.
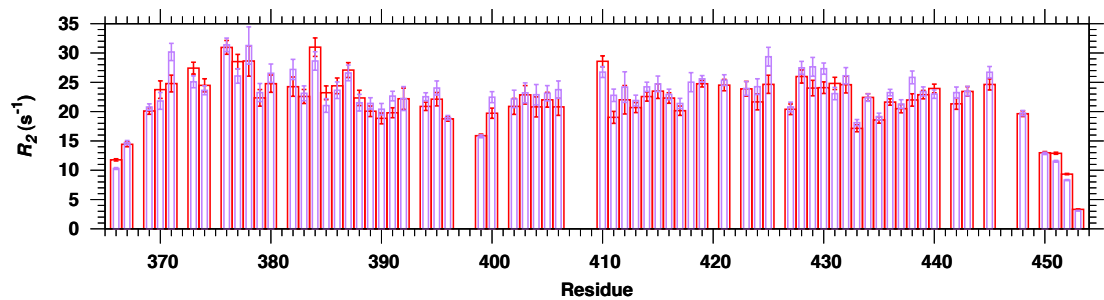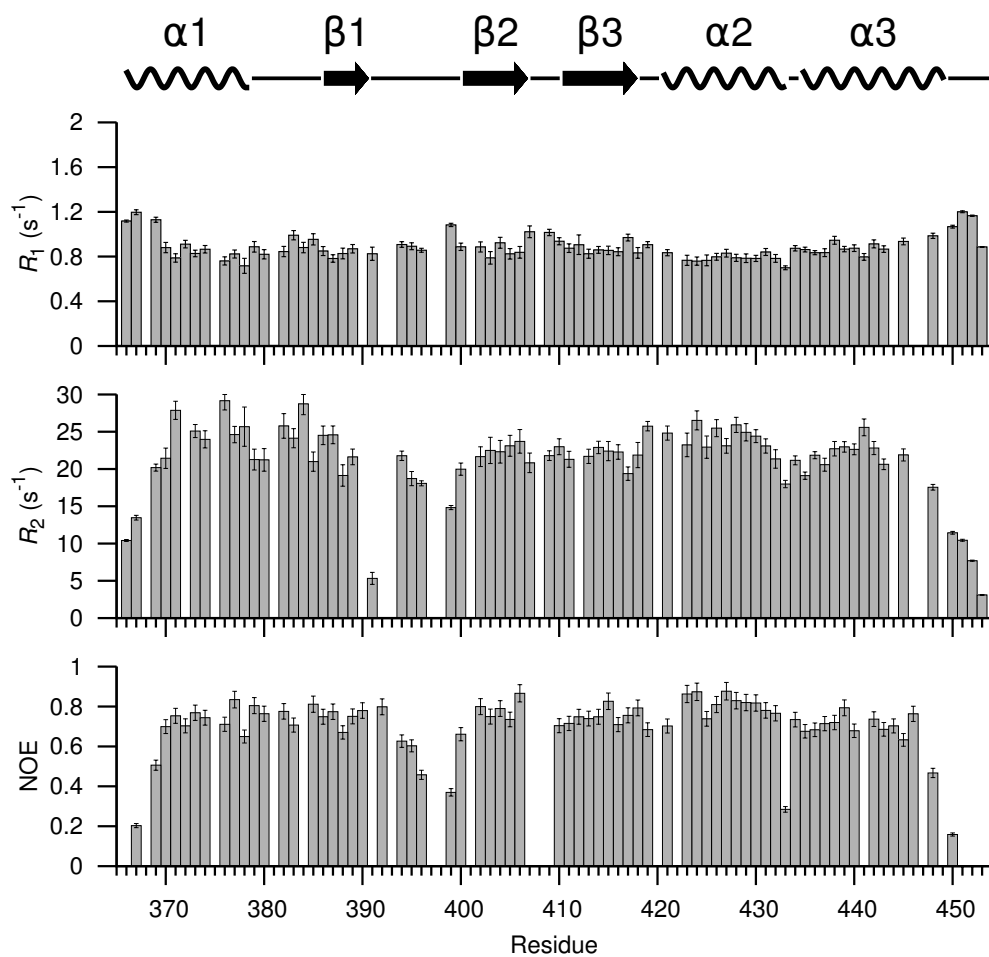
Fig. 3.14. ^{15}N relaxation parameters for dsRBD/AGAA22 at 300 mM NaCl at 20°C. Error bars reflect the fitting error for R_1 and R_2 values and the estimated error in the measurement for NOE values based on the noise in the spectrum.
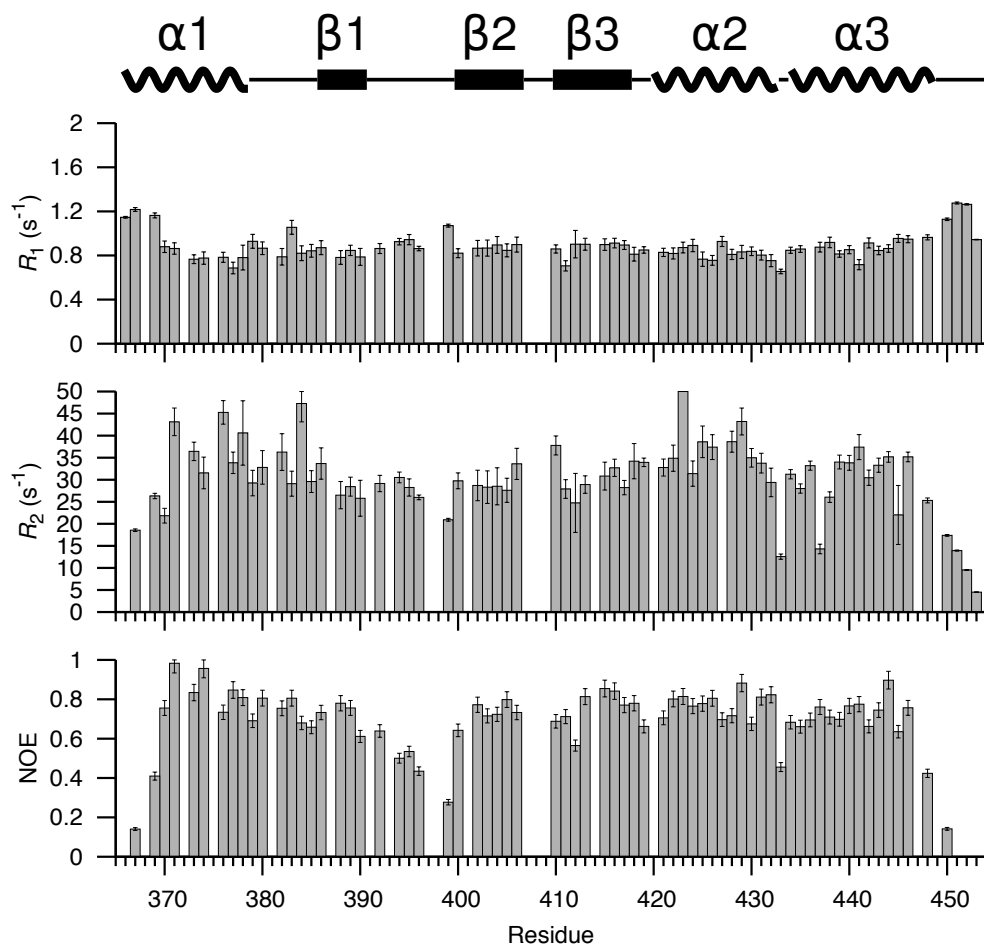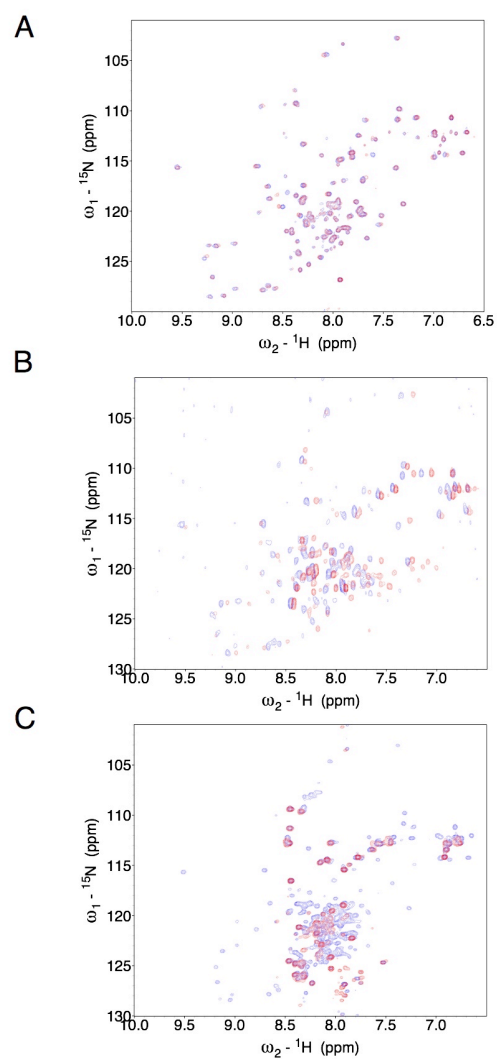
Fig. 3.15. ^{15}N-HSQC spectra of dsRBD mutants. Free dsRBD (blue) and dsRBD + AGAA (red) spectra for (A) dsRBD G379P, (B) dsRBD G379A, and (C) dsRBD I378A mutants.
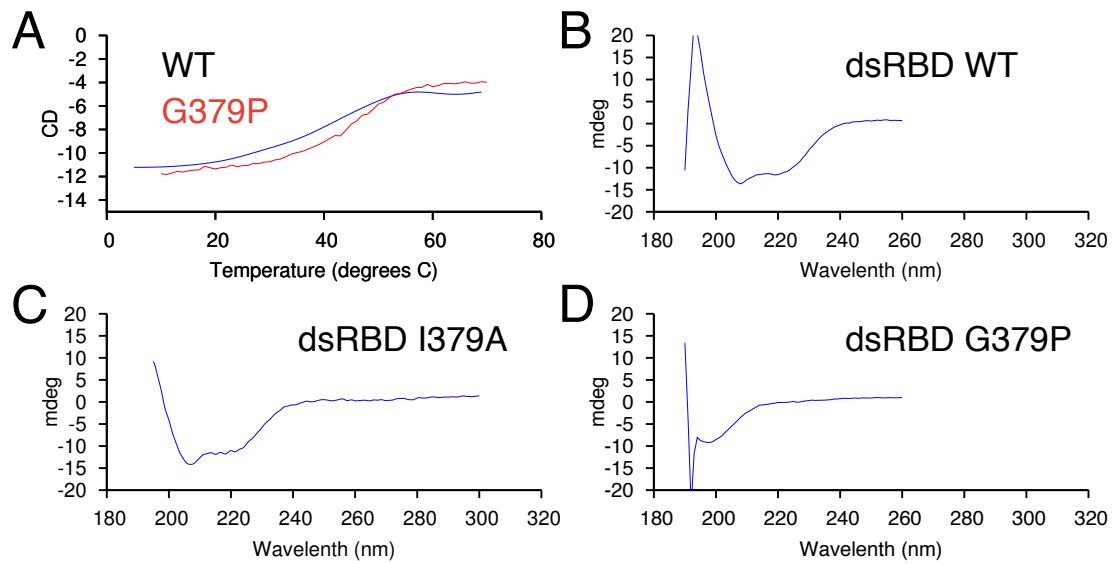
Fig. 3.16. (A) dsRBD WT and G379P have different melting temperatures, as measured by circular dichoism. (B-D) CD spectra of dsRBD WT, G378P, and I379A at 25°C, showing that dsRBD 379A is unstructured.
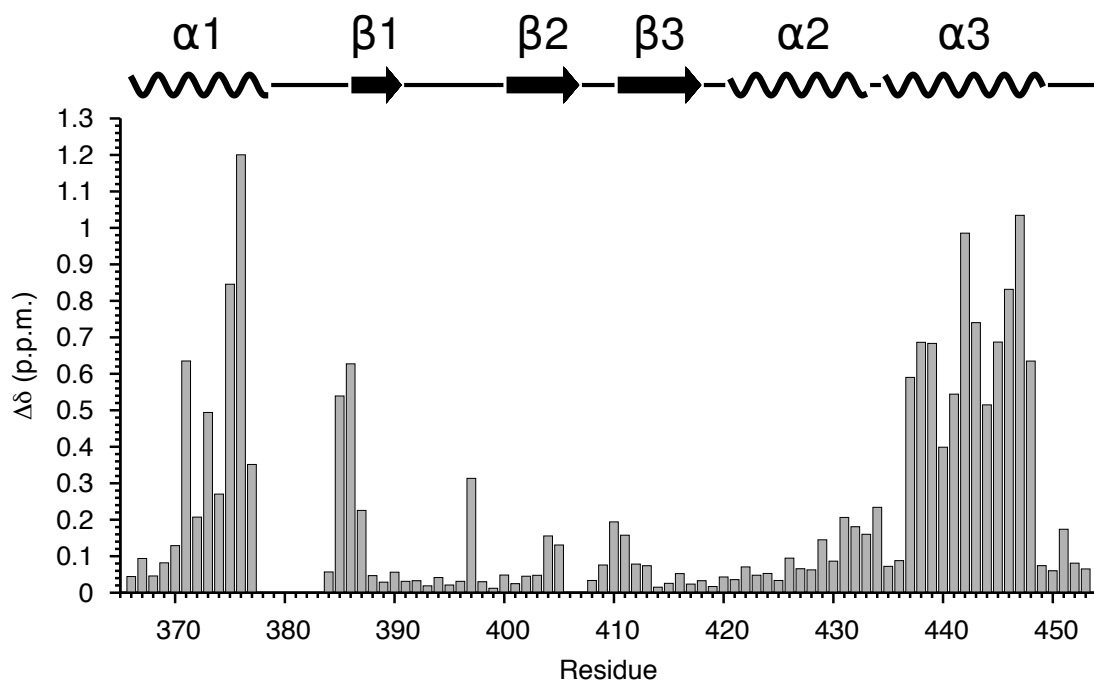
Fig. 3.17. Chemical shift difference between dsRBD WT and dsRBD G379P. Chemical shift difference between dsRBD WT and dsRBD G379P was calculated as the weighted average of H(N), N(H), CA, and CO chemical shifts, where

$$\Delta\delta = \sqrt{(\Delta\delta H_N)^2 + (\Delta\delta N_H/5)^2 + (\Delta\delta C\alpha/4)^2 + (\Delta\delta CO/4)^2}$$

No peaks were observed for residues in the $\alpha1$-$\beta1$ loop.

Fig. 3.18. (A) Hydrophobic core residues in the free Rnt1p dsRBD and (B) the corresponding residues in the Dcr1 dsRBD.

3.7   References

1. Ketting, R. F., Fischer, S. E., Bernstein, E., Sijen, T., Hannon, G. J. and Plasterk, R. H. (2001). Dicer functions in RNA interference and in synthesis of small RNA involved in developmental timing in *C. elegans. Genes Dev.* **15**, 2654-9.
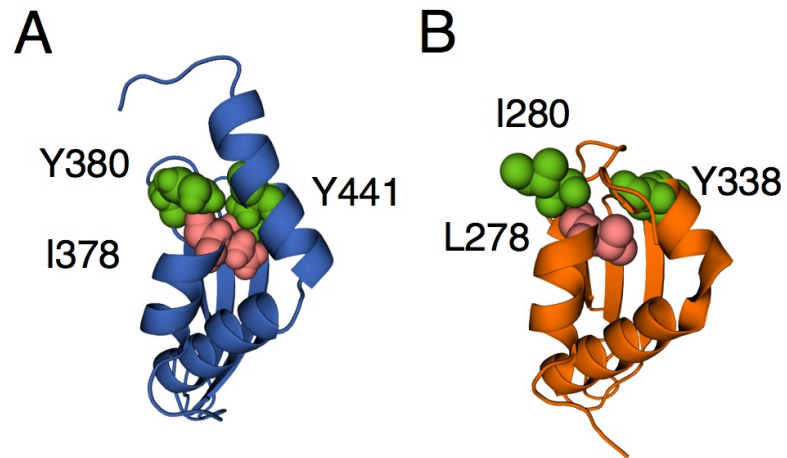
2. Knight, S. W. and Bass, B. L. (2001). A role for the RNase III enzyme DCR-1 in RNA interference and germ line development in *Caenorhabditis elegans. Science.* **293**, 2269-71.

3. He, L. and Hannon, G. J. (2004). MicroRNAs: small RNAs with a big role in gene regulation. *Nat. Rev. Genet.* **5**, 522-31.

4. Ji, X. (2006). Structural basis for non-catalytic and catalytic activities of ribonuclease III. *Acta. Crystallogr. D Biol. Crystallogr.* **62**, 933-40.

5. MacRae, I. J. and Doudna, J. A. (2007). Ribonuclease revisited: structural insights into ribonuclease III family enzymes. *Curr. Opin. Struct. Biol.* **17**, 138-45.

6. Kufel, J., Dichtl, B. and Tollervey, D. (1999). Yeast Rnt1p is required for cleavage of the pre-ribosomal RNA in the 3′ ETS but not the 5′ ETS. *RNA* **5**, 909-17.

7. Elela, S. A., Igel, H. and Ares, M., Jr. (1996). RNase III cleaves eukaryotic preribosomal RNA at a U3 snoRNP-dependent site. *Cell.* **85**, 115-24.

8. Ghazal, G., Ge, D., Gervais-Bird, J., Gagnon, J. and Abou Elela, S. (2005). Genome-wide prediction and analysis of yeast RNase III-dependent snoRNA processing signals. *Mol. Cell. Biol.* **25**, 2981-94.

9. Chanfreau, G., Legrain, P. and Jacquier, A. (1998). Yeast RNase III as a key processing enzyme in small nucleolar RNAs metabolism. *J. Mol. Biol.* **284**, 975-88.

10. Lee, Y., Ahn, C., Han, J., Choi, H., Kim, J., Yim, J., Lee, J., Provost, P., Radmark, O., Kim, S. and Kim, V. N. (2003). The nuclear RNase III Drosha initiates microRNA processing. *Nature.* **425**, 415-9.

11. Chanfreau, G., Elela, S. A., Ares, M., Jr. and Guthrie, C. (1997). Alternative 3′-end processing of U5 snRNA by RNase III. *Genes. Dev.* **11**, 2741-51.

12. Abou Elela, S. and Ares, M., Jr. (1998). Depletion of yeast RNase III blocks correct U2 3′ end formation and results in polyadenylated but functional U2 snRNA. *EMBO J.* **17**, 3738-46.

13. Seipelt, R. L. and Peterson, M. L. (1995). Alternative processing of IgA pre-mRNA responds like IgM to alterations in the efficiency of the competing splice and cleavage-polyadenylation reactions. *Mol. Immunol.* **32**, 277-85.

14. Allmang, C., Kufel, J., Chanfreau, G., Mitchell, P., Petfalski, E. and Tollervey, D. (1999). Functions of the exosome in rRNA, snoRNA and snRNA synthesis. *EMBO J.* **18**, 5399-410.

15. Lee, C. Y., Lee, A. and Chanfreau, G. (2003). The roles of endonucleolytic cleavage and exonucleolytic digestion in the 5'-end processing of *S. cerevisiae* box C/D snoRNAs. *RNA* **9**, 1362-70.

16. Petfalski, E., Dandekar, T., Henry, Y. and Tollervey, D. (1998). Processing of the precursors to small nucleolar RNAs and rRNAs requires common components. *Mol. Cell. Biol.* **18**, 1181-9.

17. Qu, L. H., Henras, A., Lu, Y. J., Zhou, H., Zhou, W. X., Zhu, Y. Q., Zhao, J., Henry, Y., Caizergues-Ferrer, M. and Bachellerie, J. P. (1999). Seven novel methylation guide small nucleolar RNAs are processed from a common polycistronic transcript by Rat1p and RNase III in yeast. *Mol. Cell. Biol.* **19**, 1144-58.

18. Danin-Kreiselman, M., Lee, C. Y. and Chanfreau, G. (2003). RNAse III-mediated degradation of unspliced pre-mRNAs and lariat introns. *Mol. Cell.* **11**, 1279-89.

19. Egecioglu, D. E., Kawashima, T. R. and Chanfreau, G. F. (2012). Quality control of MATa1 splicing and exon skipping by nuclear RNA degradation. *Nucleic. Acids. Res.* **40**, 1787-96.

20. Ghazal, G., Gagnon, J., Jacques, P. E., Landry, J. R., Robert, F. and Elela, S. A. (2009). Yeast RNase III triggers polyadenylation-independent transcription termination. *Mol. Cell.* **36**, 99-109.

21. Rondon, A. G., Mischo, H. E., Kawauchi, J. and Proudfoot, N. J. (2009). Fail-safe transcriptional termination for protein-coding genes in *S. cerevisiae. Mol. Cell.* **36**, 88-98.

22. Lavoie, M., Ge, D. and Abou Elela, S. (2012). Regulation of conditional gene expression by coupled transcription repression and RNA degradation. *Nucleic Acids Res.* **40**, 871-83.

23. Ge, D., Lamontagne, B. and Elela, S. A. (2005). RNase III-mediated silencing of a glucose-dependent repressor in yeast. *Curr. Biol.* **15**, 140-5.

24. Zer, C. and Chanfreau, G. (2005). Regulation and surveillance of normal and 3′-extended forms of the yeast aci-reductone dioxygenase mRNA by RNase III cleavage and exonucleolytic degradation. *J. Biol. Chem.* **280**, 28997-9003.

25. Chanfreau, G., Buckle, M. and Jacquier, A. (2000). Recognition of a conserved class of RNA tetraloops by *Saccharomyces cerevisiae* RNase III. *Proc. Natl. Acad. Sci. U.S.A.* **97**, 3142-7.

26. Nagel, R. and Ares, M., Jr. (2000). Substrate recognition by a eukaryotic RNase III: the double-stranded RNA-binding domain of Rnt1p selectively binds RNA containing a 5′-AGNN-3′ tetraloop. *RNA.* **6**, 1142-56.

27. Drinnenberg, I. A., Weinberg, D. E., Xie, K. T., Mower, J. P., Wolfe, K. H., Fink, G. R. and Bartel, D. P. (2009). RNAi in budding yeast. *Science.* **326**, 544-50.

28. Bernstein, D. A., Vyas, V. K., Weinberg, D. E., Drinnenberg, I. A., Bartel, D. P. and Fink, G. R. (2012). *Candida albicans* Dicer (CaDcr1) is required for efficient ribosomal and spliceosomal RNA maturation. *Proc. Natl. Acad. Sci. U.S.A.* **109**, 523-8.

29. Nanduri, S., Carpick, B. W., Yang, Y., Williams, B. R. and Qin, J. (1998). Structure of the double-stranded RNA-binding domain of the protein kinase PKR reveals the molecular basis of its dsRNA-mediated activation. *EMBO J.* **17**, 5458-65.

30. Ryter, J. M. and Schultz, S. C. (1998). Molecular basis of double-stranded RNA-protein interactions: structure of a dsRNA-binding domain complexed with dsRNA. *EMBO J.* **17**, 7505-13.

31. Stefl, R., Oberstrass, F. C., Hood, J. L., Jourdan, M., Zimmermann, M., Skrisovska, L., Maris, C., Peng, L., Hofr, C., Emeson, R. B. and Allain, F. H. (2010). The solution structure of the ADAR_2 dsRBM-RNA complex reveals a sequence-specific readout of the minor groove. *Cell.* **143**, 225-37.

32. Mueller, G. A., Miller, M. T., Derose, E. F., Ghosh, M., London, R. E.

and Hall, T. M. (2010). Solution structure of the Drosha double-stranded RNA-binding domain. *Silence.* **1**, 2.

33. Wu, H., Henras, A., Chanfreau, G. and Feigon, J. (2004). Structural basis for recognition of the AGNN tetraloop RNA fold by the double-stranded RNA-binding domain of Rnt1p RNase III. *Proc. Natl. Acad. Sci. U.S.A.* **101**, 8307-12.

34. Leulliot, N., Quevillon-Cheruel, S., Graille, M., van Tilbeurgh, H., Leeper, T. C., Godin, K. S., Edwards, T. E., Sigurdsson, S. T., Rozenkrants, N., Nagel, R. J., Ares, M. and Varani, G. (2004). A new alpha-helical extension promotes RNA binding by the dsRBD of Rnt1p RNAse III. *EMBO J.* **23**, 2468-77.

35. Wang, Z., Hartman, E., Roy, K., Chanfreau, G. and Feigon, J. (2011). Structure of a Yeast RNase III dsRBD Complex with a Noncanonical RNA Substrate Provides New Insights into Binding Specificity of dsRBDs. *Structure.* **19**, 999-1010.

36. Ghazal, G. and Elela, S. A. (2006). Characterization of the reactivity determinants of a novel hairpin substrate of yeast RNase III. *J. Mol. Biol.* **363**, 332-44.

37. Henzler-Wildman, K. and Kern, D. (2007). Dynamic personalities of proteins. *Nature.* **450**, 964-72.

38. Boehr, D. D., Nussinov, R. and Wright, P. E. (2009). The role of dynamic conformational ensembles in biomolecular recognition. *Nat. Chem. Biol.* **5**, 789-96.

39. Guillerez, J., Lopez, P. J., Proux, F., Launay, H. and Dreyfus, M. (2005). A mutation in T7 RNA polymerase that facilitates promoter clearance. *Proc. Natl. Acad. Sci. U.S.A.* **102**, 5958-63.

40. Wu, H., Finger, L. D. and Feigon, J. (2005). Structure determination of protein/RNA complexes by NMR. *Methods Enzymol.* **394**, 525-45.

41. Kay, L. E., Xu, G. Y. and Yamazaki, T. (1994). Enhanced-Sensitivity Triple-Resonance Spectroscopy with Minimal H_2O Saturation. *J. Magn. Reson.* **109**, 129-133.

42. Grzesiek, S. and Bax, A. (1993). The importance of not saturating water in protein NMR. Application to sensitivity enhancement and NOE measurements. *J. Amer. Chem. Soc.* **115**, 12593-12594.

43. Schleucher, J., Schwendinger, M., Sattler, M., Schmidt, P., Schedletzky, O., Glaser, S. J., Sorensen, O. W. and Griesinger, C. (1994). A general enhancement scheme in heteronuclear multidimensional NMR employing pulsed field gradients. *J. Biomol. NMR.* **4**, 301-6.

44. Ottiger, M., Delaglio, F. and Bax, A. (1998). Measurement of J and Dipolar Couplings from Simplified Two-Dimensional NMR Spectra. *J. Magn. Reson.* **131**, 373-378.

45. Ruckert, M. and Otting, G. (2000). Alignment of Biological Macromolecules in Novel Nonionic Liquid Crystalline Media for NMR Experiments. *J. Amer. Chem. Soc.* **122**, 7793-7797.

46. Cornilescu, G., Delaglio, F. and Bax, A. (1999). Protein backbone angle restraints from searching a database for chemical shift and sequence homology. *J. Biomol. NMR.* **13**, 289-302.

47. Schwieters, C. D., Kuszewski, J. J., Tjandra, N. and Clore, G. M. (2003). The Xplor-NIH NMR molecular structure determination package. *J. Magn. Reson.* **160**, 65-73.

48. Clore, G. M., Gronenborn, A. M. and Tjandra, N. (1998). Direct structure refinement against residual dipolar couplings in the presence of rhombicity of unknown magnitude. *J. Magn. Reson.* **131**, 159-62.

49. Koradi, R., Billeter, M. and Wuthrich, K. (1996). MOLMOL: a program for display and analysis of macromolecular structures. *J. Mol. Graphics.* **14**, 51-5, 29-32.

50. DeLano, W. L. (2002). The PyMOL Molecular Graphics System.

51. Garcia de la Torre, J., Huertas, M. L. and Carrasco, B. (2000). HY-DRONMR: prediction of NMR relaxation of globular proteins from atomic-level structures and hydrodynamic calculations. *J. Magn. Reson.* **147**, 138-46.

52. Bernado, P., Garcia de la Torre, J. and Pons, M. (2002). Interpretation of ^{15}N NMR relaxation data of globular proteins using hydrodynamic calculations with HYDRONMR. *J. Biomol. NMR.* **23**, 139-50.

53. Mandel, A. M., Akke, M. and Palmer, A. G., 3rd. (1995). Backbone dynamics of *Escherichia coli* ribonuclease HI: correlations with structure and function in an active enzyme. *J. Mol. Biol.* **246**, 144-63.

54. Lipari, G. and Szabo, A. (1982). Model-free approach to the interpretation of nuclear magnetic resonance relaxation in macromolecules. 2. Analysis of experimental results. *J. Am. Chem. Soc.* **104**, 455970.

55. Lipari, G. and Szabo, A. (1982). Model-free approach to the interpretation of nuclear magnetic resonance relaxation in macromolecules. 1. Theory and range of validity. *J. Am. Chem. Soc.* **104**, 454659.

56. Henras, A. K., Sam, M., Hiley, S. L., Wu, H., Hughes, T. R., Feigon, J. and Chanfreau, G. F. (2005). Biochemical and genomic analysis of substrate

recognition by the double-stranded RNA binding domain of yeast RNase III. *RNA* **11**, 1225-37.

57. Storici, F., Lewis, L. K. and Resnick, M. A. (2001). *in vivo* site-directed mutagenesis using oligonucleotides. *Nat. Biotechnol.* 19, 773-6.

58. Sambrook, J. and Russell, D. W. (2001). *Molecular Cloning: A laboratory manual.* 3rd edit., Cold Spring Harbor Laboratory Press, New York.

59. Massi, F., Grey, M. J. and Palmer, A. G., 3rd. (2005). Microsecond timescale backbone conformational dynamics in ubiquitin studied with NMR R_1rho relaxation experiments. *Protein Sci.* **14**, 735-42.

60. Ravindranathan, S., Oberstrass, F. C. and Allain, F. H. (2010). Increase in backbone mobility of the VTS1p-SAM domain on binding to SRE-RNA. *J. Mol. Biol.* **396**, 732-46.

61. Maynard, C. M. and Hall, K. B. (2010). Interactions between PTB RRMs induce slow motions and increase RNA binding affinity. *J. Mol. Biol.* **397**, 260-77.

62. Kharrat, A., Macias, M. J., Gibson, T. J., Nilges, M. and Pastore, A. (1995). Structure of the dsRNA binding domain of *E. coli* RNase III. *EMBO J.* **14**, 3572-84.

63. Nanduri, S., Rahman, F., Williams, B. R. and Qin, J. (2000). A dynamically tuned double-stranded RNA binding mechanism for the activation of antiviral kinase PKR. *EMBO J.* **19**, 5567-74.

64. Arumugam, S., Gao, G., Patton, B. L., Semenchenko, V., Brew, K. and Van Doren, S. R. (2003). Increased backbone mobility in beta-barrel enhances entropy gain driving binding of N-TIMP-1 to MMP-3. *J. Mol. Biol.* **327**, 719-34.

65. Weinberg, D. E., Nakanishi, K., Patel, D. J. and Bartel, D. P. (2011). The inside-out mechanism of Dicers from budding yeasts. *Cell.* **146**, 262-76.